



Li, Li (2017) A surgical bone biopsy needle using ultrasonic-sonic frequency vibration. PhD thesis.

<http://theses.gla.ac.uk/8367/>

Copyright and moral rights for this work are retained by the author

A copy can be downloaded for personal non-commercial research or study, without prior permission or charge

This work cannot be reproduced or quoted extensively from without first obtaining permission in writing from the author

The content must not be changed in any way or sold commercially in any format or medium without the formal permission of the author

When referring to this work, full bibliographic details including the author, title, awarding institution and date of the thesis must be given

Enlighten:Theses
<http://theses.gla.ac.uk/>
theses@gla.ac.uk



University of Glasgow

A SURGICAL BONE BIOPSY NEEDLE USING ULTRASONIC-SONIC FREQUENCY VIBRATION

LI LI

A thesis submitted to
School of Engineering
University of Glasgow

In the fulfilment of the requirements for the degree of

Doctor of Philosophy

July 2017

I. Abstract

This thesis presents a surgical needle designed for bone biopsy, based on an ultrasonic-sonic drilling mechanism. Bone biopsy is an invasive diagnostic procedure where a bone sample is extracted for clinical analysis. For conventional bone biopsy methods, closed biopsy is normally adopted and uses a core needle. An intact and viable biopsy sample is required for clinical analysis. However, a particular limitation of closed biopsy is that the microarchitecture of the biopsy sample can be easily damaged due to the large force which is applied through the core needle to penetrate bone. In some cases, the bone biopsy samples are fractured or crushed during the biopsy process. Power ultrasonic surgical devices have improved many aspects of bone cutting procedures, such as lower cutting force, higher accuracy, and better preservation of the tissue around the cutting site. In this study, an ultrasonic-sonic needle (US needle) system is designed and used to extract an intact biopsy sample and the penetration performance is evaluated by the effective impulse delivered to the target. The ultrasonic-sonic drilling mechanism was originally invented for rock drilling in low environments. In the US needle system, a free mass oscillates between an ultrasonic transducer-horn and a surgical needle, converting the ultrasonic frequency vibration of the horn to sonic frequency vibration of the needle. Compared to other ultrasonic surgical devices that directly transfer the ultrasonic vibrations from the cutting tip to the tissue, the US needle allows sufficient time between impacts with the free mass for the tip vibration amplitude to be re-established in the horn. This can maintain penetration progress of the needle into bone, where the rate of progress has been shown to be proportional to the effective impulse delivered by the needle to the bone. To maximise the effective impulse, a numerical model is developed to simulate the dynamic behaviour of the needle system and optimise the US needle.

To build the US needle system, the design and optimisation of the ultrasonic transducer-horn were investigated with the finite element method and experimental modal analysis, ensuring that the transducer-horn operates at the tuned frequency (50kHz) with a pure longitudinal mode. The configuration of the ultrasonic horn determines the momentum transferred to the free mass and hence also affects the effective impulse delivered to the target. The shape and dimensions of the ultrasonic horn were determined through the finite element model of the

ultrasonic horn impacting the free mass, which focused on maximising the post-collision velocity of the free-mass. The dynamic components of the US needle were also investigated.

A numerical model representing the dynamic behaviour of the needle system was developed, allowing the optimisation of each dynamic component, maximising the effective impulse delivered to the target. Each dynamic component of the US needle was modelled as a mass-spring-damper (MSD) system, which constituted the whole system dynamic model. The numerical model was validated by experiments using a prototype needle. The free-mass velocity, needle velocity and impact force predicted by the numerical model were compared with the results measured from experiments using 3D laser Doppler vibrometry, an ultra-high speed camera and a load cell, respectively. The numerical model results exhibit good agreement with the experimental results, indicating the numerical model can be used as a predictive tool to evaluate the performance of the US needle when different configurations are implemented. The configuration of the US needle is studied to maximise the effective impulse by the numerical model, through optimisation of the mass of the free mass, spring rate and spring pre-load. An optimised configuration of the US needle was determined by the numerical model and validated by experiments. The resulting prototype of the needle device was tested in ovine femur *in vitro* and was demonstrated to retrieve a cortical bone biopsy sample with a more cylindrical geometry, smoother surface and more intact sample than a cortical biopsy sample retrieved using a conventional trephine needle. Moreover, the penetration performance of the US needle was also compared with an ultrasonic resonant needle where the ultrasonic transducer and surgical needle resonate at the same frequency.

II. Acknowledgements

First and foremost, I must recognise and express my sincerest gratitude to my supervisor Professor Margaret Lucas for her support, effort, patience and guidance. She always proposed many valuable suggestions for my research. Also I would like to thank her for giving me opportunities to present my research in various countries and discuss my research with researchers around the world.

I would like to thank the China Scholarship Council and the British Research Council (the Engineering and Physical Sciences Research Council, grant number EP/K020013/1) for funding this research.

I would also like to thank the members of the Medical and Industrial Ultrasonics Group, for giving me their suggestions and time on discussing my work, providing space to conduct experiments, revising my thesis and improving my English. A special thanks goes to Professor Hamish Simpson and Dr Robert Wallace from the Department of Orthopaedics and Trauma of the University of Edinburgh for their help in evaluation of the performance of the surgical procedures in cutting ovine bones.

Thanks are expressed to the technical staff in the workshop for their assistance and suggestions on my mechanical design, and machining the components of the ultrasonic bone biopsy device.

Thanks to my friends in Glasgow who made my life exciting, wonderful and happy. I will never forget the good times we had together.

Last, but definitely not the least, I wish to express my love and gratitude to my parents who always encourage and support me, and believe in me no matter what I decided to do.

Thanks to all!

III. Contents

I. Abstract	i
II. Acknowledgements	iii
III. Contents	iv
IV. List of table captions.....	viii
V. List of figure captions	x
VI. List of symbols.....	xv
VII. Abbreviations.....	xviii
Chapter 1 Introduction	1
1.1 Introduction of ultrasound	2
1.2 High power ultrasonic system used in industrial and surgical applications.....	3
1.3 Ultrasonics in surgical applications.....	4
1.4 Bone drilling technologies	6
1.5 Ultrasonic-sonic drilling technology for bone biopsy	8
1.6 Outline of research	10
Chapter 2 Literature review	13
2.1 Early history of ultrasound	13
2.2 Review of ultrasonic applications in surgery	16
2.2.1 Ultrasound in neurosurgery	16
2.2.2 Ultrasound in vestibular surgery	17
2.2.3 Ultrasound in bone surgery	18
2.3 Research on biopsy.....	25

2.4 Research on ultrasonic-sonic drilling method	27
2.4.1 The invention of ultrasonic-sonic drilling method	27
2.4.2 Modelling of ultrasonic-sonic drilling system	30
 Chapter 3 Methodology of ultrasonic transducer and horn design	31
 3.1 Design of Langevin ultrasonic transducer.....	32
3.1.1 Determination of the resonant frequency, vibration mode and wavelength.....	32
3.1.2 Determination of piezo-ceramic rings.....	34
3.1.3 Material selection for back mass and front mass	35
3.1.4 Electrode and bolt.....	37
3.1.5 The mounting position of the high power transducer.....	38
3.1.6 Initial consideration of the dimensions of the transducer parts.....	38
3.2 Finite element analysis	39
3.2.1 Modelling of the ultrasonic transducer in FEA software Abaqus	40
3.2.2 Definition of piezo-ceramic material properties in Abaqus	42
3.2.3 Mesh convergence.....	47
3.3 Dimensions of each ultrasonic transducer part	49
3.3.1 The dimensions of the electrode.....	49
3.3.2 The dimensions of the back mass and front mass	50
3.4 Design of ultrasonic horn	52
3.4.1 Design of different shapes of ultrasonic horn by analytical method.....	53
3.4.2 Design of different shapes of ultrasonic horn by FEA method.....	60
3.5 Chapter conclusion.....	61

Chapter 4 Optimisation of the ultrasonic horn and design of the ultrasonic-sonic needle system.....	63
4.1 Optimisation of the ultrasonic horn.....	64
4.1.1 Determination of the shape of the ultrasonic horn	64
4.1.2 Determination of the tip diameter of the stepped horn.....	68
4.1.3 FE model of the ultrasonic transducer-horn	69
4.2 Experimental analysis of the ultrasonic transducer-horn	72
4.2.1 Assembly of the ultrasonic transducer-horn and electrical impedance analysis	72
4.2.2 Experimental modal analysis	75
4.2.3 Comparison of FEA and EMA.....	80
4.3 Experimental setup of the ultrasonic-sonic needle system.....	82
4.3.1 The ultrasonic-sonic needle system.....	82
4.3.2 The components of the ultrasonic-sonic needle system	84
4.4 Chapter Conclusion	91
Chapter 5 Modelling and optimisation of the ultrasonic-sonic needle system	93
5.1 The MSD model of the ultrasonic transducer-horn.....	94
5.1.1 Numerical model	94
5.1.2 Evaluation of the ultrasonic transducer-horn MSD model.....	103
5.1.3 The effective mass of the ultrasonic horn	104
5.2 The MSD model of the ultrasonic-sonic needle system.....	105
5.2.1 Free mass-surgical needle MSD model.....	105
5.2.2 The contact stiffness and damping coefficient of the target.....	109
5.2.3 Dynamic equations of the ultrasonic-sonic needle system.....	111
5.3 Validation of the MSD model of the ultrasonic-sonic needle system.....	112

5.3.1 Validation of the MSD model without the target	112
5.3.2 Validation of the MSD model with the target	114
5.4 Optimisation of the ultrasonic-sonic needle system.....	120
5.5 Chapter conclusion	127
 Chapter 6 Penetration tests.....	129
6.1 Biopsy needles and testing materials	130
6.2 Penetration tests on biomechanical test sample	132
6.3 Penetration tests on ovine femur	136
6.3.1 Penetration tests on ovine trabecular bone	136
6.3.2 Penetration tests on ovine cortical bone	140
6.4 Thermal damage analysis of the ultrasonic-sonic needle biopsy	146
6.5 Chapter conclusion	147
 Chapter 7 Conclusions and future work.....	149
7.1 Conclusions	149
7.2 Future work	151
Appendix I: References.....	153
Appendix II: Publications	169

IV. List of table captions

Table 3.1 Acoustic properties of the materials for the transducer design	35
Table 3.2 Values of $\sqrt{Z_b Z_f}$ for the different configurations of the ultrasonic transducer ...	36
Table 3.3 Material properties of the recommended materials for the transducer design	36
Table 3.4 Material properties of the transducer parts used for FE model.....	41
Table 3.5 Conversion of matrix form to tensor form	42
Table 3.6 PZT-8 material properties data expressed as the format of Abaqus (elastic properties, piezoelectric properties and electrical permittivity).....	46
Table 3.7 The number of elements required to achieve mesh convergence for the vibration modes of the ultrasonic transducer.....	47
Table 3.8 The frequencies of the 1 st longitudinal mode and neighbouring modes	51
Table 3.9 Formulae for calculating the resonant length and vibration amplitude gain of different horns [143, 145]	56
Table 3.10 Data used to plot the exponential curve	59
Table 3.11 The resonant length and vibration amplitude gain of the four different horns ..	59
Table 3.12 The resonant length and vibration amplitude gain of four different horn shapes tuned nearly at 50kHz by the analytical and FEA method (5mm horn tip diameter)	61
Table 4.1 The resonant length and vibration amplitude gain of four different horn shapes tuned nearly at 50kHz by the analytical and FEA method (8mm horn tip diameter)	67
Table 4.2 The resonant length and vibration amplitude gain of four different horn shapes tuned nearly at 50kHz by the analytical and FEA method (10mm horn tip diameter)	67
Table 4.3 The number of elements required to achieve mesh convergence for the vibration modes of the transducer-horn	71
Table 4.4 The frequencies of the 2 nd longitudinal mode and surrounding vibration modes	71
Table 4.5 Parameters of the ultrasonic transducer after each step of applying the pre-load	74
Table 5.1 The resonant frequencies of the undamped 2-DOF model	97
Table 5.2 Simulation and experiment of free mass average velocity and the average peak value of the needle velocity (without target).....	114
Table 5.3 Simulation and experiment of free mass average velocity and the average peak value of the needle velocity (with target).....	116

Table 5.4 The difference of the impact force distribution between experiment and simulation.....	118
Table 5.5 Two different configurations of the US needles	125
Table 6.1 Material properties of the three types of biomechanical materials	132
Table 6.2 Dimensions of the trephine needle and the US needle used for penetration tests on biomechanical samples.....	132
Table 6.3 Dimensions of the penetration holes shown in Fig. 6.5	135
Table 6.4 Dimensions of the trephine needles and the biopsy needles used for US needles	140

V. List of figure captions

Figure 1.1 Bone biopsy (a) open biopsy [6] (b) closed biopsy: bone marrow biopsy by a core needle [7].....	1
Figure 1.2 Different types of sound waves and their corresponding applications [22, 23] ...	2
Figure 1.3 High power ultrasonic system	4
Figure 1.4 Three vibration modes (a) longitudinal mode (b) torsional mode (c) flexural mode	4
Figure 1.5 Schematic of the microwave drilling system [50]	7
Figure 1.6 Schematic of an ultrasonic-sonic drill	8
Figure 1.7 The definition of effective impulse [58]	9
Figure 2.1 Ultrasonic surgical instrument developed for neurosurgery [74]	16
Figure 2.2 Bone structure: cortical bone and trabecular bone [81].....	19
Figure 2.3 Three mutually perpendicular directions of a femur cortical bone [81]	20
Figure 2.4 Manual bone cutting instruments (a) bone cutting forceps (b) bone biopsy needle (c) amputation saw (d) bone chisel.....	23
Figure 2.5 Electrical bone cutting devices (a) electrical bone drill (b) electrical bone saw	24
Figure 2.6 Ultrasonic bone cutting instrument: Misonix BoneScalpel (Misonix Corp.)	25
Figure 2.7 USDC device mounted on the Sojourner Rover for rock drilling [109].....	28
Figure 2.8 A rotary-hammering drilling and coring device used to conduct penetration tests on limestone [110].....	28
Figure 2.9 Ultrasonic planetary core drill mounted on EADS Astrium's Bridget testbed [59]	29
Figure 3.1 Schematic of the structure and components of a Langevin ultrasonic transducer	32
Figure 3.2 The relationship between the vibration amplitude and stress distribution of the ultrasonic transducer [128].....	33
Figure 3.3 The initial dimensions of the ultrasonic transducer.....	39
Figure 3.4 Number of elements required to obtain mesh convergence for the operating mode of the ultrasonic transducer and surrounding vibration modes (a) the 1 st torsional mode (b) the 1 st longitudinal mode (c) the 2 nd bending mode	48

Figure 3.5 The failure of the electrodes (electrodes made of copper alloy CZ106, 0.05mm thickness)	49
Figure 3.6 Modelled 1st longitudinal mode of the transducer at 50.04kHz (green colour). Note: the black frame structure represents the ultrasonic transducer without deformation.	51
Figure 3.7 The position of the nodal plane and flange.....	52
Figure 3.8 The shape of stepped-exponential horn	54
Figure 3.9 Calculation of the length of L_2 , L_3 and vibration amplitude gain (a) L_2 length (b) L_3 length (c) the vibration amplitude gain of stepped-exponential horn [146]	55
Figure 3.10 The coordinate of the exponential part	59
Figure 3.11 Mode shapes of the stepped, conical, exponential and stepped-exponential horn (1 st longitudinal vibration mode).....	60
Figure 4.1 FE model used to calculate the post-velocity of the free mass (a) the ultrasonic transducer-horn impacting the free mass (b) the ultrasonic horn impacting the free mass..	64
Figure 4.2 FE model of ultrasonic horn impacting the free mass: stage of after impact	65
Figure 4.3 The velocity of the free mass after a single collision by the four different shaped horns	68
Figure 4.4 The velocity of the free mass after single collision and the maximum stress in the horns, predicted by FEA.....	69
Figure 4.5 Mesh convergence study of the ultrasonic transducer-horn (a) 1 st longitudinal mode (b) 4 th bending mode (c) 2 nd longitudinal mode (d) 3 rd longitudinal mode	70
Figure 4.6 The parts of the ultrasonic transducer.....	72
Figure 4.7 Assembly of the ultrasonic transducer.....	73
Figure 4.8 The assembled ultrasonic transducer-horn	75
Figure 4.9 Electrical impedance analysis of the ultrasonic transducer and horn	75
Figure 4.10 Single degree of freedom system [151]	76
Figure 4.11 EMA of the transducer-horn (a) actual experimental setup (b) schematic diagram of the EMA showing the main components [142]	77
Figure 4.12 Grid points on the ultrasonic transducer-horn	79
Figure 4.13 The normalised modal peaks functions of EMA of the ultrasonic transducer-horn	80
Figure 4.14 The resonant frequencies and corresponding mode shapes of the transducer-horn measured by EMA and predicted by FEA	81

Figure 4.15 US needle system (a) schematic of the US needle system (b) the position of the rod (c) impact force measurement experimental setup	83
Figure 4.16 Different shapes of free mass (a) spherical free mass (b) cylindrical free mass (c) sphere with four flat faces (d) cylinder with cross profiles (e) cylinder with triangular profiles.....	84
Figure 4.17 Two different US needles (a) schematic of US needle 1 (b) schematic of US needle 2	85
Figure 4.18 Impact force measurement experimental setup of US needle 2	86
Figure 4.19 Testing the titanium free mass and stainless steel free mass for US needle.....	87
Figure 4.20 Needle tip geometries used for bone biopsy (a) bevel-shaped needle tip (b) fish-mouth-shaped needle tip (c) needle with multiple teeth (d) multi-bevel shaped needle	88
Figure 4.21 The assembled biopsy needle for the US needle	89
Figure 4.22 Schematic of the casing used for the US needle.....	90
Figure 5.1 The MSD model of the US needle.....	93
Figure 5.2 Modelling the ultrasonic transducer-horn as a 2-DOF system: (a) structure of the ultrasonic transducer-horn (b) simplification of the ultrasonic transducer-horn (c) the MSD model of the ultrasonic transducer-horn	95
Figure 5.3 The undamped 2-DOF model of the transducer-horn.....	96
Figure 5.4 Ultrasonic vibration of the ultrasonic transducer-horn model: the blue line shows the vibration displacement amplitude of the 2 nd mass and the pink dashed line represents the 1 st mass displacement.....	103
Figure 5.5 FE model of ultrasonic transducer-horn impacting the free mass: the transducer-horn operating at 49.99kHz, 2 nd longitudinal mode	104
Figure 5.6 MSD model of the impact between free mass and needle	106
Figure 5.7 The assembled biopsy needle	106
Figure 5.8 Schematic of contact time measurement experimental setup	107
Figure 5.9 One impact cycle between the free mass and needle.....	108
Figure 5.10 Images of the needle during one impact	110
Figure 5.11 Simulated impact force used to show the contact time between the surgical needle and target	110
Figure 5.12 The MSD model of the US needle system.....	111

Figure 5.13 Experimental setup used for validation of the MSD model	112
Figure 5.14 Comparison of the simulated velocity and measured velocity (without target): (a) and (b) represent free mass velocities from simulation model and experiment, respectively; (c) and (d) indicate needle velocities from simulation model and experiment, respectively	113
Figure 5.15 Comparison of the simulated velocity and measured velocity (with target): (a) and (b) represent free mass velocity from simulation model and experiment, respectively; (c) and (d) indicate needle velocity from simulation model and experiment, respectively	115
Figure 5.16 Comparison of the simulated impact force and measured impact force (a) the impact force predicted from simulation model (b) the impact force measured from experiment.....	117
Figure 5.17 Comparison of the impact force distribution between simulation and experiment.....	118
Figure 5.18 The values of effective impulse delivered to the target for different spring pre-loads: orange line is the experimental results and blue line represents the simulation results	120
Figure 5.19 Three different free masses used for optimisation of the US needle.....	121
Figure 5.20 The schematic of the US needle system used to indicate the position to add the spacers	122
Figure 5.21 The effective impulse values of the US needle with different configurations (simulation and experimental results)	123
Figure 5.22 Comparison of the penetration performance between US needle 3 and US needle 4	126
Figure 5.23 Penetration tests on ovine cortical bone using the US needle	126
Figure 6.1The dimensions of the US needle with the optimal configuration (without casing)	126
Figure 6.2 Two different bone biopsy needles (a) a conventional trephine needle, 101.00mm length (b) an US needle, 137.80mm length	130
Figure 6.3 UR needle designed for bone biopsy, 122mm length [93]	131

Figure 6.4 Two different bone biopsy needles used to conduct penetration tests on three different biomechanical materials (a) the conventional trephine needle biopsy (b) the US needle biopsy.....	133
Figure 6.5 The UR needle and the US needle used to perform penetration tests on the biomechanical materials (a) low density testing sample $0.13\text{g}/\text{cm}^3$, thickness 40mm (b) high density testing sample $0.64\text{g}/\text{cm}^3$, thickness 40mm, where Holes 1 and 2 were achieved by the UR needle, Hole 3 was achieved by the US needle (c) high density $0.64\text{g}/\text{cm}^3$ testing sample, thickness 40mm, where Hole 4 was achieved by the US needle	135
Figure 6.6 A penetration test on ovine femur (trabecular bone) using the US needle	137
Figure 6.7 3D μCT reconstruction of trabecular bone biopsy extracted by (a) the trephine needle (b) the UR needle (c) the US needle [93]	138
Figure 6.8 Comparison of the US needle biopsy and the trephine needle biopsy (a) Bone penetration tests using the trephine needle and US needle (b) bone biopsy sample retrieved by the trephine needle and the US needle	139
Figure 6.9 Bone biopsy tests (a) US needle biopsy (b) conventional trephine needle biopsy	141
Figure 6.10 Comparison of the trephine needle 1 before and after use	142
Figure 6.11 Comparison of bone biopsy performance between the trephine needle and the US needle	142
Figure 6.12 Biopsy samples from cortical bone (a) retrieved by the US needle, 2.83mm length (b) retrieved by the US needle, 1.36mm length (c) retrieved by the trephine needle	143
Figure 6.13 Bone chips around the biopsy site (a) US needle biopsy (b) trephine needle biopsy	144
Figure 6.14 US needle biopsy (a) US needle 6 used to conduct cortical bone biopsy (b) needle tip broken during the bone biopsy process	145
Figure 6.15 Temperature measurement during the bone biopsy procedure.....	147

VI. List of symbols

B	Coefficient of restitution
c	Speed of the stress wave propagating in the material
$c_1 \ c_2$	Damping coefficient of transducer-horn
c_3	Damping coefficient of free mass
c_4	Damping coefficient of surgical needle
c_5	Damping coefficient of target
D	Elastic stiffness constant of piezo-ceramic material
d	Piezoelectric constant
E	Young's modulus of elasticity
e_{ij}	Piezoelectric charge constant
F_0	Interaction force between the piezo-ceramic ring model and the 2-step mass
F_{PL}	Preload of spring
f	Frequency
G	Vibration amplitude gain
i, j, k, l, p, q	Directional notation
k_{eff}	Effective electromechanical coupling coefficient
k_{wn}	Wavenumber
$k_1 \ k_2$	Contact stiffness of ultrasonic transducer-horn
k_3	Contact stiffness of free mass
k_4	Contact stiffness of surgical needle
k_5	Contact stiffness of spring

L	Length
l_0	Thickness of piezo-ceramic ring
$m_1 \ m_2$	Effective mass of ultrasonic transducer-horn
m_{FM}	Effective mass of free mass
m_N	Effective mass of surgical needle
r	Radius
S	Cross-sectional area
s	Elastic compliance
t	Time
U	Energy of ultrasonic transducer-horn
U_{MSD}	Energy of transducer-horn MSD model
u	Voltage
x_0	Displacement of piezo-ceramic ring
$x_1 \ x_2$	Displacement of ultrasonic transducer-horn
x_3	Displacement of free mass
x_4	Displacement of surgical needle
Z_p	Acoustic impedance of piezo-ceramic material
Z_b	Acoustic impedance of back mass
Z_f	Acoustic impedance of front mass
ε_{ij}^T	Relative permittivity evaluated at constant stress
ε_{ij}^S	Relative permittivity evaluated at constant stress constant strain
ε_0	Absolute dielectric constant
λ	Wavelength

Ψ	Ratio of vibration amplitude
ω	Angular frequency of vibration

VII. Abbreviations

CT	Computerised tomography
CUSA	Cavitron ultrasonic surgical aspirator
DoF	Degree-of-freedom
EMA	Experimental modal analysis
FEA	Finite element analysis
FEM	Finite element method
FFT	Fast fourier transforms
FRF	Frequency response function
JPL	Jet Propulsion Laboratory
LF	Longitudinal-flexural vibration mode
LT	Longitudinal-torsional vibration mode
MRI	Magnetic imaging
MSD	Mass-spring-damper
PBS	Phosphate buffered saline
PZT	Lead zirconate titanate
SDoF	Single-degree-of-freedom
TF	Torsional-flexural vibration mode
UPCD	Ultrasonic planetary core drill
US	Ultrasonic-sonic
USDC	Ultrasonic-sonic drilling-coring

Chapter 1 Introduction

Bone biopsy is a diagnostic procedure where a bone sample is removed from the body and examined under a microscope for cancer, infection or other diseases [1, 2]. It is the most definitive way to diagnose bone cancer, which can distinguish whether a tumour is benign or cancerous. Bone biopsy is commonly performed by open biopsy or closed biopsy, and an intact and viable biopsy sample is acquired for clinical analysis. These two different biopsy methods are shown in Fig. 1.1. In an open biopsy, a surgical incision is made through the skin to expose and remove tissues, which is usually conducted under general anaesthesia. It can provide an adequate sample for diagnostic analysis. However, the cost of open biopsy is high and it increases the risk of spreading tumour cells and local contamination compared to closed biopsy [3, 4]. A closed biopsy is a minimally invasive procedure performed under local anaesthesia, usually using a fine needle or a core needle. The main limitations of a fine needle are that the false negative rate is high and the bone tissue architecture cannot be evaluated because of the small sample size [5]. The architecture of the bone tissue recovered by a core needle may be preserved and the size of the sample is sufficiently large to conduct clinical imaging analysis. However, one of the drawbacks of the core needle is the large force applied by the surgeon can affect the accuracy of the biopsy and damage the micro-architecture of the bone samples.

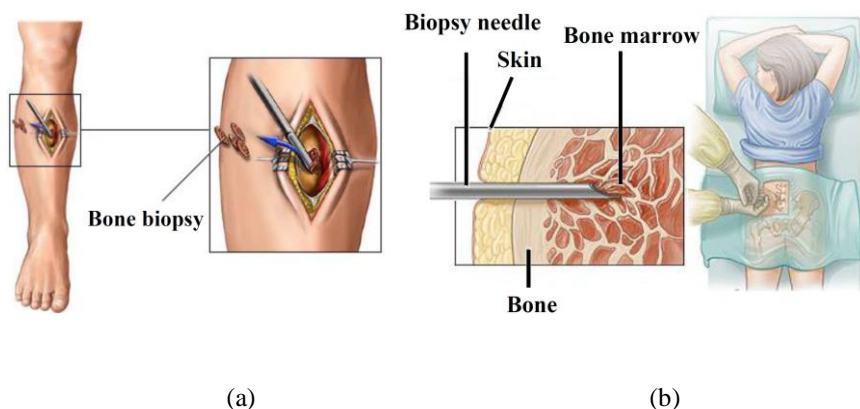


Figure 1.1 Bone biopsy (a) open biopsy [6] (b) closed biopsy: bone marrow biopsy by a core needle [7]

CHAPTER 1

The investigations of power ultrasonics applied for surgical application have been reported since the 1950s [8-13]. Ultrasonic surgical devices have demonstrated many advantages in bone drilling and bone cutting procedures including reducing the cutting force, enhancing precision and reducing the mechanical damage to the surrounding tissues. Consequently, ultrasonic surgical devices have been increasingly used in many surgical procedures, such as oral surgery and maxillofacial surgery [14, 15]. In this study, an ultrasonic surgical needle device is investigated for bone biopsy to improve the accuracy of the biopsy and preserve the tissues surrounding the biopsy site.

1.1 Introduction of ultrasound

Ultrasound is an oscillating sound pressure wave with a frequency above the upper audible limit of the human hearing; the range of ultrasound frequency is normally above 20kHz [16, 17]. Fig. 1.2 shows the sound wave is classed as infrasound, acoustics and ultrasound, based on the ability of the human to hear sound. The frequency range of the sonic wave, which is the sound detection range of the human ear, is from 20Hz to 20kHz. The sound wave with a frequency below 20Hz (the lower limit of human hearing) is defined as infrasonic wave. Infrasonic waves normally occur in earthquakes, avalanches and atmospheric phenomena such as wind and thunder [18-21].

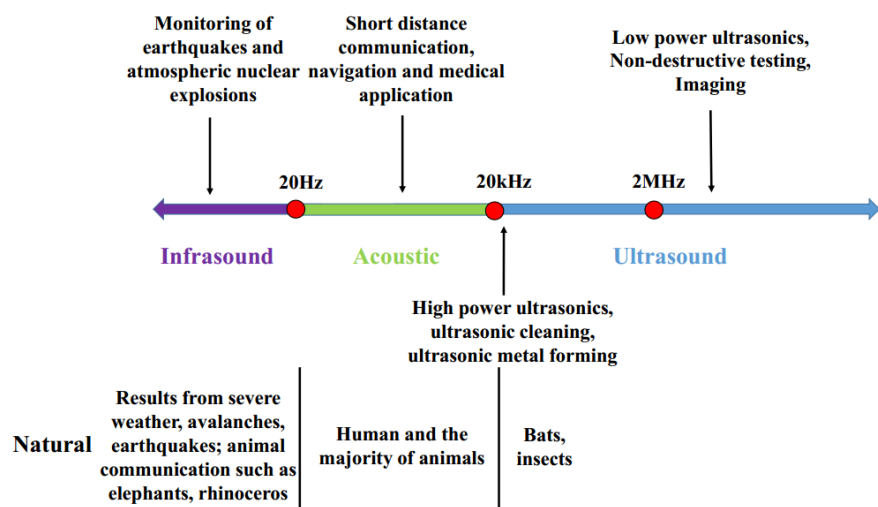


Figure 1.2 Different types of sound waves and their corresponding applications [22, 23]

CHAPTER 1

Ultrasound has been shown to be advantageous in many applications such as metal welding, ultrasonic imaging, non-destructive testing, cutting of hard human tissue, and metal forming [24-26]. According to the range of frequencies and power levels, the applications of ultrasonics can be divided into two groups: low power and high power. Low power ultrasonics does not change the properties of the medium that it propagates through; the frequency range is usually above 1MHz and a typical application is non-destructive testing. It is generally used for detection, exploration and information (e.g., detection of vascular defects, exploration of the properties and structure of minerals, signal transmission) [27, 28]. On the other hand, high power ultrasonics has the ability to change the chemical or mechanical properties of substances, or has a permanent or lasting effect on the medium. The frequencies of high power ultrasonics in industrial applications are normally in the range of 20kHz to 100kHz. High power ultrasonics are applied for example in welding of metals and polymers, food drying and ultrasonic surgical devices [29, 30].

1.2 High power ultrasonic system used in industrial and surgical applications

A typical high power ultrasonic system is shown in Fig. 1.3. It normally consists of two components: the ultrasonic generator and the ultrasonic transducer system (a transducer, a booster and a tool). The ultrasonic generator is used to drive the ultrasonic transducer system, which can transform a low frequency signal (50Hz or 60Hz) to a high frequency signal (20kHz to 100kHz). The high frequency electrical signal from the generator is then supplied to an ultrasonic transducer that converts electrical signal to mechanical vibration. Most efficient transducers use piezo-ceramic elements to generate mechanical vibration. The vibration from the transducer is transmitted directly to an ultrasonic tool that is in contact with the work-piece. In many applications the vibration amplitude of the transducer is not sufficient to meet the working requirements such as bone cutting and ultrasonic welding. A booster is added to the system between the transducer and the ultrasonic tool. The purpose is to increase the amplitude of vibration of the device or provide a convenient holding location for the device.

CHAPTER 1

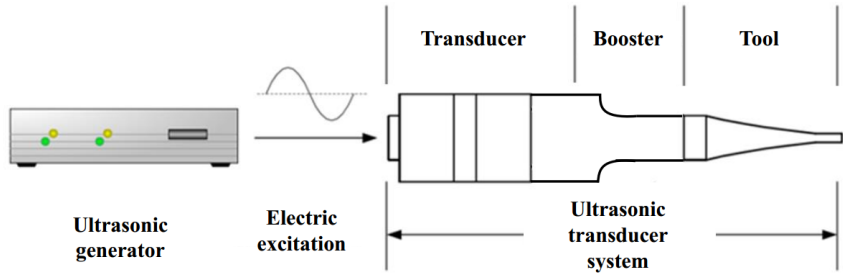


Figure 1.3 High power ultrasonic system

The ultrasonic transducer normally operates in a longitudinal mode, torsional mode or flexural mode. These three vibration modes are illustrated in Fig. 1.4. For the longitudinal mode, the direction of the particle displacement in the medium is parallel to the direction of wave propagation. The torsional mode is the vibrational angular motion and this vibration mode can cause the system to twist. For the flexural vibration mode, the direction of the particles displacement is perpendicular to the wave propagation direction. In general, the whole vibration system (transducer, booster and tool) operates at the tuned frequency with a specific vibration mode. However, some ultrasonic devices also combine the different vibration modes to create a new mode shape such as longitudinal-torsional vibration mode (LT), longitudinal-flexural vibration mode (LF) and torsional-flexural vibration mode (TF). These have demonstrated advantages in many applications, such as ultrasonic motors, ultrasonic welding and ultrasonic drilling [31-34].

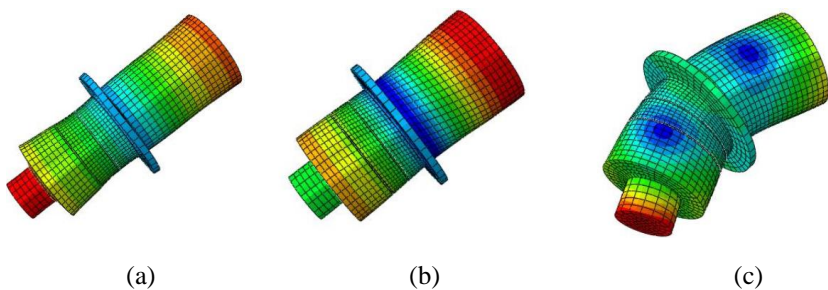


Figure 1.4 Three vibration modes (a) longitudinal mode (b) torsional mode (c) flexural mode

1.3 Ultrasonics in surgical applications

Ultrasonics has been used in medical applications since the 1930s. The first application in the medical field was recorded in obstetrics [35]. Ultrasonics was employed to evaluate

CHAPTER 1

foetal size, maturity and position, which was a fast, safe and reliable method for the diagnosis of pregnancy. After that, ultrasonics was used in other medical fields such as therapy and surgery [36-39].

Ultrasonography is a diagnostic imaging technology using ultrasound to generate the images of body structures including tissues, blood flow and internal organs [40]. It is often employed to assist surgeons in performing surgical procedures such as gynaecological surgery and laparoscopic surgery. Surgeons can clearly observe and understand the internal conditions of the body before performing the operation. For this procedure, a hand-held probe (called a transducer or scan head) is directly placed on and moved over the patient. The body structures are visualised by recording the reflections or echoes of ultrasonic pulses directed into the tissues. This application employs frequencies in the range of 1.6MHz to 10MHz and is a branch of low power ultrasonics [41]. The ultrasonic waves used for medical diagnosis are normally low intensity ($<100\text{mW/cm}^2$) which ensures the physicochemical properties of the tissue do not change. In many ways ultrasonography is an ideal diagnostic tool as it is non-invasive, externally applied and non-traumatic. Moreover, it is quicker, easier and less costly than the Computerised Tomography (CT) scans and Magnetic Imaging (MRI).

Ultrasonic surgical devices were first reported in the mid-1950s for dentistry, where the first experiment was used to examine drilling teeth. Following this, a dental scaler was invented in 1963 based on high power ultrasonics to remove deposits from the surface of teeth, which was considered as a simple and effective way to treat dental calculus [42]. An ultrasonic surgical instrument typically has three main components: an ultrasonic transducer, an ultrasonic horn and a surgical insert. A tapered ultrasonic horn is often connected to the transducer to provide amplitude gain, so that the small amplitude from the transducer, of the order of a few microns, can be increased to several tens of microns at the tip of the surgical insert. The surgical insert may be the front end of the horn or may be another tuned component connected to the horn. For either configuration, the whole device normally operates in a longitudinal mode of vibration at its tuned frequency while ultrasonic surgical devices are also possible to employ LF or LT vibration mode as the operating mode. However, for an ultrasonic surgical drill, if the tip surface of the vibrating surgical insert is relatively large, and the target is hard tissue (bone), it will exhibit poor drilling performance. The reason for this is that the instantaneous pressure from the surgical insert does not exceed

CHAPTER 1

the compressive strength of the bone during each impact, and hence the drill doesn't progress [43]. Additionally, the ultrasonic surgical insert is vibrating at an ultrasonic frequency and is in contact with the target during the surgical procedure. Thus, it may increase the heat generation at the cutting site when an ultrasonic resonant device is used for bone cutting, and this will damage the tissues around the cutting site. In this study, the ultrasonic resonant device refers to the ultrasonic transducer and surgical insert resonating at the same frequency.

1.4 Bone drilling technologies

Drilling of bone is commonly used in two main fields: orthopaedic surgery and biomechanical engineering. In orthopaedic surgery, the most common application of bone drilling is the treatment of bone fracture, which restores the bone fracture parts to their original position and immobilizes them until the fracture parts are completely healed. The hole produced during the bone drilling process is used to fix the fractured parts for immobilization using a screw [44-46]. For bone drilling in biomechanical engineering, it focuses on investigation of bone drilling performance (including required force, required torque and temperature around the drilling site), mechanical strength of the bone and automatic bone drilling instruments [47, 48].

Presently, mechanical rotary drills are normally used for bone drilling, and the rotation speed of the drills varies from 400rpm to 150,000rpm. The rotary drills have the advantages of low force requirements (applied by the surgeon) and rapid drilling through cortical bone (the hardest bone). However, the drawbacks of rotary drills are also apparent. For example, the debris and chips can spread during the surgical process, and this increases the risk of foreign-body-reactions. Moreover, excessive heat generation is produced in the bone tissue. It was reported that temperatures of 89°C up to 185°C were measured around the drilling site, resulting in the bone cellular necrosis [49, 50]. Rotary drills can also damage bone tissues. In drilling tests on rat femoral diaphysis, a large haematoma was observed at the drilling site, indicating that a longer postoperative recovery time was required when using rotary drills for bone drilling [51].

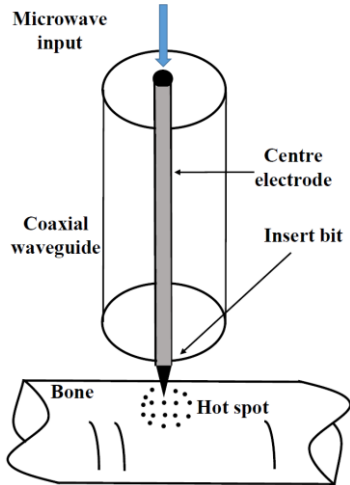


Figure 1.5 Schematic of the microwave drilling system [50]

Many new drilling technologies have been studied to improve the performance of bone drilling. The method of using lasers has been widely studied [52]. Compared to rotary drilling, laser ablation of bone tissue can give highly accurate and clean cuts. However, the cost of laser drills is too high for widespread use in a clinical setting. It has also been reported that laser drilling can induce severe thermal damage in bone tissue. Employment of microwave energy for hard tissue drilling has been studied by many researchers [53-55]. The schematic of a microwave drilling system is shown in Fig. 1.5. The centre electrode radiates the microwave energy and a confined hot spot near the tip of the electrode is generated. The hot spot assists the electrode to drill deeper into the molten area. Rotary motion is not required for this drilling mechanism and there are no vibrating parts in this system. For drilling tests on ovine tibias (cortical bone, 3mm up to 5mm thickness), the results show that a microwave power of 200W is required to penetrate the cortical bone and the operating time is below 5 seconds. There are no debris and chips produced during the drilling procedure. A microwave drill can also improve the cutting accuracy and reduce the mechanical damage to bone tissue compared with a rotary drill. Moreover, the cost of a microwave drill is much less than a laser drill. However, for microwave drills used in bone surgery, the safety of the patient and the surgeon is a significant issue as the microwave radiation may be hazardous. Microwave drilling may increase the risk of causing cancer, however this is still being researched [50].

1.5 Ultrasonic-sonic drilling technology for bone biopsy

To generate sufficient instantaneous pressure, preserve the bone tissue architecture and extract an intact biopsy sample, an ultrasonic-sonic drilling technology is employed in a surgical device for bone biopsy. Ultrasonic-sonic drilling was originally developed for rock drilling in low gravity environments [56-59]. The current research on ultrasonic-sonic drilling technology focuses on planetary exploration. This is the first time that the ultrasonic-sonic drilling method is applied in a surgical application. The ultrasonic-sonic drilling system is shown in Fig. 1.6.

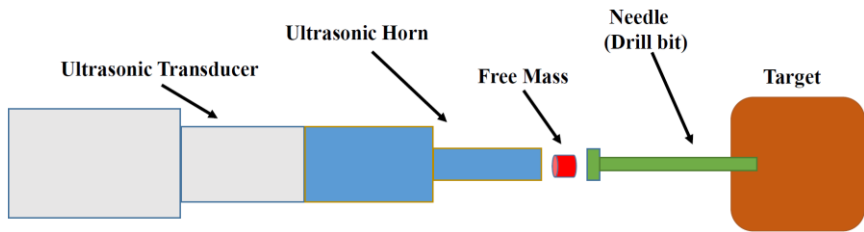


Figure 1.6 Schematic of the ultrasonic-sonic drill

In this methodology, a free mass, in the form of a small piece of metal, is placed between the ultrasonic transducer-horn and the drill bit. The ultrasonic horn impacts the free mass and transfers an impulse to the free mass. Then, the free mass moves forwards to hit the drill bit and delivers an impulse to the drill bit. Lastly, the free mass rebounds to finish one cycle. The drill bit delivers a considerable force to the target in a short time period for each impact. The area under the drilling force-time curve directly affects the rate of progress, determining the interval when the pressure applied by the drill bit exceeds the compressive strength of bone. Accordingly, it has been suggested that the impulse (area under the force-time curve) lying above the force threshold required to exceed the compressive strength of bone, is defined as the effective impulse, in Fig. 1.7, and can be considered as a design parameter to evaluate the drilling performance [43, 58].

CHAPTER 1

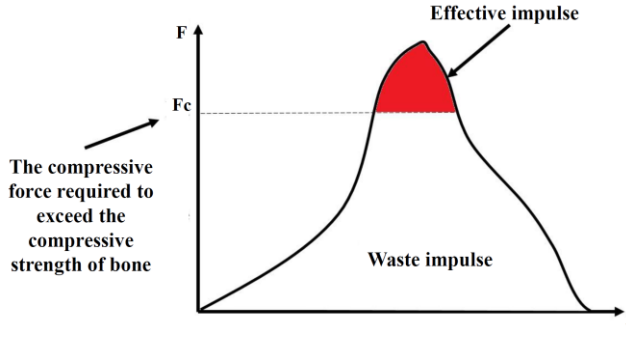


Figure 1.7 The definition of effective impulse [58]

In this work, an US needle for bone biopsy is designed by use of the ultrasonic-sonic drilling technology. For this drilling method, the horn is vibrating at an ultrasonic frequency while the free mass is vibrating at sonic frequencies. Compared to conventional ultrasonic drilling approaches that directly deliver the impulse to the bit, the advantage is that during the interval between two successive impacts the ultrasonic horn recovers its vibration amplitude and thus delivers a nearly consistent impulse to the free mass and drill bit for each impact. Consequently, the ultrasonic-sonic drill can largely improve the rate of progress compared with other ultrasonic resonant devices. The other advantage is that the ultrasonic-sonic drilling approach can reduce the heat generation at the cutting zone therefore reduce the thermal damage to the bone tissue, compared with the ultrasonic resonant drilling method. In the ultrasonic resonant device, the surgical insert resonates at an ultrasonic frequency, while in the ultrasonic-sonic drilling device it vibrates at a sonic frequency. Thus, the friction between the surgical tool and the target is significantly reduced for the ultrasonic-sonic device. The vibration amplitude of the surgical insert in the ultrasonic-sonic device (in millimetre range) is also much larger than that of the ultrasonic resonant device (in micros range). This also helps the ultrasonic-sonic device penetrate the target, reduce the penetration time and hence reduce the heat accumulation. Moreover, it is reported that the ultrasonic-sonic drill for rock drilling requires very low pre-load (<5N) to penetrate the rock [57]. Thus, for the ultrasonic-sonic drilling mechanism used for bone biopsy, it can ensure the micro-architecture of the biopsy sample is preserved and the tissue around the biopsy site remains uninjured.

1.6 Outline of research

A study is presented of an ultrasonic surgical needle designed for bone biopsy, based on an ultrasonic-sonic drilling approach which converts ultrasonic frequency vibration of the horn to sonic frequency vibrations of the needle through a freely vibrating mass between an ultrasonic transducer-horn and a surgical needle. The feasibility of the ultrasonic-sonic drilling mechanism in a surgical application is investigated and the penetration performance is evaluated. This thesis is divided into 7 chapters and the key contributions of the remaining chapters are summarised below:

Chapter 2 is a literature review. The early history of ultrasound is first presented, which reviews the development of ultrasound from the discovery of ultrasound to mature ultrasound technology in practical applications. Then, the surgical applications of ultrasonics are introduced including neurosurgery, vestibular surgery and bone surgery. Bone properties and the development of ultrasonic bone cutting are also explained in this chapter. The advantages and disadvantages of conventional and ultrasonic instruments used for surgical bone cutting are discussed and compared. The current research on biopsy is presented, which focuses on the review of conventional methods for bone biopsy and discussion of their advantages and disadvantages. The studies and modelling approaches of ultrasonic-sonic drilling technology are reviewed. This chapter also demonstrates that the current application of ultrasonic-sonic drilling technology is narrow, only focusing on planetary exploration.

Chapter 3 introduces the methodology of ultrasonic transducer and horn design. The characteristic parameters of the ultrasonic transducer (such as the resonant frequency, vibration mode and wavelength) and materials of ultrasonic transducer parts are first determined based on achievement of high acoustic transmission, low mechanical loss and long lifespan. Then, the Finite Element Analysis (FEA) is employed to simulate the vibrational behaviour of the ultrasonic transducer, followed by a presentation of the steps of developing the transducer finite element model (FE model). To balance the computing resources and the accuracy of the solution, a mesh convergence study of the transducer FE model is conducted to determine the suitable mesh density. The dimensions of each ultrasonic transducer part is optimised and determined through the FE model to ensure the

CHAPTER 1

transducer is resonating at the design frequency with a pure longitudinal motion. The analytical and FEA methods used to calculate the resonant length of different ultrasonic horn shapes are investigated. The resonant length and vibration gain of the different horn shapes achieved by the analytical and FEA methods are in good agreement.

Chapter 4 presents optimisation of the ultrasonic horn and design of the US needle. The shape and dimensions of the ultrasonic horn play an important role in the performance of the US needle because the horn affects the momentum of the free mass and therefore has a great influence on the effective impulse. To maximise the effective impulse delivered to the target, an FE model of the ultrasonic horn impacting the free mass is developed to select the optimal horn for the US needle. The optimised ultrasonic horn and the ultrasonic transducer are assembled and modelled in FEA software Abaqus to ensure the whole device resonates at the design frequency with a pure longitudinal mode. The ultrasonic transducer-horn are manufactured and assembled. Experimental analysis methods (the electrical impedance analysis and the experimental modal analysis) are conducted to evaluate the performance of the ultrasonic transducer-horn. In addition, the FE model of the transducer-horn is validated by the experimental modal analysis. The design of the US needle system is presented and the selection of each component used to form the needle system is discussed.

Chapter 5 discusses the use of finite element analysis and numerical methods to build a one dimensional numerical model for the US needle. The numerical model is used to simulate the dynamic process and optimise the needle system. A MSD modelling method is conducted to build the numerical model of the needle system. Each dynamic component (ultrasonic transducer-horn, free mass and surgical needle) is modelled as a MSD system, which constitutes the whole system dynamic model. The numerical model is validated through experiments, using a prototype needle. The experimental and numerical results have indicated that the numerical model is an adequate model to simulate the US needle system. Moreover, a parametric study (the mass of the free mass, spring pre-load and spring rate) is conducted with the MSD model to maximise the effective impulse and determine the best configuration of the needle system. The optimal configuration of the needle system achieved by the simulation model is also validated by experiments.

CHAPTER 1

Chapter 6 presents the bone penetration tests of the US needle with the optimal configuration. The needle system is employed to conduct penetration tests on biomechanical test samples and fresh ovine femur (trabecular bone and cortical bone). The penetration performance of the US needle is also compared with the conventional trephine needle in terms of the quality of the bone biopsy site and biopsy sample. The penetration tests demonstrate that the US needle can penetrate the hardest bone (cortical bone) and extract a bone biopsy sample with a regular cylindrical geometry and smooth surface. For penetration of cortical bone, the heat generation and rate of progress are also compared between the US needle and an ultrasonic resonant needle. Thermal damage analysis of the US needle used for penetrating cortical bone is also conducted.

Chapter 7 introduces the conclusion of this study and suggestions for the future work.

Chapter 2 Literature review

2.1 Early history of ultrasound

Ultrasound is a term that defines sound waves at frequencies above the range of human hearing, and also defines a branch of the field of acoustics. Although it has been applied in industrial, medical and military fields since the beginning of the 20th century, the foundations of ultrasound were studied and laid in the 19th century. Wollaston was one of the early researchers who studied the pitch limits of audibility, and observed that some insects might communicate by high frequency sound inaudible to the human in 1820. In 1830, Savart developed a large toothed wheel known as Savart's wheel that was the first device to generate ultrasonic waves and could achieve frequencies up to 24kHz [60]. In 1876, Galton invented the whistle that employed edge tones and a resonant cavity to produce the frequencies in the range of 3kHz to 30kHz in air. Galton then used the whistle to investigate the audibility limits of human beings and animals. In addition, another important study of audibility limits was performed by Koenig in 1899. This resulted in the development of the tuning-fork tonometer, which could generate frequencies from 16Hz up to 90kHz [61].

Magnetostriction and piezoelectricity were discovered in the 19th century, and these had a significant influence on ultrasonics in the 20th century. Magnetostriction is a property of ferromagnetic materials that can convert magnetic energy to kinetic energy (or vice versa) during the magnetization process. This effect was first discovered by Joule in 1842 [62]. Piezoelectric materials can generate an electrical charge when a mechanical force is applied. In 1880, French physicists Pierre and Curie discovered the piezoelectric effect in crystals (such as quartz, topaz and Rochelle salt). The magnetostrictive and piezoelectric effects became acoustic sources and receivers in the 19th century and had positive effects on developments in the field of ultrasonics.

In the early 20th century, the work in the field of ultrasound was concentrated on improving the Galton whistle and the development of more advanced detection methods. For example,

CHAPTER 2

an improved version of the Galton whistle was developed by Edelmann, which could generate higher energy of sound. Moreover, frequencies up to 110kHz were recorded by the Edelmann Galton whistle. Underwater sound propagation was investigated at the end of the 1800s and the beginning of the 1900s for the detection of submarines. A well-known work on the detection of submarines was given by Langevin in 1916 in the development of the first underwater sound transducer using the piezoelectric effect. Additionally, Langevin found that small fish in the ultrasonic field were killed, with these observations being the first to indicate the destructive capability of ultrasound [60, 63].

From 1916 to 1926, ultrasonic applications grew steadily, mainly focusing on three fields: underwater uses, communications and the scientific field [61]. After that, research on high power ultrasonics was initiated in 1927 by Wood and Loomis, which was based on Langevin's work. Wood and Loomis had developed a high power oscillator tube (frequency range: 200kHz to 500kHz) which could be used for many high power applications such as drilling, heating and radiation pressure. Furthermore, Wood and Loomis also achieved observations of the modal patterns of tubes and plates and first identified the phase velocity in rods and disks from their experiments. In 1929, the application of ultrasound was first used in two new fields of testing and medicine [35, 64]. Sokolov and Muhlhauser made significant contributions towards using ultrasound for testing materials. Sokolov was the first scientist who employed ultrasound to identify the hidden flaws in metals in 1929, and Muhlhauser published the first patent in the field of ultrasonic non-destructive testing in 1931. In the medical field, a large number of studies were conducted in the 1930s to investigate the biological effects of ultrasound. Freundlich, Sollner and Rogowski suggested the use of ultrasound in medicine for diathermy. Their research results indicated that bone marrow could be heated by the ultrasonic energy, with nearly no influence on the bone.

World War II witnessed the development of sonar technology which played an important role in antisubmarine warfare, the rapid development of ultrasonic non-destructive testing and radar applications. On the other hand, high power ultrasonics developed slowly during this period. Piezoelectric ceramics were introduced after World War II and demonstrated many excellent material properties that facilitated the application of ultrasound in industry. A large number of power ultrasonics applications were developed and realised from scientific research to commercial applications such as cleaning and machining. During the

CHAPTER 2

period 1940 to 1955, there were two important developments for high power ultrasonics. The first was the invention of the ultrasonic horn. In 1950, Mason designed an exponentially tapered rod to amplify the displacement of a resonant transducer. He also conducted material testing for the horn, such as fatigue strength and cavitation resistance. Several different kinds of horns were proposed by Lozinskii and Rozenberg to meet the requirements of various applications. The ultrasonic horn became an important component of high power ultrasonics system, which is still currently widely used in many high power ultrasonics applications. The second significant development was the prestressed sandwich transducer. The basic transducer structure (sandwich type) was proposed by Langevin and then optimised by Miller. In 1954, Miller proposed the mechanical bias concept by a centre bolt to pre-stress a sandwich transducer in compression. This method effectively solved a major problem with piezoelectric ceramics and crystals, which was the low tensile strength of these materials [61]. During this period, studies on high power ultrasonics mainly focused on the following areas: intense ultrasound in liquids (for example cavitation), industrial applications (ultrasonic cutting, ultrasonic cleaning, soldering, and metal welding), the medical field and chemical-biological processes. A large number of low power ultrasonics applications also appeared in 1940-1955. The ultrasonic flow meter was proposed in 1949, although the earliest research indicating use of sound to measure flow was first published in 1931. In the following years, with the development of ultrasonic flow meters, it became a mature technology and was used in industrial applications in 1963 [61]. In 1952, Crawford developed the ultrasonic burglar alarm that utilized high frequency sound waves to detect motion in a specific region. Airborne ultrasound technology was employed as an aid to the blind in 1948, and as a driving aid in severe weather (for example fog) in 1949 [61]. Investigations of ultrasound for medical applications were also an important and popular subject between 1940 and 1955. The range of studies of ultrasound in medicine could be classified into the following areas diagnostics, therapeutics, surgery and dentistry [60, 61, 63-69].

2.2 Review of ultrasonic applications in surgery

Ultrasonics has been applied to many surgical applications such as neurosurgery, cosmetic surgery, vestibular surgery and bone surgery [36, 70-72]. It offers many advantages for these surgeries as it is minimally invasive, safe, and gives precise control.

2.2.1 Ultrasound in neurosurgery

The first application of ultrasonics in surgery was recorded in the field of neurosurgery, which was described by Lindstrom in 1954 [73]. Ultrasonic irradiation was employed as a substitute for lobotomy, and was performed on twenty patients. Sixteen of the patients suffered from severe pain because of metastatic tumours. The intensity of the ultrasonic irradiation was 7W/cm^2 applied for 4 minutes to 13 minutes via a hole in the skull. There were no post-operative complications for all cases and the patients were reported to be in a satisfactory condition.



Figure 2.1 Ultrasonic surgical instrument developed for neurosurgery [74]

In 1954, Fry invented the earliest surgical instrument for focused ultrasonic neurosurgery, as shown in Fig. 2.1 [74]. Fry's surgical instrument contained an array of four transducers and a plane quartz disk in each transducer resonating at 1MHz fitted with a polystyrene lens. It was reported that high intensities could be achieved by this focused ultrasonic device, up to 2.7kW/cm^2 . Fry then improved his device by employing a single piezoelectric element

CHAPTER 2

fixed on a parabolic reflector. This new device could achieve a more focused pattern of radiation. In 1965, Fry conducted a series of studies on 87 patients treated with ultrasonics, mainly in the treatment of Parkinson's disease. There were several incisions made in each patient to expose the suitable volume for destruction. An intensity in the range of 400W/cm^2 to 1200W/cm^2 was applied to the exposed area and persisted for a few seconds. However, the results were not completely satisfactory. There were 15 patients who suffered post-operative complications. One patient did not respond to the ultrasonic irradiation, although the patient's condition improved when the pituitary was removed surgically.

Nowadays, the Cavitron Ultrasonic Surgical Aspirator (CUSA) has been widely used in neurosurgery to remove brain tumours. Ultrasonic aspiration was first used in neurosurgery in 1976, in the United States; it was found that ultrasonic aspiration did not produce harmful physiological effects on nervous tissue [75, 76]. The CUSA system could generate ultrasonic frequency vibrations in the range of 23kHz to 35kHz and the vibration amplitude of the tip is usually operating at 100 microns to 300 microns. During the ultrasonic aspiration procedure, two effects occur to rupture and fragment the tissue. One is due to the vacuum effect: the tissue is in contact with the vibrating surgical tip which is able to tear the targeted tissue from the surrounding tissues. The other one is the effect of cavitation: the vibrating surgical tip produced localized pressure waves that could generate transient cavitation bubbles in the tissue. Then, the bubbles could burst and assist the rupture of the tissue. The major advantage of the CUSA system is that it can rapidly remove the brain tumour with minimal manipulation of the surrounding tissue. Compared to the traditional suction and cautery loop, ultrasonic aspiration has the following advantages: preservation of brain vessels and nerves, reduction of thermal damage and increased safety [77].

2.2.2 Ultrasound in vestibular surgery

Meniere's disease is caused by a disorder of the vestibular end organ, which is harmful to the inner ear and can result in vertigo, tinnitus and a loss of hearing. People aged 20 to 60 are more likely to suffer from Meniere's disease, and it is also reported that females are more likely to get this disease. In 1960, James reviewed many conventional surgical alternatives to cure Meniere's disease. However, none of the alternatives were completely satisfactory. For example, the patient was at high risk during the operation, potentially resulting in the

CHAPTER 2

loss of their hearing. Krejci made great contributions towards the treatment of Meniere's disease. Krejci conducted experimental work on the employment of ultrasonic irradiation to treat a patient suffering from Meniere's disease. The results showed the symptoms of the disease were cured and the patient's ability of the hearing was retained [78, 79].

The ultrasonic method used to cure Meniere's disease is routinely used for routine clinical use, with the corresponding surgical systems being well developed. Most of the instruments operate at frequencies from 1MHz to 3MHz with an ultrasound intensity in the range of 3.6W/cm^2 to 22.3W/cm^2 . The main risk of this approach is that it has the potential to damage the facial nerve, which is close to the operation site. Although the facial nerve is not irradiated, it may be heated by thermal conduction from the irradiated areas. It has been reported that the maximum ultrasound intensity applied to the operation area should be below 22W/cm^2 . This ensures the temperature of the facial nerve will not rise above 48°C , preventing nerve damage [39].

2.2.3 Ultrasound in bone surgery

The cutting of human bone is a significant operation in surgery, which is used in a large number of medical applications. The common medical applications of bone cutting include osteotomy and bone biopsy. Bone cutting can be conducted with different surgical tools, either manual (bone chisels and pliers) or powered (rotary burrs and electrical saws). However, it is still a challenge for surgeons to perform precise and safe bone cutting by use of these conventional surgical tools due to the hardness of the bone tissue. To obtain high precision bone cutting and improve the safety during the procedure, ultrasonic cutting has been investigated and used in bone surgery.

2.2.3.1 Introduction of bone

Bone structure

Bone protects the various organs and helps support the body. It can produce red and white blood cells and store minerals. Bones have different shapes and sizes and it is impossible to find two identical bones in nature. From the view of the anatomic structure, there are five

CHAPTER 2

types of bones in the human body: long bone, short bone, flat bone, sesamoid bone and irregular bone. Although bone has great dissimilarities, all bone tissues are composed of the same components: minerals, water and organic phases. The mechanical properties of bone depend on the distribution of these three components. Moreover, the structure and composition of bone are determined by many factors such as the different site, physiological function and the age, sex and health of the subject. Generally, bone tissue can be divided into two types: cortical bone and trabecular bone [80]. The structure of bone is shown in Fig. 2.2.

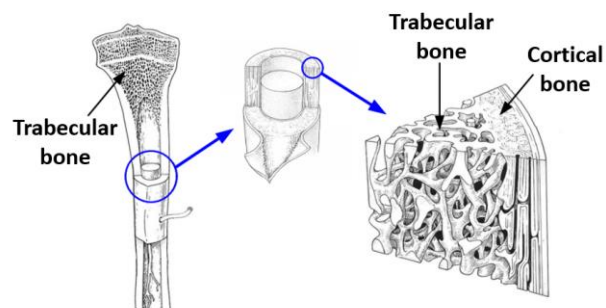


Figure 2.2 Bone structure: cortical bone and trabecular bone [81]

Cortical bone is also called compact bone and lies in the outer layer of the bone. It makes up 80% of skeletal mass and it is strong and dense [82]. The porosity ratio of cortical bone is in the range of 5% to 30%. The main function of cortical bone is to protect the vital organs, support the body and store minerals. Therefore, cortical bone is very difficult to cut and penetrate. Trabecular bone is also known as cancellous bone. It is surrounded by compact bone and is weaker, lighter, and less dense than compact bone. The porosity ratio of trabecular bone is up to 90%. It makes up a larger volume of the bone compared with the cortical bone. Consequently, the trabecular bone is less difficult to cut or penetrate than the cortical bone [81].

Mechanical properties of cortical bone

Bone is an anisotropic, hierarchical and heterogeneous material. There is a large amount of research investigating the properties of bone. It is well established that the material behaviour of cortical bone is orientation-dependent. Fig. 2.3 illustrates the three mutually

CHAPTER 2

perpendicular directions of a femur cortical bone (longitudinal, radial and circumferential directions). The mechanical properties of cortical bone are different along the three different directions. However, many studies indicated that the difference in bone properties between the radial and circumferential directions is small [81, 83]. Consequently, the majority of researchers have concluded that cortical bone can be considered as a transversely isotropic material (an orthotropic material). Additionally, researchers also have demonstrated that bovine femoral cortical bone in the longitudinal direction has a higher stiffness and strength than the transverse direction. This means that cortical bone has higher Young's modulus and higher ultimate stress in the longitudinal direction.

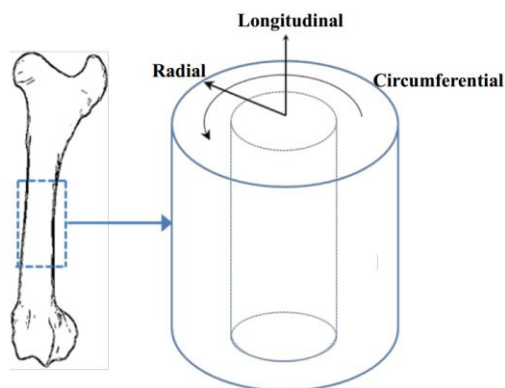


Figure 2.3 Three mutually perpendicular directions of a femur cortical bone [81]

Thermal damage of bone

For bone surgery such as bone cutting and drilling, the friction between the surgical tool and the tissue can generate heat. It is very important to control the cutting temperature during the cutting process because bone tissues will become necrotic and irreparable if the cutting temperature exceeds the safe range. According to Lundskog's experimental results, cellular necrosis could occur if the cutting temperature reaches 52°C to 55°C and lasts for more than 30 seconds [84]. A large body of literature explains bone death due to high temperature during the cutting process. However, the exact temperature of bone cellular necrosis is not constant. It can be considered that bone cell death could be induced in the temperature range 52°C to 55°C where the exposure time is longer than 30 seconds but it is possible for bone to survive higher temperatures, reportedly up to 70°C , if the exposure time is very short.

CHAPTER 2

Abouzgia reported that the cutting temperature and the duration of temperature rise could be reduced if the applied cutting force was high, which resulted in a faster cut [85-88].

2.2.3.2 Review of ultrasonic cutting in bone surgery

The evolution of the ultrasonic surgical system was paralleled to the development of ultrasonic machining for industrial applications. The year 1945 saw an ultrasonic impact grinder invented by Balamuth which was used for machining hard and brittle materials such as ceramic and glass [89]. Balamuth and Catuna also proposed a new application of the ultrasonic grinding system for cutting cavities in extracted teeth, which was the first report of ultrasound in dentistry and introduced ultrasound for cutting mineralized tissue. Following this a miniaturized dental device was designed to remove the calculus from teeth based on the same principle. Compared to the conventional pneumatic-powered device, the ultrasonic dental device offered the following benefits: it reduced tissue heating, preserved the tissue surrounding the surgical site and reduced the pain of the patients. However, Balamuth and Catuna's dental device did not achieve success in commercial applications due to the high cost of the system and the use of abrasive paste restricted surgeon's vision. In the early 1960s, an ultrasonic cutting device without use of the abrasive paste was used to perform bone cutting experiments by Mararow and McFall [89]. Both of them conducted the cutting experiments on animals and compared the cutting performance between electric powered saws/burrs and an ultrasonic scalpel device. The studies conducted by Mararow and McFall indicated that the ultrasonic scalpel device had similar advantages to that of the ultrasonic grinder device. However, Mararow also found that the ultrasonic scalpel device resulted in a slower material removal rate and healing rate, and McFall also confirmed the slower healing rate. At the end of their study, it was reported that saline was introduced to the cutting process, which significantly reduced the healing time. These studies indicated that the ultrasonic device may be a suitable choice for surgical procedures requiring high precision.

The first publication to report human osteotomies performed by an ultrasonic device was in 1974 by Volkov [89]. The ultrasonic device designed by Volkov operated at frequencies in the range of 25kHz to 35kHz with a longitudinal mode. Volkov's device was used to perform osteotomies generating smaller incisions than conventional mechanical devices. It reduced

CHAPTER 2

the damage to the tissue and simplified the procedure. Volkov also reported high cut accuracy and normal regeneration rates in bone were also obtained. Two other studies by Horton (1970) and Aro (1980) also proved that ultrasonic devices could achieve precise cuts and reduce trauma at the operating site when compared with conventional devices [89]. These studies confirmed the slow cutting rate of ultrasonic devices. Several disadvantages of ultrasonic devices were reported by Horton and Aro: difficulty in operation because of the size and shape of the device, overheating and manual adjustment of the optimal operating frequency.

Although the ultrasonic cutting technology had been widely used in industry by the mid-1990s such as textile cutting and food cutting, it still had several limitations preventing its utility in bone surgery. Comparison of the cutting performance between ultrasonic devices and conventional surgical tools had been studied throughout the 1990s. Khambay and Walmsley designed an ultrasonic bone chisel to investigate the cutting rate [90]. The study revealed that a cutting rate of 26mm/min to 110mm/min could be achieved by ultrasonic chisel while a higher cutting rate 48mm/min to 185mm/min was recorded by the conventional surgical device (rotary burrs). Moreover, the ultrasonic devices showed excellent performance on reduction of cutting force, requiring a cutting force ranging from 1.48N to 3.22N during the process of cutting bone. For manual bone cutting instruments, it required hundreds of Newtons of force to perform bone cutting [81].

Many advanced ultrasonic cutting devices have been developed since 2000, which solved many limitations of ultrasonic devices demonstrated between the 1960s and 1990s. Meanwhile, finite element analysis facilitated the development of ultrasonic surgical devices, which was an efficient and reliable tool used to design the ultrasonic devices. It allowed the designer to optimise the devices by accurate prediction of the vibrating modes, resonant frequencies and distribution of stress. Modern manufacture technology enables fabrication of ultrasonic devices with more complex geometry and ensures the high precision of devices.

2.2.3.3 Conventional and ultrasonic bone cutting instruments

The conventional instruments used for bone cutting can be classified as two categories: hand operated tools and electrical bone cutting devices. For the manual bone cutting tool, thermal

CHAPTER 2

damage to bone tissues is much less than electrical bone cutting devices. However, large amount of force is required to cut bone, which may result in uncontrolled damage to the bone and the surrounding tissues. For example, in bone biopsy, the large forces (applied by the operator) can cause large haematoma in the soft tissue surrounding the biopsy site and may also damage the micro-architecture of the biopsy sample. The common manual bone cutting instruments such as bone cutting forceps, bone biopsy needle, amputation saw and bone chisel are shown in Fig. 2.4.



Figure 2.4 Manual bone cutting instruments (a) bone cutting forceps (b) bone biopsy needle (c) amputation saw (d) bone chisel

The core-needle (in Fig. 2.4(b)) is a conventional surgical instrument that is used to penetrate hard tissue to extract a tissue sample. The typical application of a core-needle is bone biopsy and the trephine needle utilizes a cutting surface on its leading edge to penetrate bone. During the biopsy procedure, the combined effect of considerable force in the travel direction and an intermittent repetitive twisting motion is applied to penetrate bone by the surgeons. The twisting motion results in the needle travelling with a large conical orbit and thus produces a hole that is larger than the outer diameter of the needle. This usually damages the soft tissue surrounding the operation site; the disadvantages of the conventional bone biopsy needle have been explained in Chapter 1.

Electrical bone cutting devices (such as the electrical bone drill and saw) are shown in Fig. 2.5. These devices can greatly improve the speed of cutting. However, a large amount of heat is generated during cutting process and the extent of the thermal damage to bone tissues

CHAPTER 2

is determined by many factors such as the geometry of the devices, cutting speed, depth of cut and bone density. Furthermore, the electrical surgical devices may entrap the surrounding soft tissues during the bone cutting procedure and seriously damage the muscles, nerves and blood vessels, especially at sites that are difficult to access [91].



Figure 2.5 Electrical bone cutting devices (a) electrical bone drill (b) electrical bone saw

Ultrasonic cutting instruments normally utilize a cutting tool vibrating at ultrasonic frequencies to make a precise cut on biological tissue. The main advantages of ultrasonic bone cutting are summarized as follows [89, 91-98]:

- Reduction of cutting force and improvement of cutting accuracy: the ultrasonic bone cutting device can significantly reduce the cutting force compared with the conventional bone cutting devices especially the manual surgical instruments. It is reported that the applied force required to cut bone by the ultrasonic-assisted drilling technology is in the range of 20N to 40N depending on the drilling speed, feed rate and the vibration amplitude of the ultrasonic device. However, the manual surgical tools normally require hundreds of Newtons of force to perform bone cutting. Reducing the cutting force is helpful for the surgeons to control the surgical device and improve the cutting accuracy. The microvibrations of the cutting inserts also allow surgeons to make precise and narrow bone cuts.
 - Reduction of the damage to the surrounding tissue: a large number of publications have demonstrated that ultrasonic surgical instruments can reduce the injury of surrounding tissue at the cutting site. For example, comparison of the ultrasonic cutting device and conventional oscillating saw in bimaxillary orthognathic surgery

CHAPTER 2

was performed by Spinelli. In this study, it was observed that the patients had less postoperative inflammation and pain when the ultrasonic cutting device was used in the operation.

- Reduction of bleeding: compared with the conventional surgical burrs and saws, low bleeding is achieved during bone surgery by the ultrasonic cutting devices and it is reported that blood loss can be reduced by 30% to 40%. This is because the combined effects of frictional heat and ultrasonic energy contribute to seal the blood vessels around the surgical site.

Fig. 2.6 shows a typical configuration of an ultrasonic bone cutting device. It consists of two main components: the generator and the acoustic unit. For this commercial ultrasonic cutting device, the cutting tool is vibrating at 22.5kHz in the longitudinal direction by the effects of piezo-ceramic materials and the vibration amplitude of the cutting tool is in the range of 35 μm to 300 μm . Additionally, the cutting tool can be changed according to different applications. It is indicated from clinical reports that this product can make fine and precise cuts, preserve the surrounding soft tissue and improve bone healing.



Figure 2.6 Ultrasonic bone cutting instrument: Misonix BoneScalpel (Misonix Corp.)

2.3 Research on biopsy

Biopsy is a surgical procedure to extract a tissue sample from the living body for diagnosis. There are various types of biopsies, such as bone biopsy, bone marrow biopsy, liver biopsy and kidney biopsy. Biopsy is usually performed by open biopsy and needle biopsy, as

CHAPTER 2

explained in Chapter 1. The first diagnostic biopsy was performed by Rudnev in 1875 and surgical biopsies were widely used in the early 1990s [99].

A study in the comparison of open biopsy and needle biopsy were performed by Heeten [100]. In this study, 206 bone biopsy samples were extracted from 136 patients, including 99 biopsy samples from open biopsy and 107 biopsy samples from needle biopsy. The 136 patients were made up of 73 males and 63 females. The ages were ranging from 5 years up to 82 years and the average age was 30.5 years. Bone biopsies were performed on different parts of the body such as femur, tibia, fibula, skull, ribs and humerus. In retrieving adequate bone biopsy samples used for diagnosis, the results of open biopsies (98% diagnostic accuracy rate) were superior than needle biopsies (70% diagnostic accuracy rate). A similar result was also published by Schajowicz who conducted 7165 needle biopsies and achieved 5231 adequate bone biopsy samples (73% adequate samples) [101]. In literature, the diagnostic accuracy rate was reported ranging from 69% to 88% for needle biopsies used for diagnosis of musculoskeletal lesions [102-104]. Although open biopsy offered adequate biopsy samples with a higher accuracy rate, it also increased the risk of local complication. Murphy found that the complication rate of open biopsy was up to 16%, most commonly tumour spread and hematoma. On the other hand, the complication rate of fine needle biopsy was proved to be below 1%, and the core needle biopsy gave the complication rate from 0 to 7.4%, including hematoma, bleeding and infection [105, 106]. Moreover, the cost of open biopsy is also much more expensive (\$4321.25 to \$7234.00, in the year of 2001) than needle biopsy (average \$1106, in the year of 2001). Needle biopsy is less invasive than open biopsy and it is usually performed under local anaesthesia. However, during the process of core needle biopsies, patients still experience high levels of pain. It was reported by Valebjorg that 167 patients experienced serious pain during the core needle biopsies, accounting for 91% of the total participants (184 patients). Moreover, residual pain lasted 3 days to 4 days in 75% patients [107]. A large haematoma was observed in the soft tissue around the biopsy site using a core needle [93]. This was caused by the needle movements and the large forces applied to the needle, which were required for the biopsy.

Needle biopsy is less invasive, fewer complications and less cost than the open biopsy, and it has widely replaced open biopsy [108]. The main disadvantage of needle biopsy is the low accuracy of achieving an adequate biopsy sample for diagnosis, which is due to the needle

CHAPTER 2

being applied with a large force and an intermittent repetitive twisting action, which can damage the structure of the biopsy sample. It is necessary to explore a new method to address the drawbacks of the current bone biopsy approach. Ultrasonic surgical devices have shown advantages in bone cutting, including preserving the soft tissue surrounding the cutting site, enhancing precision and accuracy, and reducing forces applied to the device compared with bone saws or bone burrs. In this work, an ultrasonic-sonic drilling method is studied and used to investigate the feasibility of high power ultrasonics for bone biopsy.

2.4 Research on ultrasonic-sonic drilling method

2.4.1 The invention of the ultrasonic-sonic drilling method

The ultrasonic-sonic drilling method was invented in 2000 by NASA Jet Propulsion Laboratory, which was used to develop an ultrasonic-sonic drilling-coring (USDC) device for planetary sample acquisition [57]. For exploration missions to Mars, it was crucial to conduct sampling, in-situ analysis and possibly return the samples to Earth for analysis. The first prototype was invented in April 2000 with a weight of 0.7kg. The second generation drill with a weight of 0.4kg was developed and used for the Sojourner Rover to collect rock samples [109]. The USDC device is shown in Fig. 2.7. The major limitations of the conventional drilling approaches used for Mars sampling or sampling in other low gravity environments were the requirement of high axial force, high power consumption and heavy weight. It has been reported that the USDC device could efficiently solve these limitations: required low pre-load (<5N) and low power (5W) to penetrate rocks and retrieve samples. Due to the high performance of piezo-ceramic materials on operating at extreme environments, the USDC device has demonstrated that it could operate over a wide temperature range from 200°C to 500°C. It was also suggested by the inventors of the USDC that the ultrasonic-sonic drilling mechanism may have potential applications in the field of medicine. For example, the ultrasonic-sonic drilling devices could be used for delicate surgeries such as tissue cutting, which normally requires a low force (applied by the surgeon) to prevent organs or surrounding tissues damage.

CHAPTER 2



Figure 2.7 USDC device mounted on the Sojourner Rover for rock drilling [109]



Figure 2.8 A rotary-hammering drilling and coring device used to conduct penetration tests on limestone [110]

The main components and the working principle of the ultrasonic-sonic drilling system have been explained in Section 1.5. The key feature of this drilling method is that the free mass is used to conduct frequency reduction, which converts the ultrasonic vibration of the horn tip to a sonic hammering of the drill bit. For the USDC device used in planetary explorations, the ultrasonic transducer-horn is driven at 20kHz and the cyclic rebound frequencies of the free mass are in the range of 60Hz to 1000Hz. It has been reported that the presence of the free mass could greatly improve the drilling performance [111]. The USDC device has demonstrated that it could be used to penetrate different types of rocks such as granite, basalt and limestone. Additionally, a rotary-hammering drilling and coring device was also developed by the NASA Jet Propulsion Laboratory for deep penetration, which was achieved

CHAPTER 2

by the combination of USDC devices to produce percussive action and an electric motor to generate rotation motion [110]. The rotary-hammering device could penetrate rocks as deep as 3m to 5m. Fig. 2.8 shows the rotary-hammering drilling and coring device used to penetrate limestone and achieve a core with a length of 97.25mm.

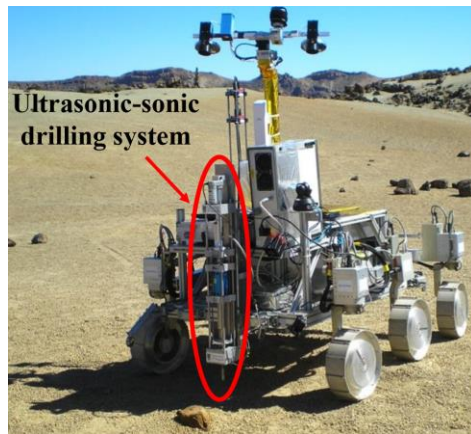


Figure 2.9 Ultrasonic planetary core drill mounted on EADS Astrium's Bridget testbed [59]

The ultrasonic-sonic drilling mechanism has also been studied by other researchers. Harkness developed an ultrasonic-sonic drill for rock drilling (in Fig. 2.9) and proposed the concept of effective impulse to evaluate the drilling performance in 2010 [43, 58]. The different configurations of the ultrasonic-sonic drill were also investigated by Harkness to achieve the maximum effective impulse and improve the drilling performance. The ultrasonic-sonic drilling device was used to perform drilling tests on various rocks such as pumice, low-density vesicular basalt and rheomorphic ignimbrite. The test results indicated that excellent progress and a clean cut could be achieved. In 2013, Quan investigated the ultrasonic-sonic drilling mechanism and designed a corresponding prototype, which was still used for planetary exploration. In Quan's study, the ultrasonic transducer-horn was first analysed and designed based on Mason's equivalent circuit and the impacts between the horn tip and free mass, free mass and drill bit were investigated. The pre-load and the configurations of the drill bits (such as conical, cylindrical and hollow cylindrical drill bits) affecting the drilling performance were also studied through rock drilling tests, which were compared by the drilling depth. Yang and Potthast also employed the ultrasonic-sonic drilling mechanism to design a drilling tool for space application [112]. The current researches on ultrasonic-sonic drilling system are mainly focused on the application of

CHAPTER 2

planetary exploration and the size of these devices are normally large. In this work, the ultrasonic-sonic drilling mechanism is employed to develop a device for surgical application with a small size.

2.4.2 Modelling of ultrasonic-sonic drilling system

A large number of studies on ultrasonic-sonic drilling systems have focused on demonstrating a low applied force and a low power consumption required for ultrasonic-sonic devices to extract rock samples. However, it is also necessary to optimise each dynamic component of the ultrasonic-sonic drilling system and determine the best configuration of the drilling system (the mass of free mass, spring rate and pre-load) to improve the drilling performance.

To evaluate the performance of various configurations and study the dynamic behaviour of this drilling mechanism, the ultrasonic-sonic drilling system for rock drilling has been simulated by different methods. The optimal configuration of the rock drilling system was determined by the numerical model of the ultrasonic-sonic drilling system, which could ensure the drilling system penetrated rocks. The numerical model used to simulate the ultrasonic-sonic drilling system was first proposed by researchers from Jet Propulsion Laboratory. Several independent models were developed to describe the interactions between the main elements and then these simulation models were integrated as a one-dimensional software program to analyse the performance of different designs [57]. Potthast employed the finite element method to develop 2D-axisymmetric models to describe the interactions of the transducer tip, the free mass and the drill bit. This method was difficult to implement because of the convergence problem and long computation time [112]. A one dimensional numerical model was also developed to simulate the ultrasonic-sonic drilling system by Harkness. The drilling force delivered to the target was recorded and then compared with the experimental results. Harkness also proposed the concept of effective impulse that was used to verify the accuracy of the numerical model and evaluate the drilling performance of the ultrasonic planetary core drill [58].

Chapter 3 Methodology of ultrasonic transducer and horn design

The ultrasonic transducer and horn have a significant influence on the performance of the US needle since the effective impulse delivered to the target largely depends on the momentum of the free mass achieved from impact with the ultrasonic transducer and horn. Consequently, the ultrasonic transducer and horn should be designed to transfer optimum momentum to the free mass.

Ultrasonic transducers were originally designed by 1D analytical model and experimental prototypes [113]. The geometry of an ultrasonic transducer was calculated by the solution of the wave equation in the 1D analytical model. The experimental prototypes were used to characterise the performance of the transducer and validate the 1D analytical model. However, there were many disadvantages in using a 1D analytical model to design ultrasonic transducers, such as unrealistic assumptions, high cost of fabricating different prototypes and time consuming repeated experiments. With the development of computing technology, the Finite Element Method (FEM) is increasingly employed to design and analyse ultrasonic transducers as a 2D/3D numerical model [114-116]. FEM can solve complex geometry problems with high accuracy and thus it is normally adopted for ultrasonic transducer design.

In this chapter, the resonant frequency, vibration mode, wavelength and materials of the ultrasonic transducer were first determined based on achievement of high acoustic transmission, low mechanical loss and long lifespan. Then, the ultrasonic transducer was designed and optimised by Finite Element Analysis (FEA) to ensure the transducer operated at the tuned frequency with a pure longitudinal mode. The dimensions of the optimised ultrasonic transducer for the US needle were achieved from the FE model of the transducer. Lastly, the analytical and numerical methods were used to design different shapes of ultrasonic horn. These horn shapes were employed in Chapter 4 to select the optimal configuration of the ultrasonic horn for the US needle.

3.1 Design of Langevin ultrasonic transducer

Langevin ultrasonic transducers, also called sandwich transducers, are widely used in high power ultrasonic applications [117-120]. This kind of transducer typically consists of piezo-ceramic rings, electrodes, a bolt, a back mass and a front mass. The piezo-ceramic rings are sandwiched between the back and front mass, which are clamped by the prestressed bolt. The structure of a Langevin ultrasonic transducer is shown in Fig. 3.1. The piezoelectric elements convert electrical charge to mechanical vibration energy. The vibration amplitude of the transducer has maximum value when the driving frequency is the resonant frequency of the ultrasonic transducer. The steps of the ultrasonic transducer design are summarised in the following sections.

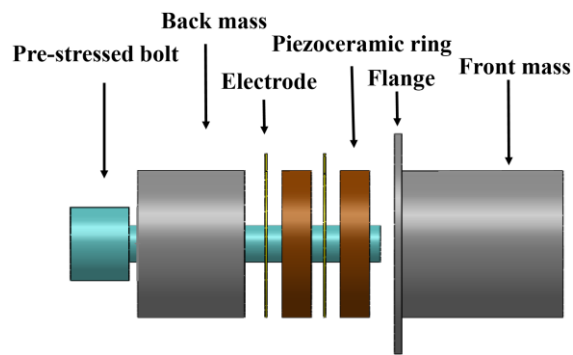


Figure 3.1 Schematic of the structure and components of a Langevin ultrasonic transducer

3.1.1 Determination of the resonant frequency, vibration mode and wavelength

The operating frequency of a high power ultrasonic transducer is normally in the range of 20-100kHz, depending on the application. For surgical applications, ultrasonic surgical devices are usually operating at a frequency between 20kHz and 60kHz to cut biological tissue, such as cortical bone and trabecular bone [14, 121]. The operating frequency of the transducer directly determines the size of the transducer: an ultrasonic transducer with a lower operating frequency is generally longer in dimension compared with a transducer with a higher operating frequency. In this work, the transducer is designed to operate at a frequency of 50kHz. For this frequency, the length of the US needle is estimated to be

CHAPTER 3

120mm based on the estimated dimensions of ultrasonic transducer, ultrasonic horn, free mass and biopsy needle. This is a suitable size for a surgeon to operate. Moreover, compared to the device operating at 60kHz, the needle system with a 50kHz operating frequency can deliver more effective impulse to the target. In practical applications, the ultrasonic transducer generally utilizes longitudinal mode (ultrasonic drilling, ultrasonic cutting), torsional mode (ultrasonic machining and ultrasonic welding) and flexural mode (ultrasonic motors). It is also possible to combine two vibration modes to achieve the expected performance, such as longitudinal-torsional, longitudinal-flexural and torsional-flexural modes of vibration [122-127]. For the ultrasonic-sonic drilling mechanism, there is a free mass oscillating between the horn and surgical insert. The ultrasonic transducer-horn impacts the free mass. Then, the free mass obtains momentum and moves forward to transfer its momentum to the surgical insert. Consequently, the longitudinal mode of vibration is selected because it can transfer the largest momentum to the free mass compared with the other vibration modes.

In an ultrasonic resonant system, the ultrasonic components (such as ultrasonic transducer, booster, horn and tool) are usually designed as a half-wavelength device. The advantage is that the stress at the interfaces between different ultrasonic components is zero in an ideal case, as shown in Fig. 3.2 [128]. Each half-wavelength component of the ultrasonic system can be designed independently based on the specific resonant frequency and then assembled together to form the whole ultrasonic device. The high power ultrasonic transducer used in this work is designed as a half-wavelength device vibrating at 50kHz in the 1st longitudinal vibration mode.

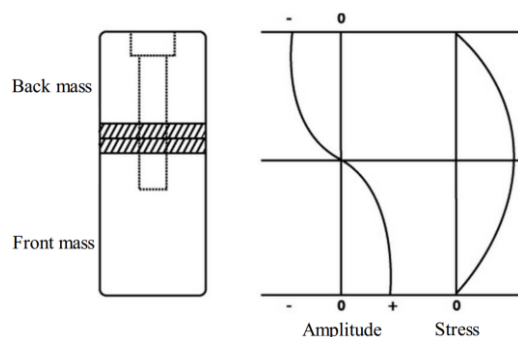


Figure 3.2 The relationship between the vibration amplitude and stress distribution of the ultrasonic transducer [128]

3.1.2 Determination of piezo-ceramic rings

Piezoelectric materials generate electrical charge when a mechanical force is applied, and vice versa. Most high power ultrasonic transducers employ piezo-ceramics that have the following properties: low dielectric loss, high Curie temperature, high mechanical quality factor, high electromechanical coupling factor and relatively stable performance under high power conditions [129, 130].

At present, the most popular piezo-ceramic material is lead zirconate titanate (PZT) that is categorised based on two factors: the chemical composition and the specific application condition. PZT-4 and PZT-8 compositions are usually selected as the piezoelectric element of high power transducers. PZT-8 is particularly recommended for ultrasonic drilling and welding because of the low mechanical loss and excellent dielectric stability under high electrical field [131-133].

Piezo-ceramics have many different shapes, such as plate, disk and ring. For Langevin ultrasonic transducers, a central bolt is used to clamp the back mass, piezo-ceramic rings and front mass. Thus, ring shaped piezo-ceramic materials are adopted. The dimensions of the piezo-ceramic rings are determined by the required output amplitude of vibration, the vibration mode and the application of the transducer [122]. In the case of high power ultrasonic transducers operating in a longitudinal vibration mode, the diameter of the piezo-ceramic rings should be less than a quarter-wavelength to avoid lateral coupling [134]. The total thickness of the piezo-ceramic rings is usually less than one tenth of the one wavelength ultrasonic device to achieve a high electromechanical coupling [122]. The displacement of each piezo-ceramic ring is small and thus multiple piezo-ceramic rings are assembled in series to achieve higher displacement.

To select the suitable dimensions of the piezo-ceramic rings, the length of the one wavelength ultrasonic device is initially calculated to be 101mm. Two PZT-8 equivalent piezo-ceramic rings (CeramTec GmbH, SonoX P8, 20mm outer diameter, 8.2mm inner diameter diameter and 4mm thickness) are selected based on the dimensions requirements of the piezo-ceramic rings and achievement of the high output energy. The diameter of the piezo-ceramic ring (20mm) is smaller than a quarter-wavelength (25.3mm). The total

CHAPTER 3

thickness of the two piezo-ceramic rings is 8mm, which is also less than one tenth of the wavelength (10.1mm).

3.1.3 Material selection for back mass and front mass

The piezo-ceramic rings generate the ultrasonic vibration, constituting the vibrational generator. The metal parts (front mass and back mass) are the vibrational transmitter. When the acoustic wave arrives at the boundary between two media, part of the acoustic wave will be reflected back to the medium that it came from [135]. To reduce the reflection of the acoustic wave, the ultrasonic transducer is usually designed to obtain the largest acoustic energy transmission and thus the materials of the transducer should be acoustically matched. A large acoustic energy transmission can be achieved when the acoustic impedance is matched well for piezo-ceramic material, back mass and front mass. The following equation is used to achieve optimum acoustic impedance matching [130, 136].

$$Z_p = \sqrt{Z_b Z_f} \quad (3.1)$$

Where Z_p , Z_b and Z_f represent the acoustic impedance of the piezo-ceramic material, back mass and front mass, respectively. The acoustical impedances of the materials usually used for the transducer design are listed in Table 3.1 [130, 135, 137].

Table 3.1 Acoustic properties of the materials for the transducer design

Material	Acoustical impedance ($\text{kg/m}^2/\text{s}$)
PZT8	29.9×10^6
Titanium alloy Ti-6Al-4V	31.54×10^6
Stainless steel (316)	39.21×10^6
Duraluminium	14.04×10^6
Tool steel	41.50×10^6

Applying the data in Table 3.1 to Equation 3.1, the values of $\sqrt{Z_b Z_f}$ for five different configurations of the ultrasonic transducer are listed in Table 3.2. The value of $\sqrt{Z_b Z_f}$ for

CHAPTER 3

the transducer configuration titanium-PZT8-titanium ($31.54 \times 10^6 \text{ kg/m}^2/\text{s}$) is especially close to the acoustic impedance of PZT-8 ($29.9 \times 10^6 \text{ kg/m}^2/\text{s}$), which can reach a good acoustic impedance matching.

Table 3.2 Values of $\sqrt{Z_b Z_f}$ for the different configurations of the ultrasonic transducer

Configuration of ultrasonic transducer	Value of $\sqrt{Z_b Z_f}$
Steel-PZT8-Titanium	35.17×10^6
Steel-PZT8-Duraluminium	23.46×10^6
Titanium-PZT8-Titanium	31.54×10^6
Tool steel-PZT8-Duraluminium	24.14×10^6
Tool steel-PZT8-Titanium	36.18×10^6

The materials of the ultrasonic transducer should also have high fatigue strength to prevent failure of the device, and low internal friction to reduce acoustic loss during ultrasonic wave transmission. The acoustic quality factor is used to evaluate the acoustic performance of a material, and is inversely proportional to the acoustic loss factor. Table 3.3 shows the fatigue strength, acoustic quality factor and acoustic loss factor for the materials considered for the ultrasonic transducer design [92, 138].

Table 3.3 Material properties of the recommended materials for the transducer design

Material	Fatigue strength (MPa)	Acoustic Quality factor	Acoustic loss factor
Titanium alloy Ti-6Al-4V	410	7143	1.4×10^{-4}
Stainless steel (316)	270	2174	4.6×10^{-4}
Duraluminium	225	3333	3.0×10^{-4}
Tool steel	333	2632	3.8×10^{-4}

CHAPTER 3

Stainless steel and tool steel have relatively high fatigue strength but the acoustic loss factor is also high. The high acoustic loss factor increases the heat generation during operation and has a significant negative influence on the efficiency of the acoustic energy transmission. Furthermore, the transducer operating in a high temperature environment also affects the piezoelectric performance of the piezo-ceramic rings. For example, when the temperature of the piezo-ceramic materials reaches its Curie point, the piezoelectric properties will be lost. Duraluminium is easy to manufacture and the cost of duraluminium is quite low, but the disadvantages are also apparent: low fatigue strength and poor performance on material wear. Titanium alloy is an ideal material for an ultrasonic device because of the low acoustic loss and high fatigue strength. In addition, titanium alloy has excellent resistance to wear and corrosion. Consequently, Titanium alloy Ti-6Al-4V is selected as the material for the front mass and back mass because of the acoustic impedance, high fatigue strength and low acoustic loss factor.

3.1.4 Electrode and bolt

The electrode used in the ultrasonic transducer is usually made of copper alloy, which acts as a conductor. The thickness of the electrode has a significant influence on the performance of the ultrasonic transducer. Increasing the thickness of the electrode can enhance the heat dissipation of the transducer because the thicker electrode supplies a more efficient heat sink for the piezo-ceramic rings. However, thicker electrodes decrease the electromechanical coupling factor of the ultrasonic transducer [114]. Consequently, the thickness of the electrode should be selected based on balancing the heat dissipation and the electromechanical coupling factor.

A central bolt is employed to apply a pre-load on the ultrasonic transducer parts (the back mass, electrodes, piezo-ceramic rings and front mass). This is to ensure the parts of the transducer are in compression during operation because the piezo-ceramic rings are weak in tension [122]. Furthermore, the bolt improves the mechanical contact of the transducer parts, which reduces the energy loss between the transducer parts. The pre-stress of the piezo-ceramic rings (Sonox P8) is recommended in the range of 15MPa to 30MPa [122]. When the pre-load is insufficient, the transducer will have the following problems: high impedance, low fatigue life and inconsistent resonant frequency from the design. A bolt made of A2

CHAPTER 3

stainless steel (Westfield Fasteners Ltd., 36mm length) is selected because it has a high tensile strength to prevent failure during the process of applying pre-load.

3.1.5 The mounting position of the high power transducer

The transducer is usually accommodated within a housing for handling and electrical safety reasons. For a high power ultrasonic transducer, the securing component is normally a flange located at the front mass. The flange should be seated at a position where it has the minimum influence on the vibration amplitude because the vibration amplitude is varying along the ultrasonic transducer. The position of the flange is normally selected at the nodal position, where the displacement is nearly equal to 0 [139]. Consequently, it has a minimum influence on the ultrasonic wave transmission.

The nodal plane is located at the centre of the piezo-ceramic rings for a symmetric transducer and it is difficult to attach the flange to the piezo-ceramic rings. The other disadvantage of a symmetric transducer is that the stress at the nodal plane is a maximum, which is one of the reasons for temperature increasing in the piezo-ceramic rings. As mentioned before, the high operating temperature diminishes the piezoelectric performance of the piezo-ceramic rings. To avoid this, the dimensions of the front mass and back mass are carefully adjusted so that the nodal position of the ultrasonic transducer is within the front mass.

3.1.6 Initial consideration of the dimensions of the transducer parts

The dimensions of back mass, front mass and electrodes are determined based on the dimensions of the piezo-ceramic rings. The outer diameter of the back mass, front mass and electrodes should be the same as the outer diameter of the piezo-ceramic rings (20mm). However, the inner diameters of the back mass and front mass should be less than that of the piezo-ceramic rings to create a gap between the bolt and the piezo-ceramic rings. Then an electrical tape is used to cover the bolt to avoid the possibility of an electrical short during operation. The inner diameter of the piezo-ceramic rings is 8.2mm and thus the inner diameters of the back mass and front mass and diameter of the bolt are chosen as 6mm.

CHAPTER 3

The total length of the back mass and piezo-ceramic rings is designed as one quarter wavelength, and the length of the front mass is also equal to one quarter wavelength, as shown in Fig. 3.3. In addition, the length of the back mass and the length of the front mass are tuned by the FE model of the ultrasonic transducer to ensure the nodal plane is not located at the middle position of the two piezo-ceramic rings. The dimensions of the flange and the contact length between the bolt and front mass are also determined by the FE model to avoid undesired flange and bolt vibration modes coupling with the 1st longitudinal vibration mode of the transducer. The dimensions of the transducer parts are initially determined according to the design requirements explained in Section 3.1.

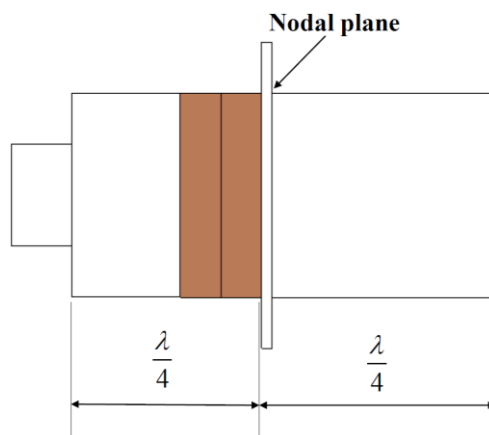


Figure 3.3 The initial dimensions of the ultrasonic transducer

3.2 Finite element analysis

The next step is to determine the dimensions of each transducer part to ensure the assembled transducer operates at the tuned frequency with a pure longitudinal mode. FEA is normally employed for ultrasonic transducer design, which is a numerical method to solve complex structural, thermal and fluid flow problems. It divides a complex system into many small discrete elements that can be analysed by mathematical methods. FEA is widely used in engineering analysis and the advantages of FEA are shown below:

- Enables analysis of complex engineering systems
- Accurately predicts the performance of the engineering system

CHAPTER 3

- Allows evaluation and optimisation of the design, which can reduce the cost of testing and physical prototyping
- Discovers design problems before prototyping
- Shortens the development time of the product

In this work, the commercial FEA software Abaqus/CAE v6.13-1 is utilised to design and analyse the Langevin ultrasonic transducer. The modal parameters of the ultrasonic transducer can be estimated by the FE model created in this software, such as vibration mode and resonant frequency.

3.2.1 Modelling of the ultrasonic transducer in FEA software Abaqus

To predict the modal parameters of the transducer, each part of the transducer is created in Abaqus and the dynamic behaviour is analysed. For an axial symmetric structure, it is possible to study the structure by a two-dimensional (2D) model, to reduce the computational time. Although the ultrasonic transducer is axially symmetric, a three-dimensional (3D) model is created to model the transducer in this work. The reason is that the 1st longitudinal vibration mode of the transducer should have sufficient frequency separation from other modes, and the torsional mode cannot be presented and studied by a 2D model. It normally consists of two main parts to develop the transducer FE model: create the ultrasonic transducer CAD model and discretisation of the transducer simulation model.

Create the ultrasonic transducer CAD model

The transducer parts (front mass, electrodes, piezo-ceramic rings, bolt and back mass) are first created in Abaqus based on the dimensions of each part. The material properties of each part are defined and assigned to the corresponding parts. The required parameters to represent the properties of metal parts are the Young's modulus, Poisson's ratio and material density. These properties are listed in Table 3.4. The mechanical and electrical properties of the piezo-ceramic rings are detailed in Section 3.2.2. Lastly, for a transducer, the boundary conditions are usually classified as the electrical potential and displacement. Applying the electrical potential to the piezo-ceramic rings is not necessary for modal analysis of the transducer. Consequently, the ultrasonic transducer has a free boundary condition.

CHAPTER 3

Discretisation of the transducer simulation model

The mesh is used to discretize a system into small elements that are connected by nodes. The contributions of these elements are calculated individually and assembled together to form the system of equations for the whole problem. The type, shape and density of the elements influences the accuracy of the numerical model. Suitable element parameters are determined by the geometry of the structure, the problem to analyse and the materials of the structure [122]. Abaqus/CAE v6.13-1 provides three different types of element: wedge element, tetrahedral element and hexahedral element. They have two different geometry orders: first order element (use linear interpolation to estimate the solution) and second order element (use quadratic interpolation to estimate the solution). Second order elements are usually selected to conduct the modal analysis for a vibrating system. Previous research has proven that the hexahedral element (C3D20R) is particularly suited to conducting modal analysis for an ultrasonic transducer [92, 122, 135]. The reason is that the hexahedral element can achieve an accurate solution with a lower number of elements compared with the wedge element and tetrahedral element, thus significantly reducing the computational time of the transducer FE model. A mesh convergence study is also performed to determine the appropriate number of elements, which is explained in Section 3.2.3.

Table 3.4 Material properties of the transducer parts used for FE model

Part	Material	Density (kg/m ³)	Young's modulus (GPa)	Poisson's ratio
Back mass	Titanium alloy Ti-6Al-4V	4430	113.8	0.342
Front mass	Titanium alloy Ti-6Al-4V	4430	113.8	0.342
Electrode	Copper C101	8942	115.0	0.31
Bolt	A2 Stainless steel	7850	203.5	0.285

CHAPTER 3

3.2.2 Definition of piezo-ceramic material properties in Abaqus

The piezo-ceramic ring used, PZT-8 (SonoX P8), is an orthotropic material. The mechanical, electrical and electromechanical properties of the PZT-8 piezo-ceramic material are defined by the elastic properties, piezoelectric properties, the electrical permittivity (dielectricity), and the density.

The data used to describe the properties of the piezo-ceramic material in Abaqus is expressed as tensor notation. For example, a fourth order tensor C_{ijkl} is used to represent the elastic properties of the PZT-8. However, the manufacturer usually provides a compressed matrix form to replace the long notation form and the notation p or q are used to replace the ij or kl for simplicity. To import the data provided by the manufacturer into Abaqus, the compressed matrix form is converted to the tensor form according to Table 3.5 [140].

Table 3.5 Conversion of matrix form to tensor form

p or q	ij or kl
1	11
2	22
3	33
4	12
5	13
6	23

The subscripts 1, 2 and 3 represent the direction of x, y and z in a rectangular coordinate system for the piezo-ceramic materials. The shear directions xy, xz and yz are expressed by 4, 5 and 6.

Elastic properties of PZT-8

The elastic modulus of PZT-8 (C_{ij}) is the ratio of the mechanical stress to the strain in the PZT-8 material, which is the reciprocal value of the elastic compliance (s_{ij}) [141]. The first

CHAPTER 3

and second subscripts represent the directions of stress and strain, respectively. The elastic modulus is usually used to evaluate the stiffness and it can be evaluated at a constant electric displacement or a constant electric field. In Abaqus, the elastic modulus evaluated at constant electric field is adopted and expressed as a tensor form D_{ijkl} .

Piezoelectric properties of PZT-8

The piezoelectric properties of PZT-8 are the relationship between the electrical field and the mechanical deformation [122, 141]. Three parameters are usually used to evaluate the piezoelectric properties. The first parameter is named as the piezoelectric charge constant d_{ij} that is the ratio of the mechanical strain to the applied electrical field. The second parameter is also called the piezoelectric charge constant e_{ij} and it relates the stress to the applied electrical field. Therefore, these two parameters are considered in the design of ultrasonic actuators and the evaluation of the piezoelectric performance of the ceramic material. The third parameter named the piezoelectric voltage constant g_{ij} relates the electric field generated to the applied mechanical stress, and is usually used in sensor design.

In Abaqus, the piezoelectric charge constant d_{ij} is used to evaluate the piezoelectric properties of the piezo-ceramic material. The suppliers of the ceramic materials usually provide data for the piezoelectric charge constant d_{ij} (d_{33} , d_{31} and d_{15}), which can be converted into stress form e_{ij} based on the following equation.

$$[e] = [d][D] \quad (3.2)$$

The piezoelectric charge constants (d_{ij} and e_{ij}) are expressed as the following form in Abaqus:

$$[d] = \begin{bmatrix} d_{111} & d_{122} & d_{133} & d_{112} & d_{113} & d_{123} \\ d_{211} & d_{222} & d_{233} & d_{212} & d_{213} & d_{223} \\ d_{311} & d_{322} & d_{333} & d_{312} & d_{313} & d_{323} \end{bmatrix} \quad (3.3)$$

CHAPTER 3

$$[e] = \begin{bmatrix} e_{111} & e_{122} & e_{133} & e_{112} & e_{113} & e_{123} \\ e_{211} & e_{222} & e_{233} & e_{212} & e_{213} & e_{223} \\ e_{311} & e_{322} & e_{333} & e_{312} & e_{313} & e_{323} \end{bmatrix} \quad (3.4)$$

The first subscript represents the direction of the applied electrical field and the last two subscripts are the direction of induced mechanical strain (d_{ijk}) or stress (e_{ijk}). For piezo-ceramic materials poled in the z-direction (thickness direction), Equations 3.3 and 3.4 can be simplified as Equation 3.5 and 3.6.

$$[d] = \begin{bmatrix} 0 & 0 & 0 & 0 & d_{113} & 0 \\ 0 & 0 & 0 & d_{212} & 0 & 0 \\ d_{311} & d_{322} & d_{333} & 0 & 0 & 0 \end{bmatrix} \quad (3.5)$$

$$[e] = \begin{bmatrix} 0 & 0 & 0 & 0 & e_{113} & 0 \\ 0 & 0 & 0 & e_{212} & 0 & 0 \\ e_{311} & e_{322} & e_{333} & 0 & 0 & 0 \end{bmatrix} \quad (3.6)$$

Table 3.5 is employed to convert d_{ij} to d_{ijk} , as below:

$$d_{15} = d_{113}$$

$$d_{212} = d_{113}$$

$$d_{31} = d_{311}$$

$$d_{322} = d_{311}$$

$$d_{33} = d_{333}$$

d_{33} , d_{31} and d_{15} are the data provided by the materials supplier. The matrix of the piezoelectric charge constant $[e]$ is calculated from $[d]$ with Equation 3.2. The piezoelectric charge constant $[d]$ is used in Abaqus to represent the piezoelectric properties of PZT-8.

Permittivity of PZT-8

The permittivity (or dielectric constant) of the piezo-ceramic material defines the dielectric displacement per unit electric field [141]. The permittivity can be evaluated at two conditions: constant stress (ϵ_{ij}^T) or constant strain (ϵ_{ij}^S). In Abaqus, the permittivity at constant strain is adopted to evaluate the permittivity of PZT-8, as shown in Equation 3.7. The first and second subscript of ϵ_{ij}^S represent the direction of the dielectric displacement and the electric field, respectively.

$$[\epsilon^S] = \begin{bmatrix} \epsilon_{11}^S & 0 & 0 \\ 0 & \epsilon_{22}^S & 0 \\ 0 & 0 & \epsilon_{33}^S \end{bmatrix} \quad (3.7)$$

Suppliers usually provide the data for ϵ_{11}^S and ϵ_{33}^S in the condition that the piezo-ceramic material is poled in the thickness direction ($\epsilon_{11}^S = \epsilon_{22}^S$). For the Sonox P8, the relative dielectric constants are supplied, which are the dielectric constants divided by the absolute dielectric constant ϵ_0 ($\epsilon_0 = 8.85 \times 10^{-12}$ farad/meter). Consequently, the dielectric constants of the Sonox P8 can be easily calculated.

Summary of PZT-8 material properties

The elastic modulus D_{ijkl} , the piezoelectric charge constant e_{ijk} and the permittivity at constant strain ϵ_{ij}^S of the PZT-8 are calculated based on the data supplied by the manufacturers [122, 140, 141]. The material properties of PZT-8 used for modelling the ultrasonic transducer in Abaqus are listed in Table 3.6. The data of D_{ijkl} , e_{ijk} and ϵ_{ij}^S , which are not shown in the table, are equal to zero.

CHAPTER 3

Table 3.6 PZT-8 material properties data expressed as the format of Abaqus (elastic properties, piezoelectric properties and electrical permittivity)

Elastic properties of PZT-8 (N/m ²)					
D ₁₁₁₁	D ₁₁₂₂	D ₁₁₃₃	D ₂₂₂₂	D ₂₂₃₃	D ₃₃₃₃
9.54E+10	-7.73E+09	2.58E+10	9.54E+10	2.58E+10	8.59E+10
Piezoelectric properties of PZT-8 (C/N)					
d ₁₁₃	d ₂₁₂	d ₃₁₁	d ₃₂₂	d ₃₃₃	
3.8E-10	3.8E-10	-9.5E-11	-9.5E-11	2.4E-10	
Permittivity of PZT-8 (F/m)					
ε ₁₁ ^S	ε ₂₂ ^S	ε ₃₃ ^S			
7.08E-09	7.08E-09	4.78E-09			

3.2.3 Mesh convergence

In finite element analysis, the number of the elements has an important influence on the accuracy of the solution and the computational time. If fewer elements are used in the FE model, the computational time will be shorter but the solution may be less accurate. On the other hand, increasing the number of elements results in a relatively long computational time. To balance the computing resources and the accuracy of the solution, a mesh convergence study is usually conducted. Mesh convergence is to investigate the minimum number of elements required for a numerical model, which can ensure the solution of the model is not affected by increasing the number of elements.

A mesh convergence study is conducted to study the mesh density affecting the operating frequency of the ultrasonic transducer and surrounding resonant frequencies. The hexahedral element (C3D20R) is adopted to model the ultrasonic transducer as explained in Section 3.2.1. Fig. 3.4 shows the number of elements required to obtain mesh convergence for the ultrasonic transducer on frequencies of the 1st longitudinal mode and two neighbouring vibration modes, the 1st torsional mode and the 2nd bending mode. Table 3.7 shows that the 1st longitudinal and 1st torsional modes converge when the number of elements is 1164. On the other hand, the 2nd bending mode requires more elements (3382 elements) to achieve convergence. To achieve convergence on the 1st longitudinal mode, the 1st torsional mode and the 2nd bending mode, the FE model of the ultrasonic transducer should be over 3382 elements. Moreover, these results also indicate that a finer mesh density is required to achieve convergence for higher order modes. Similar situations have been reported in literature [135, 142].

Table 3.7 The number of elements required to achieve mesh convergence for the vibration modes of the ultrasonic transducer

Vibration mode	Number of elements
1 st torsional mode	1164
1 st longitudinal mode	1164
2 nd bending mode	3382

CHAPTER 3

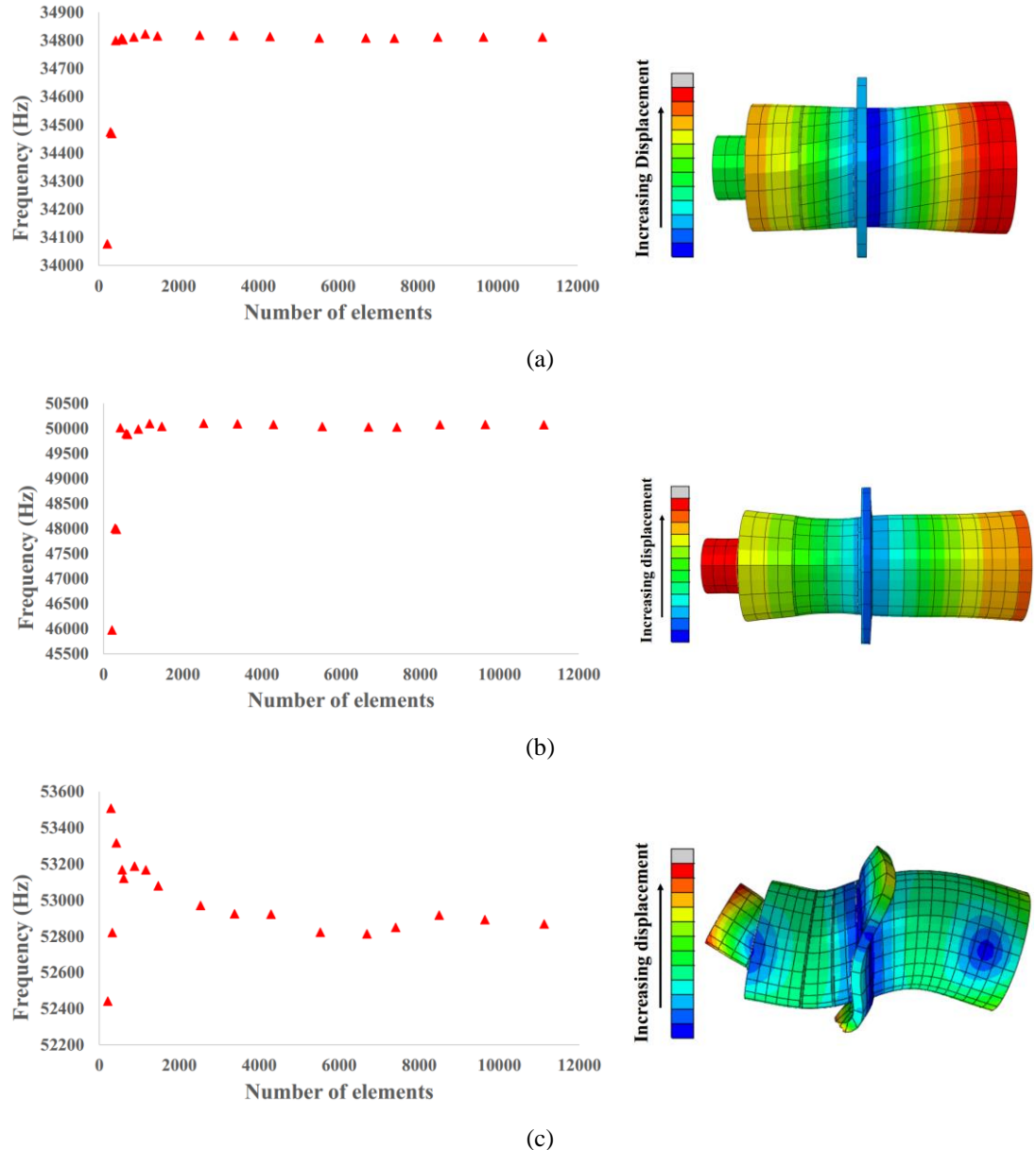


Figure 3.4 Number of elements required to obtain mesh convergence for the operating mode of the ultrasonic transducer and surrounding vibration modes (a) the 1st torsional mode (b) the 1st longitudinal mode (c) the 2nd bending mode

3.3 Dimensions of each ultrasonic transducer part

The initial dimensions of the ultrasonic transducer is achieved based on the design requirements in Section 3.1.6. The dimensions of the piezo-ceramic rings and bolt are also determined. The length of the back mass and front mass have an important influence on the operating frequency of the ultrasonic transducer, which is determined by the FE model. In this section, the dimensions of remaining transducer parts are determined and explained.

3.3.1 The dimensions of the electrode

The outer and inner diameter of the electrode should be the same as the piezo-ceramic ring as explained in Section 3.1.6. The thickness of the electrode is selected to balance the heat dissipation, the electromechanical coupling factor and its life span. The thickness of the copper electrode used for ultrasonic transducer design is usually 0.5mm or even smaller. Two different copper electrodes are used for the transducer, 0.3mm copper C101 sheet and 0.05mm copper alloy CZ106 sheet. It was observed that utilising the 0.05mm copper alloy CZ106 sheet enhanced the electromechanical coupling of the device. However, Fig. 3.5 also shows that the electrodes with 0.05mm thickness are easily damaged.

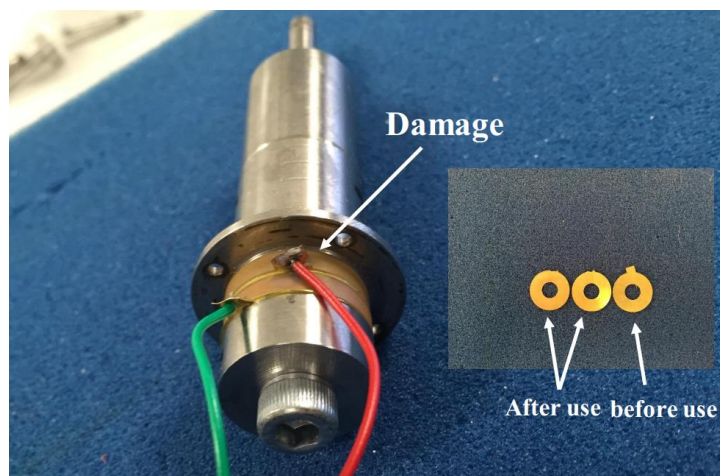


Figure 3.5 The failure of the electrodes (electrodes made of copper alloy CZ106, 0.05mm thickness)

The electrodes were tearing after operating the ultrasonic transducer several times. To give the transducer a longer lifespan, the 0.3mm thickness copper C101 sheet is finally used to

CHAPTER 3

manufacture the electrode. The dimensions of the electrode is: 20mm outer diameter, 8.2mm inner diameter and 0.3mm thickness. The electrode also has an extended rectangular part to be used to solder the electrical wires.

3.3.2 The dimensions of the back mass and front mass

The next step is to determine the length of the back mass and front mass, which has a significant influence on the operating frequency of the transducer. Increasing the length of the back and front mass results in a decrease of the resonant frequency of the transducer's 1st longitudinal vibration mode. The length of the front mass and back mass are determined based on three main requirements as explained below.

1. The frequency of the transducer 1st longitudinal vibration mode is 50kHz.
2. The transducer should be resonant at the operating frequency with a pure longitudinal mode, which means the transducer should have sufficient frequency separation between the operating frequency and the surrounding resonant frequencies. If the operating frequency is close to other resonant frequencies, the vibration amplitude at the transducer tip will be non-uniform due to modal coupling.
3. The position of the flange should have a minimum influence on the ultrasonic wave transmission. This is achieved by adjusting the length of the back mass and front mass to ensure the flange is at the nodal position.

The FE model of the ultrasonic transducer includes a back mass, piezo-ceramic rings, a front mass, electrodes and a bolt. The lengths of the back mass and front mass are tuned by the FE model of the transducer to meet the three main requirements. The back mass length, flange length and front mass length are finally selected as 8.30mm, 1.6mm and 25.4mm, respectively. For this configuration, the resonant frequency of the transducer's 1st longitudinal mode is 50.04kHz, as shown in Fig. 3.6. The difference between the operating frequency predicted by the FE model and the design frequency (50kHz) is 0.076%, which means the first requirement is achieved.

For the transducer tuned at 50.04kHz, there are two surrounding resonant frequencies (in Table 3.8): the resonant frequencies of the 1st torsional mode and the 2nd bending mode. The

CHAPTER 3

difference in frequency is 15.23kHz between the 1st longitudinal mode and the 1st torsional mode and 2.78kHz for the 1st longitudinal mode and 2nd bending mode. The experimental modal analysis (EMA), which can extract resonant frequencies and mode shapes of a vibrating system, will be conducted to study whether these frequency separations are sufficient to avoid the modal coupling. The results of the EMA are presented in Section 4.2.3.

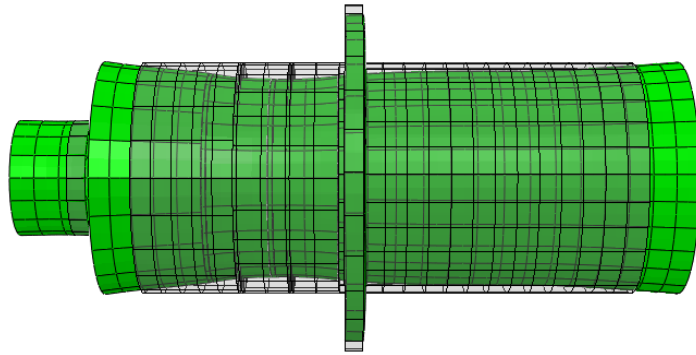


Figure 3.6 Modelled 1st longitudinal mode of the transducer at 50.04kHz (green colour). Note: the black frame structure represents the ultrasonic transducer without deformation.

Table 3.8 The frequencies of the 1st longitudinal mode and neighbouring modes

Vibration mode	Frequency (kHz)
1 st torsional mode	34.81
1 st longitudinal mode	50.04
2 nd bending mode	52.82

The nodal position of the ultrasonic transducer can be seen in Fig. 3.7, which is achieved from the FEA model of the ultrasonic transducer. The nodal position is located at the flange. The displacement along the red solid path on the transducer is presented, which indicates the nodal position is 24.3mm away from the start point of the red solid line. The distance between the flange and the start point of the red solid path is 24.0mm, which means the position of the flange is at the nodal position. Thus, the flange will have a minimum influence on the ultrasonic wave transmission.

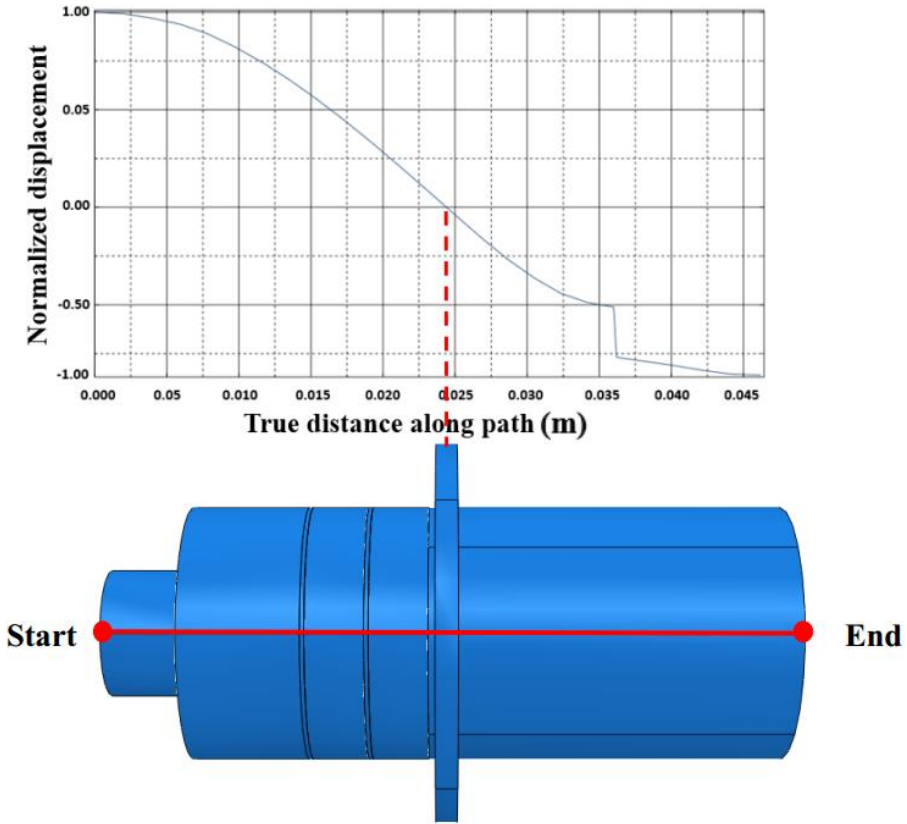


Figure 3.7 The position of the nodal plane and flange

3.4 Design of ultrasonic horn

An ultrasonic horn is a tapering metal bar used to increase the vibration amplitude of an ultrasonic transducer [143]. The ultrasonic horn is necessary to be connected to the ultrasonic transducer because the vibration amplitude of the ultrasonic transducer is small and cannot meet the requirements of the majority of applications. There are four common shapes of ultrasonic horn used in high power ultrasonics: stepped, stepped-exponential, exponential and conical horn [144]. The vibration amplitude gains of the four different ultrasonic horns are different. The stepped horn, which consists of two different sections with uniform cross-section, has the largest gain. However, it also has a high stress concentration at the step. The cross-section of the conical and exponential horns change conically and exponentially with length, respectively. Both of them have relatively low gain.

CHAPTER 3

The momentum of the free mass is achieved from impact with the ultrasonic horn, which is determined by the front mass of the horn tip and the vibration amplitude of the horn tip, as explained in Section 4.11. Thus, the configuration of the ultrasonic horn has a significant influence on the momentum of free mass. To investigate the effect of the horn tip front mass and vibration amplitude on the momentum of the free mass, different configurations of the ultrasonic horn are used. The stepped horn has a large horn tip amplitude but the front mass of the horn tip is small. On the other hand, a large front mass of the horn tip can be achieved by exponential and conical horn while the horn tip amplitude of these two horns are low. Consequently, the effect of stepped, exponential and conical horn on the momentum of the free mass are investigated. Moreover, for the stepped horn, there is a high stress concentration at the step, which may be influence on the final design. The stepped-exponential horn, which is two cylinders connected with an exponential curve, is also used in this study to reduce the high stress concentration. The stepped-exponential horn has the similar properties as the stepped horn: a larger horn tip amplitude than the exponential and conical horn while the front mass of the horn tip is small. It can be used to replace the stepped horn when the high stress concentration of the stepped horn results in device failure. Therefore, the stepped-exponential horn is also used in this study.

To select a suitable ultrasonic horn for the US needle system based on transferring more momentum to the free mass, the method for design of the ultrasonic horn operating at the operating frequency is presented. The four different ultrasonic horns are tuned at 50kHz by two steps: first estimate the resonant length of different shaped ultrasonic horns using the analytical method; then tune the ultrasonic horn length in Abaqus based on the analytical resonant length to ensure the ultrasonic horn reaches the design frequency.

3.4.1 Design of different shapes of ultrasonic horn by analytical method

The equations, which are used to calculate the length of different resonant ultrasonic horns, are different and determined by the geometry of the horn. Equation 3.8 describes a longitudinal, plane wave propagating in a bar with variable cross-section [145].

CHAPTER 3

$$\frac{d^2A}{dx^2} + \frac{d \ln S(x)}{dx} \frac{dA}{dx} = \frac{1}{c^2} \frac{d^2A}{dt^2} \quad (3.8)$$

Where A is the amplitude of vibration in the axial direction, $S(x)$ is the cross-sectional area at x that is the distance from its origin as shown in Fig. 3.8, and c is the speed of the stress wave propagating in the bar. The resonant length and magnification factor of stepped, exponential and conical horn can be calculated by substituting the corresponding cross-sectional area function $S(x)$ into the wave equation 3.8.

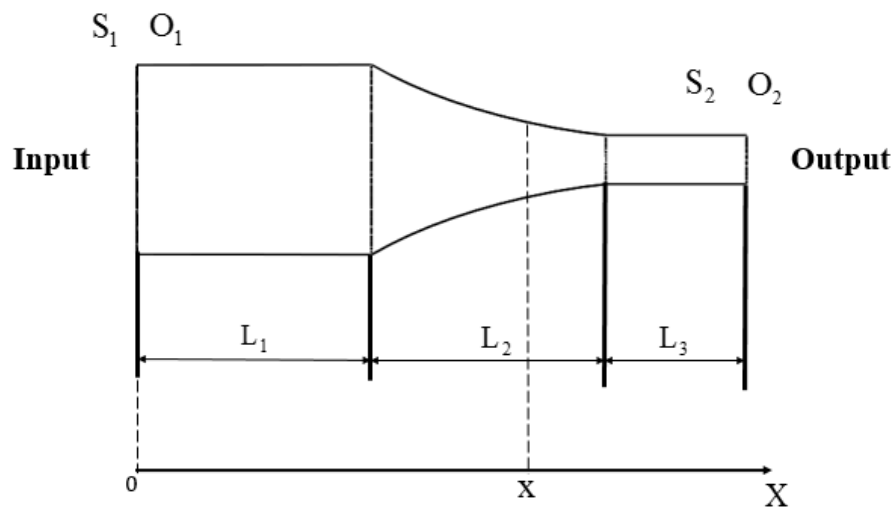


Figure 3.8 The shape of stepped-exponential horn

The shape of the stepped-exponential horn is shown in Fig. 3.8 [146]. The stepped-exponential horn has three sections: two cylinders connected by an exponential curve. The length of the first part L_1 is equal to a quarter of one wavelength. The length of L_2 , L_3 and vibration amplitude gain G can be calculated from the Fig. 3.9 [146].

CHAPTER 3

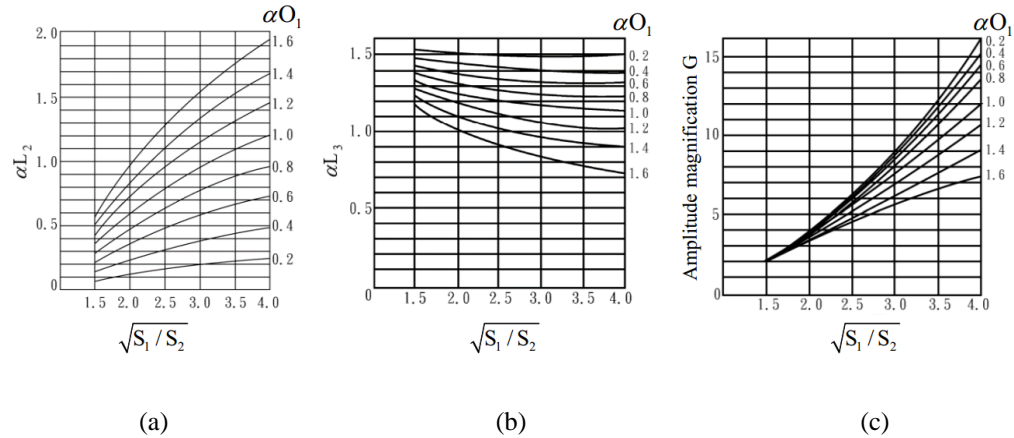


Figure 3.9 Calculation of the length of L_2 , L_3 and vibration amplitude gain (a) L_2 length (b) L_3 length (c) the vibration amplitude gain of stepped-exponential horn [146]

Where:

O_1 : the diameter of the input end

O_2 : the diameter of the output end

S_1 : the area of the input end

S_2 : the area of the output end

ω : the angular frequency of vibration

f : the design frequency

c : is the speed of the stress wave propagating in the material

α : $(\frac{\omega}{c})$, the angular frequency of vibration divided by the wave speed

The formulae, which are used to calculate the length and vibration amplitude gain of different shapes of horn vibrating at a specific frequency, are presented in Table 3.9.

CHAPTER 3

Table 3.9 Formulae for calculating the resonant length and vibration amplitude gain of different horns
[143,145]

Horn shape	Ultrasonic horn	Resonant length of a half-wavelength horn, L	Vibration amplitude gain
Cylindrical horn		$\frac{c}{2f}$	1
Stepped horn		$\frac{c}{2f}$	$\left(\frac{O_1}{O_2}\right)^2$
Stepped-exponential horn		$L_1 = \frac{\lambda}{4}$ L_2 and L_3 are shown in Fig. 3.9(a) and 3.9(b), respectively.	Shown in Fig. 3.9(c).
Exponential horn		$\frac{c}{2f} \sqrt{1 + \left(\frac{\ln(O_1/O_2)}{\pi}\right)^2}$	O_1/O_2
conical horn		$\tan \frac{\omega L}{c} = \frac{\omega c L (O_1 - O_2)^2}{c^2 (O_1 - O_2)^2 + \omega^2 L^2 O_1 O_2}$	$\frac{O_1}{O_2} \cos \frac{\omega L}{c} - \frac{c(O_1 - O_2)}{\omega L O_2} \sin \frac{\omega L}{c}$

CHAPTER 3

The four different ultrasonic horns (stepped, stepped-exponential, exponential and conical horn) are designed to resonate at 50kHz. The base diameter and tip diameter of the horns are kept constant, with a base diameter of 20mm. In this section, the tip diameter is selected as 5mm, which is used to compare the resonant length achieved by the analytical method and FEA method. Moreover, the momentum of the free mass effected by different horn tip diameters (between 3mm to 15mm) are investigated in Chapter 4. The dimensions and vibration amplitude gain of the stepped, exponential and conical horn can be easily calculated from the formulae in Table 3.9. However, it is relatively difficult to determine the dimensions of the stepped-exponential horn. The process of calculating the dimensions of the stepped-exponential horn is shown below. The material of the stepped-exponential horn is titanium alloy Ti-6Al-4V.

$$L_1 = \frac{\lambda}{4} = \frac{c}{4f} = \frac{5027}{4 \times 50} = 25.14\text{mm} \quad (3.9)$$

The areas of input and output ends are:

$$S_1 = \left(\frac{O_1}{2} \right)^2 \pi \quad (3.10)$$

$$S_2 = \left(\frac{O_2}{2} \right)^2 \pi \quad (3.11)$$

αL_2 and αL_3 can be calculated from Fig. 3.9(a) and 3.9(b) based on the value of $\sqrt{S_1/S_2}$ and αO_1 .

$$\sqrt{\frac{S_1}{S_2}} = \sqrt{\frac{O_1^2}{O_2^2}} = \frac{O_1}{O_2} = 4 \quad (3.12)$$

$$\alpha = \frac{\omega}{c} = \frac{2\pi f}{c} = 62.5 \quad (3.13)$$

CHAPTER 3

$$\alpha O_1 = \frac{\omega}{c} O_1 = 62.50 \times 02 = 1.25 \quad (3.14)$$

$$\alpha L_2 = 1.52 \quad (3.15)$$

$$\alpha L_3 = 0.94 \quad (3.16)$$

L_2 and L_3 are determined, which are 24.32mm and 15.04mm, respectively. Consequently, the total length of the stepped-exponential horn is shown below.

$$L = L_1 + L_2 + L_3 = 64.46\text{mm} \quad (3.17)$$

The profile of the stepped-exponential horn middle part is an exponential section and it is necessary to determine the coordinates of this part to plot the exponential curve (Fig. 3.10). The radius of the exponential part along the decay section is presented below:

$$r_x = r_i e^{-\beta x} \quad (3.18)$$

$$\beta = \frac{\ln \frac{r_1}{r_2}}{L_2} = \frac{1}{24.32} \ln 4 = 0.057 \quad (3.19)$$

Where r_i and r_2 are the radius of the input and output end, respectively. β is the exponential decay coefficient.

$$r_x = 10 e^{-0.057 x} \quad (3.20)$$

Using Equation 3.20, the data used to plot the exponential curve can be calculated and are shown in Table 3.10.

CHAPTER 3

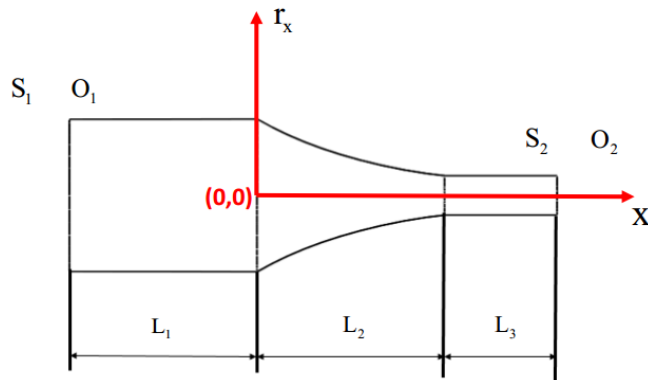


Figure 3.10 The coordinate of the exponential part

Table 3.10 Data used to plot the exponential curve

x (mm)	r_x (mm)
0	10
5	7.50
10	5.66
15	4.25
20	3.20

The resonant length and vibration amplitude gain of the four different horns resonating at 50kHz are calculated by the analytical method based on Table 3.9, which are shown in Table 3.11.

Table 3.11 The resonant length and vibration amplitude gain of the four different horns

Horn shape	Resonant length (mm)	Vibration amplitude gain
Stepped horn	50.27	16
Stepped-exponential horn	64.46	10.2
Exponential horn	55.04	4
Conical horn	60.44	3.82

3.4.2 Design of different shapes of ultrasonic horn by FEA method

The stepped, stepped-exponential, exponential and conical horn are also designed to resonate at 50kHz using the FEA method. The FEA software Abaqus is adopted to extract the modal frequencies and mode shapes of different shapes of horn. The base diameter and the tip diameter of these horns are the same as the horns used in analytical method, which are 20mm and 5mm, respectively. The dimensions of these horns are tuned by the FE models to ensure the 1st longitudinal vibration mode is 50kHz. Fig. 3.11 shows the mode shapes of these horns extracted from the FE models.

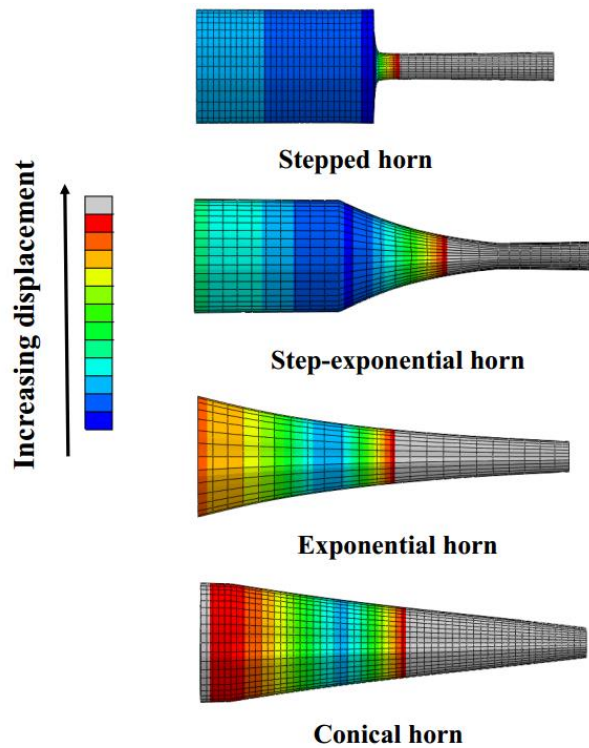


Figure 3.11 Mode shapes of the stepped, conical, exponential and stepped-exponential horn (1st longitudinal vibration mode)

Table 3.12 shows that the length and vibration gain of the half-wavelength horns resonating at 50kHz as calculated by the analytical and FEA method. It is observed that the resonant length and vibration gain achieved by the analytical and FEA method have a good agreement. The difference of the horn length calculated by the two methods is less than 1mm (1%) for the stepped horn, stepped-exponential horn and exponential horn, and 2.64mm (4.4%) for

CHAPTER 3

the conical horn. Consequently, both of the methods are suitable for ultrasonic horn design. Compared to the analytical method, the FEA method has many advantages. For example, the stress distribution along the horn can be accurately determined. Thus, the maximum stress value in the horn can be controlled under the fatigue limit of the alloy, preventing failure of the whole device. FEA can also determine the displacement of the horn. This means the nodal position can be tuned to a desired position by the FE model. However, the analytical method is still important in providing an initial dimensions of a horn. These initial dimensions are a reference for the FEA method and used in the FE model to conduct ultrasonic horn design.

Table 3.12 The resonant length and vibration amplitude gain of four different horn shapes tuned nearly at 50kHz by the analytical method and FEA method (5mm horn tip diameter)

	Calculated horn length (mm)		Vibration gain		Frequency (kHz)
	Analytical	FEA	Analytical	FEA	
Stepped horn	50.27	49.70	16.00	13.70	49.98
Stepped-exponential horn	64.46	64.62	10.20	8.95	50.00
Exponential horn	55.04	54.94	4.00	3.90	49.92
Conical horn	60.44	57.80	3.82	3.43	49.98

3.5 Chapter conclusion

The method of the ultrasonic transducer and horn design has been investigated in this chapter. The characteristic parameters of the Langevin ultrasonic transducer were determined according to the application on surgical drilling: a half-wavelength transducer resonating at 50kHz for 1st longitudinal vibration mode. The material of each transducer part was also discussed and selected to obtain the largest acoustic energy transmission and high electromechanical coupling. To ensure the transducer was resonating at the design frequency

CHAPTER 3

with a pure longitudinal motion, the dimensions of the transducer were optimised by the FEA software Abaqus, which can extract the resonant frequencies and vibration modes.

Four different shapes of ultrasonic horn (stepped, stepped-exponential, exponential and conical horn) were designed to resonate at 50kHz by the analytical and FEA method. The resonant length and vibration gain of the four horn shapes achieved by the analytical and FEA method had a good agreement. This indicates both of the methods are suitable for the ultrasonic horn design. However, compared with the analytical method, the FEA method can easily calculate the stress and displacement along the horn to prevent device failure and select a suitable position to mount the flange. The method of ultrasonic horn design was used to select a suitable configuration of a horn to transfer maximum momentum to the free mass for each impact, which is presented in Chapter 4.

Chapter 4 Optimisation of the ultrasonic horn and design of the ultrasonic-sonic needle system

The components of the US needle system should be optimised to achieve the maximum effective impulse delivered to the target and a desired needle penetration performance. For the US needle, the ultrasonic horn impacts the free mass and the free mass receives the momentum from the horn. Then, the free mass moves forward to hit the needle and transfers an impulse to the needle. The needle delivers considerable force to the target in a short time period for each impact. The effective impulse increases when the ultrasonic horn transfers more momentum to the free mass. Therefore, to maximise the effective impulse delivered to the target, optimisation of the ultrasonic horn was studied in this chapter. Different shapes of ultrasonic horns were first investigated. A numerical model of the ultrasonic horn impacting the free mass, was developed to select the suitable horn for the US needle. The shape and dimensions of the ultrasonic horn were determined through the numerical model, which focuses on maximising the post-collision velocity of the free mass. Then, the FE model of the ultrasonic transducer-horn was developed by assembly of the ultrasonic horn model and the ultrasonic transducer model. It was used to investigate the dynamic behaviour of the ultrasonic transducer-horn. The ultrasonic transducer-horn was manufactured and assembled to form a one wavelength ultrasonic surgical device. The fabricated transducer-horn was characterised by two methods, electrical impedance analysis and experimental modal analysis (EMA). The electrical properties of the transducer-horn were evaluated by the electrical impedance analysis. EMA was used to confirm the ultrasonic transducer-horn vibrating at the design frequency with a pure longitudinal mode and it also validated the FE model.

The US needle and corresponding experimental rigs were also designed and presented in this chapter. The components of the US needle were also investigated, such as free mass and needle.

4.1 Optimisation of the ultrasonic horn

Stepped, stepped-exponential, exponential and conical horn are used in this study to investigate the influence on the momentum of the free mass, as explained in Section 3.4. The ultrasonic horn is optimised by considering two features: the shape and the tip diameter.

4.1.1 Determination of the shape of the ultrasonic horn

The momentum of the free mass achieved from impact with the ultrasonic horn depends on two factors: the vibration amplitude of the horn tip and the effective mass of the ultrasonic horn. The most suitable horn is selected based on these two factors. The effective mass of the horn is the part of the horn tip that influences the dynamic behaviour of the free mass during impact. Consequently, the length of the effective mass is defined by the distance travelled by the wave propagating in the material during an impact event [57]. The vibration amplitude gains of the four different horns can be calculated from Table 3.9, and hence the vibration amplitude of the horn tip can be calculated when the vibration amplitude of the horn base is given. However, it is difficult to directly calculate the effective mass; therefore, the momentum of the free mass achieved from the four horn shapes is not evaluated by an analytical method.

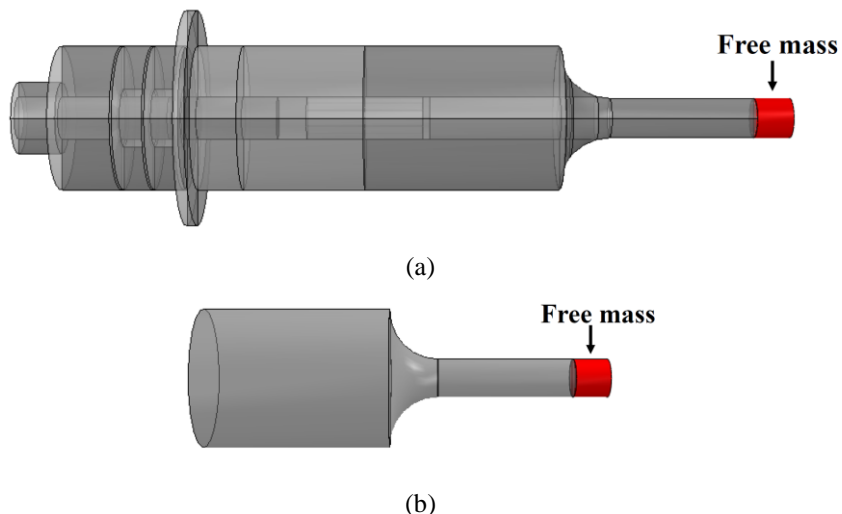


Figure 4.1 FE model used to calculate the post-velocity of the free mass (a) the ultrasonic transducer-horn impacting the free mass (b) the ultrasonic horn impacting the free mass

CHAPTER 4

To select the suitable horn, the four different shaped ultrasonic horns (stepped horn, stepped-exponential horn, exponential horn and conical horn) impacting the same free mass were modelled in the FEA package Abaqus. The free mass was placed before the horn tip. The best configuration of the horn shape for the US needle was determined based on the velocity of the free mass after collision. Because the same free mass was used in the FE models, the momentum of the free mass was only determined by the velocity of the free mass after collision. Two numerical models can be used, as shown in Fig. 4.1. One is the assembled ultrasonic transducer-horn impacting the free mass: an AC voltage at a frequency of 50kHz is used to drive the ultrasonic transducer-horn that retreats first and then advances to impact the free mass. The other numerical model is the ultrasonic horn impacting the free mass: the ultrasonic horn is driven by a sinusoidal displacement at a frequency of 50kHz at the base of the ultrasonic horn. Both of the FE models can be used to evaluate the post-collision velocity of the free mass. However, for the ultrasonic transducer-horn impacting the free mass model, computing resources will be much larger than the ultrasonic horn impacting the free mass model because the ultrasonic transducer is involved into the calculation and it takes a large portion of computational time. Consequently, the FE model of the ultrasonic horn impacting the free mass is selected to evaluate the performance of the ultrasonic horns.

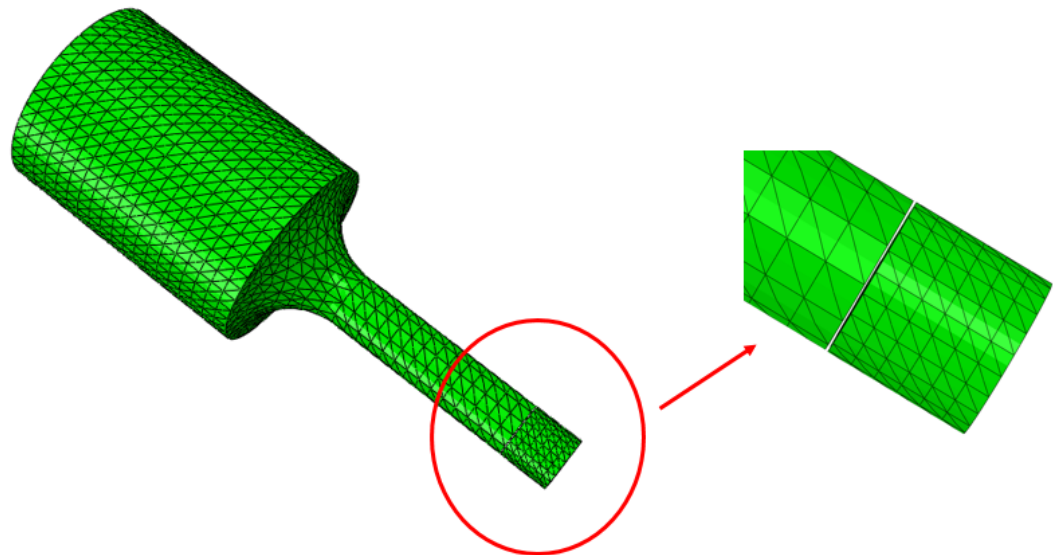


Figure 4.2 FE model of ultrasonic horn impacting the free mass: stage of after impact

CHAPTER 4

The ultrasonic horn impacting the free mass model are shown in Fig. 4.2. The ultrasonic horn and free mass were simulated as a homogeneous 3D deformable solid in Abaqus. The tetrahedron element (C3D10M) was applied to the ultrasonic horn and free mass. It is a second order element as described in Section 3.2.1 and is suitable for modelling contact problems [140, 147]. Titanium alloy Ti-6Al-4V was selected as the material of the ultrasonic horn and free mass, and the ultrasonic horn was tuned at 50kHz in the 1st longitudinal vibration mode. The boundary condition was a sinusoidal displacement at 50kHz applied to the base of the horn, which could drive the horn tip to retreat first and then advance to hit the free mass. The free mass was kept at the original position with zero velocity before the impact occurred. The velocity of the free mass after collision was extracted from the FE model to evaluate the performance of the horn.

To calculate the post-collision velocity of the free mass, the stepped, stepped-exponential, exponential and conical horns were first tuned at the same frequency of approximately 50kHz. The base diameter of these horns is equal to the diameter of the ultrasonic transducer, 20mm. The vibration amplitude gain of a horn is determined from the base and tip diameters, where a smaller tip delivers a larger gain and therefore higher amplitude, but the effective mass is low and hence momentum is not maximised. To investigate the vibration amplitude and the effective mass of the different horns affecting the momentum of the free mass, tip diameters of 5mm, 8mm and 10mm were considered. Table 3.12, 4.1 and 4.2 show the resonant length and vibration amplitude gain of the four shapes of horn.

CHAPTER 4

Table 4.1 The resonant length and vibration amplitude gain of four different horn shapes tuned nearly at 50kHz by the analytical and FEA method (8mm horn tip diameter)

	Calculated horn length (mm)		Vibration gain		Frequency (kHz)
	Analytical	FEA	Analytical	FEA	
Stepped horn	50.27	49.10	6.25	5.82	49.95
Stepped-exponential horn	58.13	57.73	4.90	4.68	50.02
Exponential horn	52.36	52.10	2.50	2.46	49.97
Conical horn	57.60	53.75	2.46	2.33	50.07

Table 4.2 The resonant length and vibration amplitude gain of four different horn shapes tuned nearly at 50kHz by the analytical and FEA method (10mm horn tip diameter)

	Calculated horn length (mm)		Vibration gain		Frequency (kHz)
	Analytical	FEA	Analytical	FEA	
Stepped horn	50.27	49.00	4.00	3.76	49.95
Stepped-exponential horn	56.02	54.93	3.50	3.33	50.01
Exponential horn	51.50	51.13	2.00	1.99	49.95
Conical horn	56.65	52.25	1.98	1.95	49.94

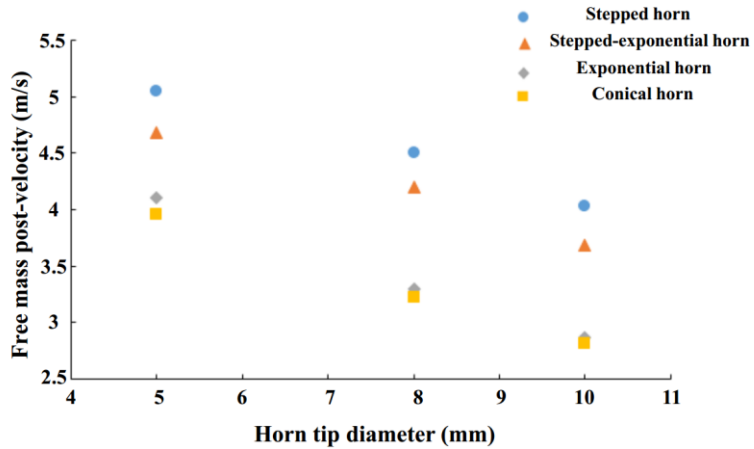


Figure 4.3 The velocity of the free mass after a single collision by the four different shaped horns

The four different horns with the diameters of 5mm, 8mm and 10mm impacting the same free mass were modelled in Abaqus. The same vibration amplitude was applied to the base of the ultrasonic horns. Fig. 4.3 shows that the free mass obtains the largest velocity from the stepped horn, which means the stepped horn can impart the largest momentum to the free mass. The stepped horn was selected for the US needle.

4.1.2 Determination of the tip diameter of the stepped horn

The vibration gain is determined from the ratio of the base diameter and tip diameter of the horn. Although a large diameter ratio leads to a high gain horn, a small tip diameter can detrimentally affect the effective mass of the horn and can also induce elevated stresses in the horn. To determine the tip diameter of the stepped horn that transfers the largest momentum to the free mass and ensures the maximum stress in the horn is within an acceptable range, stepped horns with a range of tip diameters (from 3mm to 15mm) were modelled impacting the same free mass in Abaqus. The post-collision velocity of the free mass and the maximum stress in the horn are shown in Fig. 4.4. The largest velocity of the free mass is predicted for the stepped horn with the maximum diameter ratio. However, the maximum stress of this horn is 637MPa, which is significantly larger than the fatigue limit of the titanium alloy Ti-6Al-4V (410MPa) [148]. The free mass velocities are similar when the diameter ratio is between 3.33 (6mm horn tip diameter) and 4 (5mm horn tip diameter). The maximum stress of the horn with 5.5mm tip diameter (300MPa) is lower than the horn

of 5mm tip diameter (353MPa). And it is less than the fatigue limit of the titanium alloy, 410MPa. A safety factor of 1.3 was recommended to ensure the ultrasonic horn without the risk of failure during operation [58, 149]. Therefore, the stepped horn with 5.5mm tip diameter is selected and manufactured for the US needle. Moreover, the results in Section 4.1.1 and 4.1.2 indicate that the vibration amplitude of the ultrasonic horn has a more important influence on the momentum of the free mass than the effective mass.

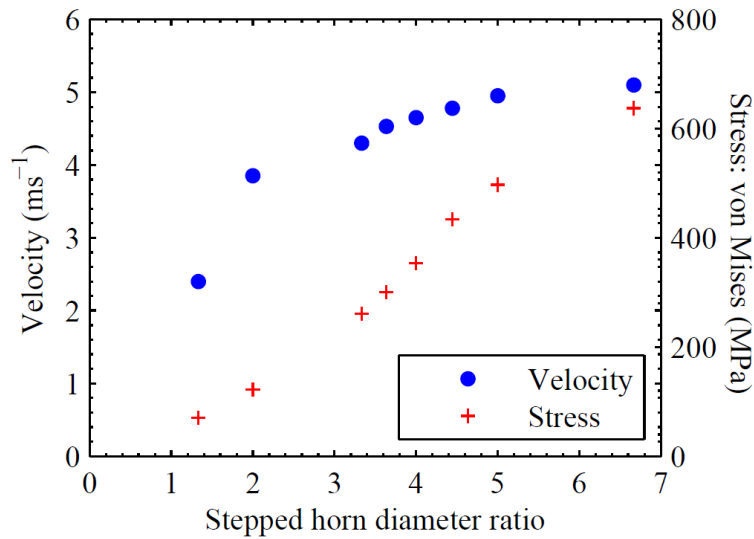


Figure 4.4 The velocity of the free mass after single collision and the maximum stress in the horns, predicted by FEA

4.1.3 FE model of the ultrasonic transducer-horn

The stepped horn with 5.5mm tip diameter and the ultrasonic transducer were assembled and modelled in FEA software Abaqus. A mesh convergence study was conducted to investigate the effect of mesh density on the tuned frequency of the ultrasonic transducer and surrounding resonant frequencies. The results of the mesh convergence are shown in Fig. 4.5 and Table 4.3.

CHAPTER 4

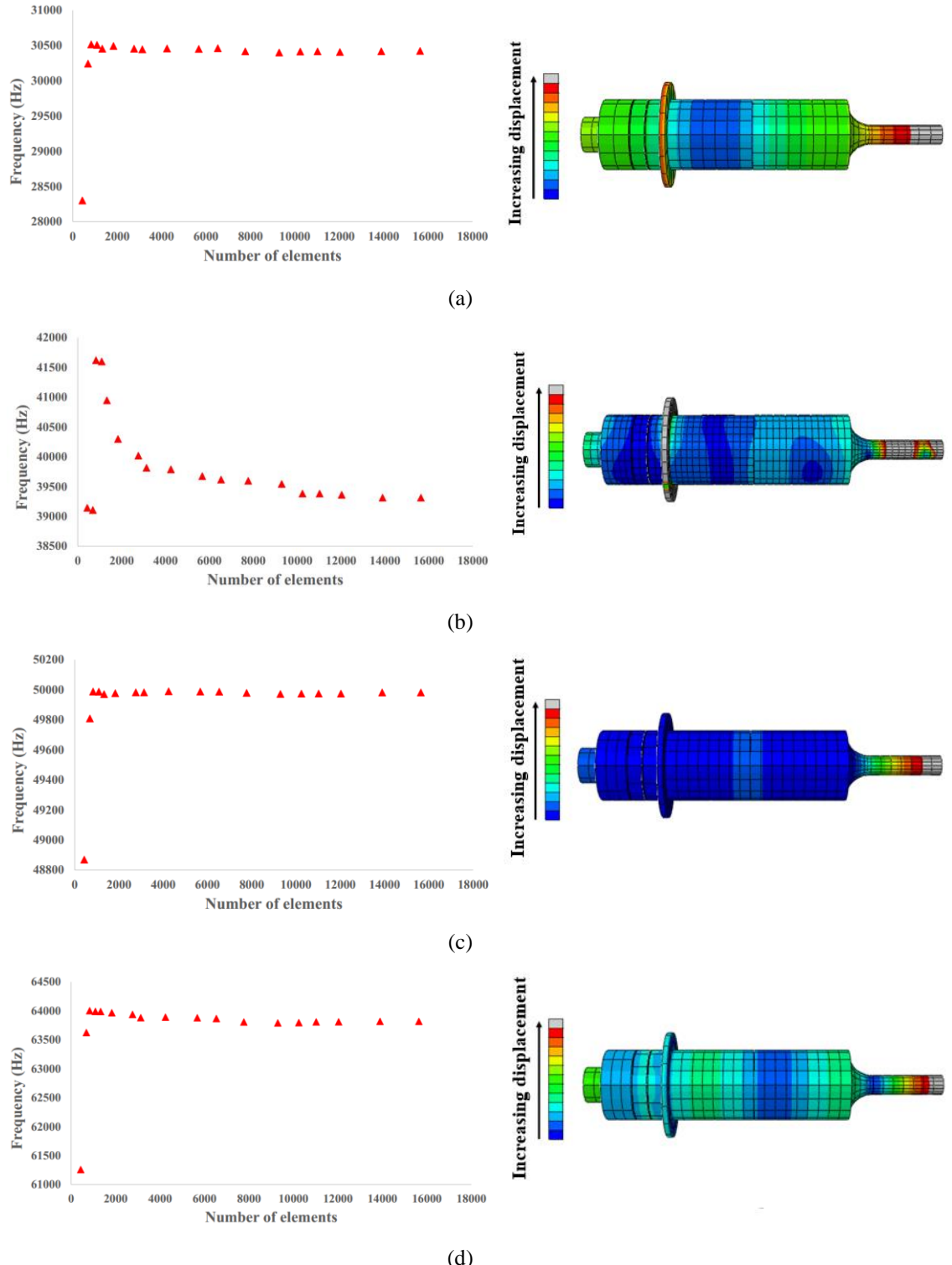


Figure 4.5 Mesh convergence study of the ultrasonic transducer-horn (a) 1st longitudinal mode (b) 4th bending mode (c) 2nd longitudinal mode (d) 3rd longitudinal mode

CHAPTER 4

Table 4.3 The number of elements required to achieve mesh convergence for the vibration modes of the transducer-horn

Vibration mode	Number of elements
1 st longitudinal mode	1328
4 th bending mode	5673
2 nd longitudinal mode	1832
3 rd longitudinal mode	1832

Table 4.3 shows the number of elements required to achieve mesh convergence for the ultrasonic transducer-horn on frequencies of the 2nd longitudinal mode and two neighbouring vibration modes, the 4th bending mode and the 3rd longitudinal mode. 1328 elements are required to obtain the mesh convergence for the 1st longitudinal mode that is also a surrounding mode of the 2nd longitudinal mode. To obtain convergence on this four vibration modes, the number of elements for the FE model of the transducer-horn should be more than 5673. Table 4.4 shows the resonant frequencies of the tuned mode and three surrounding vibration modes when the FE model of the ultrasonic transducer-horn is assigned 5673 elements. The differences in frequencies are 19.54kHz between the 2nd longitudinal mode and the 1st longitudinal mode, 10.31kHz between the 2nd longitudinal mode and the 4th bending mode, and 13.89kHz between the 2nd longitudinal mode and the 3rd longitudinal mode. The EMA (in Section 4.2.3) will be used to validate the FE model of the transducer-horn and study whether the frequency differences between the tuned frequency and neighbouring frequencies are sufficient to avoid modal coupling.

Table 4.4 The frequencies of the 2nd longitudinal mode and surrounding vibration modes

Vibration mode	Frequency (kHz)
1 st longitudinal mode	30.45
4 th bending mode	39.68
2 nd longitudinal mode	49.99
3 rd longitudinal mode	63.88

4.2 Experimental analysis of the ultrasonic transducer-horn

The components of the ultrasonic transducer-horn are manufactured and assembled. To characterise the ultrasonic transducer-horn, electrical impedance analysis and EMA are conducted in this study. Electrical impedance analysis is employed to analyse the electrical properties of the transducer-horn and calculate the resonant frequency, the anti-resonant frequency and the effective electromechanical coupling coefficient. EMA is used to extract the modal parameters of the ultrasonic transducer-horn, resonant frequencies and mode shapes.

4.2.1 Assembly of the ultrasonic transducer-horn and electrical impedance analysis

The parts of the ultrasonic transducer (back mass, bolt, piezo-ceramic rings, electrode rings and front mass,) are shown in Fig. 4.6, which are first assembled. It is necessary to have a good mechanical contact between the transducer parts to achieve high acoustic energy transmission and low mechanical loss. Each part of the transducer requires cleaning with acetone to remove any dirt or grease on the surface. The bolt exposed to the inner piezo-ceramic rings is covered with an electrical tape to avoid the possibility of a short circuit.

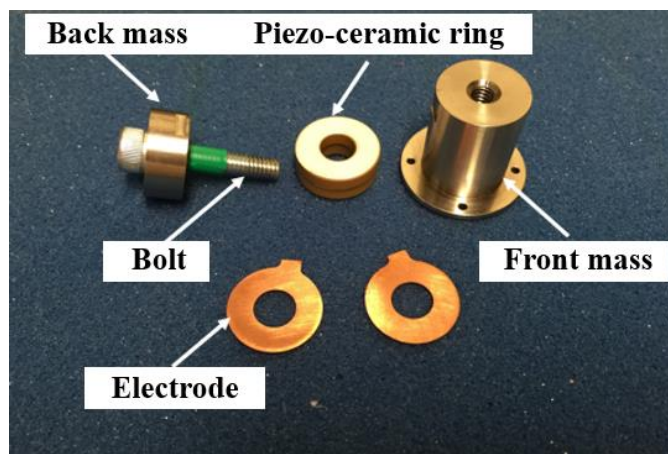


Figure 4.6 The parts of the ultrasonic transducer

CHAPTER 4

The pre-load plays an important role in the assembly of the ultrasonic transducer, which is used to keep all of the transducer parts in compression, especially the piezo-ceramic rings. Insufficient pre-load results in higher impedance, while excessive pre-load can cause the depolarisation of the piezo-ceramic rings, bolt failure and unstable impedance. It is suggested that the pre-stress values of the piezo-ceramic materials normally range from 15MPa to 30MPa [122, 135]. To apply the pre-load, the transducer is fixed in a vice, as shown in Fig. 4.7.

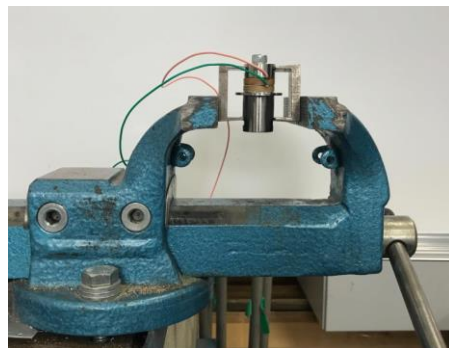


Figure 4.7 Assembly of the ultrasonic transducer

In this work, a torque wrench (Norbar TT20, 1Nm-20Nm) was used to apply the pre-load to the transducer in five steps, as shown in Table 4.5. The impedance spectrum of the transducer was measured under each pre-load to evaluate the transducer performance. An Agilent 4294A impedance analyser was used to measure the impedance spectrum in the frequency range between 10kHz to 80kHz. The electrical impedance measurements are used to obtain the magnitude of electrical impedance of the transducer in the selected frequency range, and the series resonant frequency f_s and parallel resonant frequency f_p can be measured. The input electrical signal of the measurement is small and thus it can be assumed that the values of the series and parallel resonant frequencies, f_s and f_p , are equal to the resonant and anti-resonant frequencies, f_r and f_a , respectively [122, 135]. Moreover, the frequencies f_m and f_n , which are at the maximum and minimum electrical admittance, are also approximately equal to f_s and f_p . This indicates $f_r \approx f_s \approx f_m$ and $f_a \approx f_p \approx f_n$. Table 4.5 also shows the resonant and anti-resonant frequency of the transducer after each step of applying the pre-load.

CHAPTER 4

Table 4.5 Parameters of the ultrasonic transducer after each step of applying the pre-load

Steps	Torque applied to the bolt (Nm) / Stress applied to the piezo-ceramic rings (MPa)	Resonant frequency (kHz)	Increasing value of the resonant frequency (kHz)	Anti-resonant frequency (kHz)	Effective electromechanical coupling coefficient, k_{eff}
1	3 / 9.9	44.90	N/A	47.89	0.348
2	5 / 16.5	45.63	0.73	49.21	0.374
3	6.5 / 21.45	46.09	0.46	49.86	0.381
4	8 / 26.4	46.21	0.12	50.22	0.392
5	9.5 / 31.35	46.29	0.08	50.45	0.397

The frequency changes in Table 4.5 indicate electrical stability of the transducer is reached at step 5 [122, 135]. The effective electromechanical coupling coefficient, k_{eff} , is also calculated for the five pre-load steps using Equation 4.1. k_{eff} is used to evaluate the electromechanical coupling strength, and a high value of k_{eff} is preferred for ultrasound transducers. A large effective electromechanical coupling coefficient and stable resonant frequency are achieved when a 9.5Nm torque is applied to the transducer, resulting in a stress in the piezo-ceramic rings of 31.35MPa.

$$k_{\text{eff}}^2 = 1 - \frac{f_r^2}{f_a^2} \quad (4.1)$$

CHAPTER 4



Figure 4.8 The assembled ultrasonic transducer-horn

The assembled ultrasonic transducer is then connected to the stepped horn by a threaded joint with 12mm length. The ultrasonic transducer-horn is shown in Fig. 4.8. The electrical impedance analysis of the transducer-horn is shown in Fig. 4.9, indicating the resonant frequency is 50.73kHz. This is close to the design frequency of the ultrasonic transducer-horn. The resonant frequency of the transducer-horn (2nd longitudinal mode) extracted from the FE model is 49.99kHz, representing a 1.46% difference with the electrical impedance measurement.

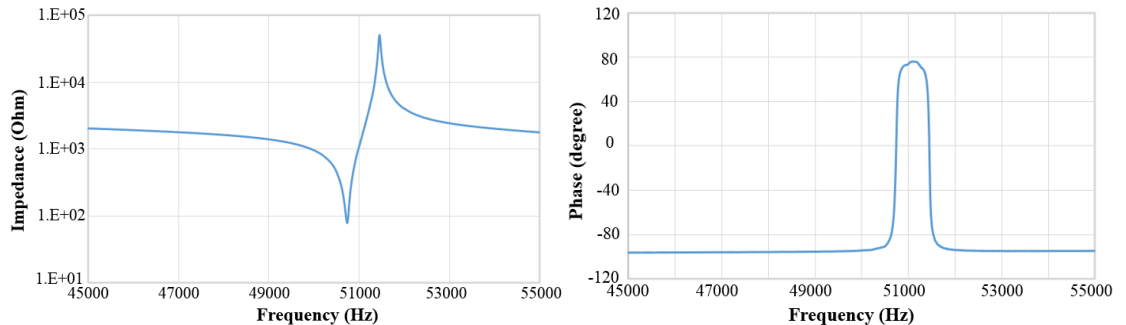


Figure 4.9 Electrical impedance analysis of the ultrasonic transducer and horn

4.2.2 Experimental modal analysis

EMA is a process to identify the modal parameters of a vibrating structure, i.e. natural frequency, mode shape and damping factor. It is widely used in vibration control and vibration-based structural health monitoring [150-152]. The most common application of EMA is to measure the vibration properties of a structure to compare with a FE model or a theoretical model of the structure. A real structure is a continuous system with infinite

CHAPTER 4

degree-of-freedom (DoF). The real structure is analysed using the EMA by discretisation of the structure, which indicates a finite number of DoF is considered and used to estimate the modal parameters of the structure. For ultrasonic transducer-horn design, EMA is normally combined with FEA to allow for a more efficient and accurate design process. FE models are first used to estimate the natural frequencies and mode shapes of a transducer-horn at the design stage. Then, EMA is used to accurately measure the modal parameters of the transducer-horn, which are used to validate the FE models. In this work, the assembled ultrasonic transducer-horn is analysed using EMA to extract the resonant frequencies and mode shapes.

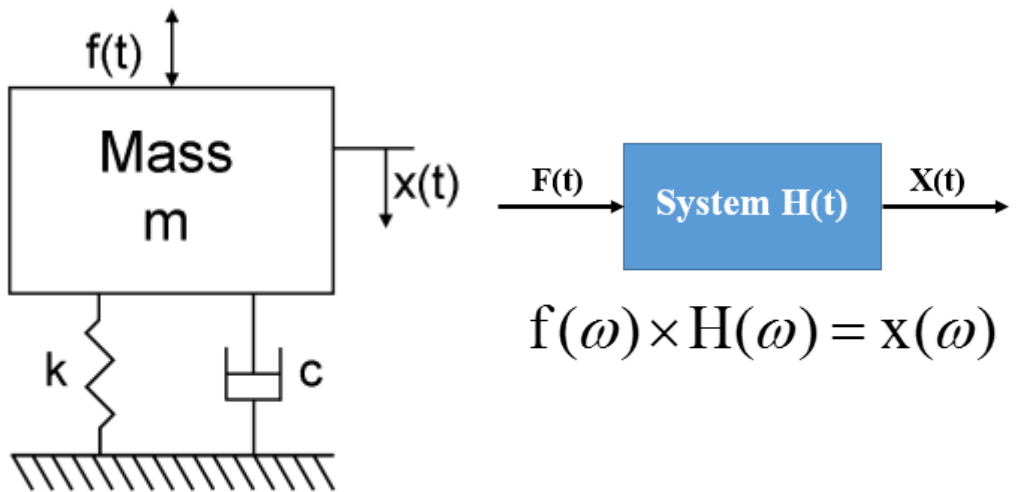


Figure 4.10 Single degree of freedom system [151]

$$m\ddot{x} + c\dot{x} + kx = f(t) \quad (4.2)$$

Practical structures can be realistically modelled by the linear superposition of many single-degree-of-freedom (SDoF) systems. The model and equation of motion of a SDoF system are shown in Fig. 4.10 and Equation 4.2. The model includes a mass (m) and a spring (k) plus when damped, a viscous dashpot (c). $f(t)$ and $x(t)$ are the general time-varying force and displacement response of the structure [151].

The frequency response function (FRF) is the ratio of the output response to the input excitation in the frequency domain, which can be used to extract the natural frequencies, mode shapes, and damping of a structure. Both the input excitation and the output response

CHAPTER 4

are recorded in the time domain and are converted into the frequency domain by the Fast Fourier Transforms (FFT). According to the definition of the FRF, the FRF of the SDof system $H(\omega)$ is calculated by solving the equation of motion of the SDof system [151]. The FRF of a system can be calculated using the velocity, displacement or acceleration depending on the parameter measured from the output response.

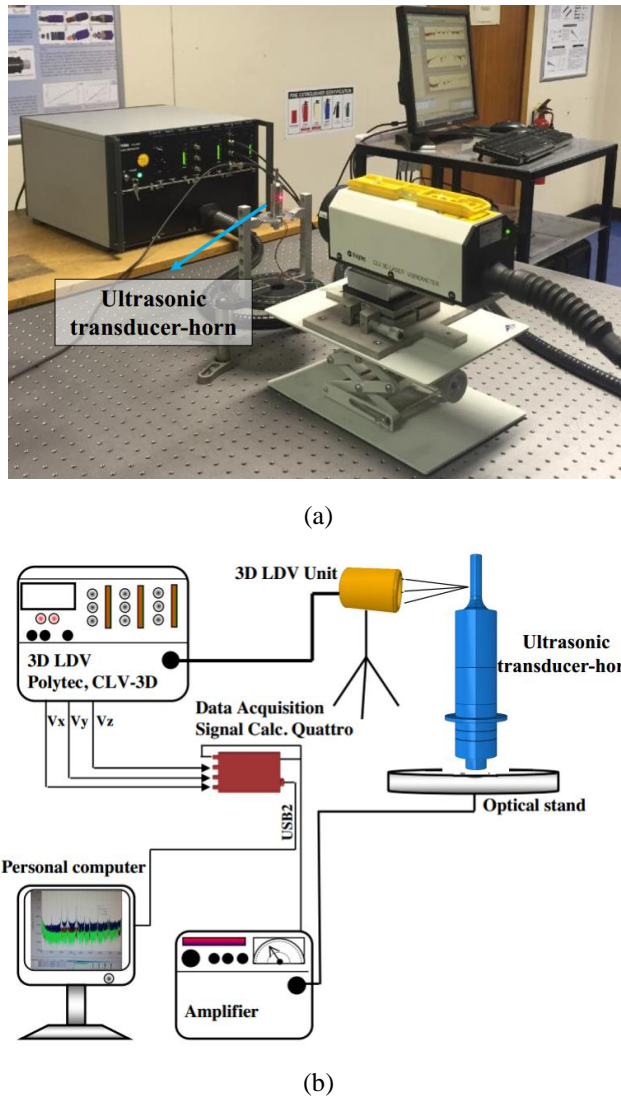


Figure 4.11 EMA of the transducer-horn (a) actual experimental setup (b) schematic diagram of the EMA showing the main components [142]

For the EMA of the ultrasonic transducer-horn, the vibrational responses of a grid of points on the transducer-horn surface were measured and each point can be regarded as a subsystem with three DoFs. The FRF of each measurement point is extracted from the

CHAPTER 4

vibrational response. The transducer-horn has multiple number of DoFs and thus multiple vibrational modes of the transducer-horn should be extracted. To accurately identify the modal parameters of the transducer-horn, the density of the measuring points should be sufficient. Fig. 4.11 shows the experimental setup used for the EMA of the ultrasonic transducer-horn including five main components: the ultrasonic transducer-horn, 3D laser Doppler vibrometry, data acquisition, power amplifier, and PC.

Excitation and measurement

Vibration analysis can be divided into two measurement methods: free vibration and forced vibration. The free vibration method is used to measure the natural vibration response of a structure. This method is normally employed to investigate large structures such as bridges to yield the natural frequencies and damping factors of the structure [122, 151]. On the other hand, the forced vibration method is used to measure the vibration response of a structure excited by a forcing function. The forcing excitation applied to the structure can be implemented by many techniques such as a hammer or an electromagnetic shaker. The forced vibration method is used to conduct the vibration analysis of the ultrasonic transducer-horn. For the EMA of the ultrasonic components, the excitation signals are commonly swept sine or true random. In this work, random excitation is used because it requires short testing time and is easily implemented [122, 149].

The transducer-horn was excited by a signal generator built into the data acquisition (Data Physics Quattro DP240) that provides a random excitation signal. The excitation signal from the signal generator was then amplified by the power amplifier and the level of the excitation signal was chosen to achieve an acceptable signal to noise ratio. A 3D laser Doppler vibrometry (Polytec, 3D CLV-3D) was employed to measure the vibration response of a grid of points on the transducer-horn surface as indicated in Fig. 4.12. There are 68 measuring points equally distributed along the four axial lines on the transducer-horn surface, which is sufficient to identify all of the mode shapes in the measurement frequency range. The vibration response of the ultrasonic transducer-horn should be measured under a free boundary condition, which is an ideal state. It is possible to imitate the free boundary condition by supporting or suspending the target by soft elastic materials, such as elastic

CHAPTER 4

string or sponge. To minimise the effect of supports, the position of the support should be at the flange of the transducer-horn, indicating close proximity to the node points.

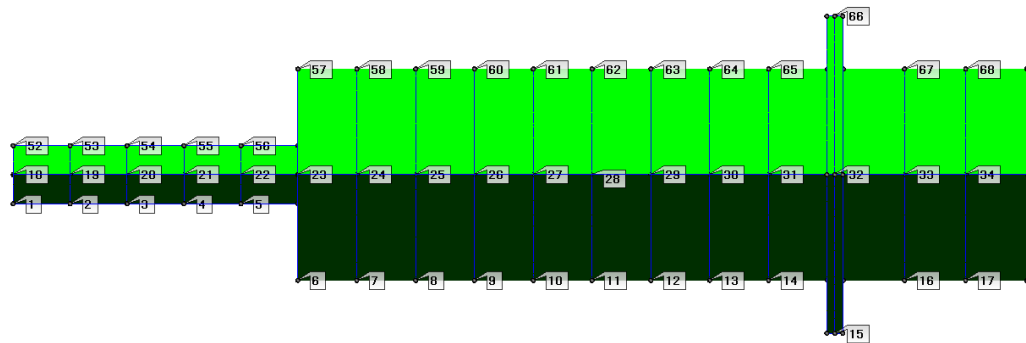


Figure 4.12 Grid points on the ultrasonic transducer-horn

Data processing

The measurement signals from the grid points on the device surface are normally analysed by a spectrum analyser. The frequency response function of the signals can be achieved through the spectrum analyser which collects the measured data, digitises and converts them from time domain to frequency domain using the Fast Fourier Transforms (FFT). The spectrum analyser can also display the frequency response function of the signals on a monitor. For the EMA of the ultrasonic transducer-horn, the sample frequency of the spectrum analyser was 204.8kHz and the number of spectral lines was 51200, indicating a resolution of 1.56Hz over a frequency range of 0-80kHz.

Modal parameter extraction

The modal parameters of the transducer-horn were extracted from the measurement data by the method of FRF curve fitting. Each measuring point on the device surface had three FRFs because three vibrational response components (two in plane and one out of plane of the transducer-horn surface) were measured by the 3D laser Doppler vibrometry for a single point. The set of FRFs generated from the measurement points were exported to the modal analysis software, MEScopeVES (Vibrant Technology Inc) for the curve fitting process and extraction of modal parameters. This software can present vibration modes in a 3D wireframe model at the corresponding resonant frequencies.

4.2.3 Comparison of FEA and EMA

The ultrasonic transducer-horn was tested by EMA, and the purpose was to confirm that the device was vibrating at the design frequency with a pure longitudinal mode. Fig. 4.13 shows the normalised modal peaks functions of EMA of the ultrasonic transducer-horn.

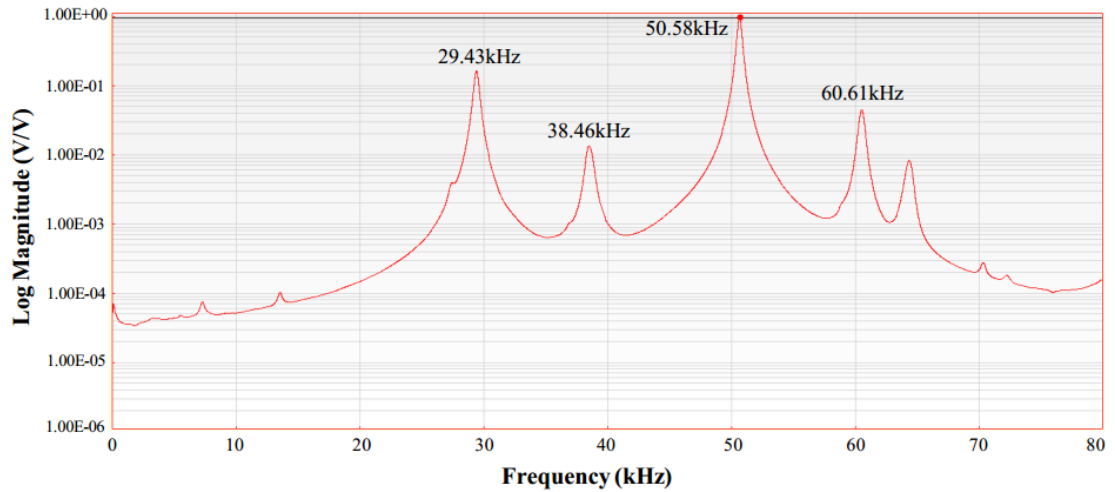


Figure 4.13 The normalised modal peaks functions of EMA of the ultrasonic transducer-horn

For the ultrasonic transducer-horn, the resonant frequency of the 2nd longitudinal mode measured from EMA is 50.58kHz while the resonant frequencies of the 4th bending mode and the 3rd longitudinal mode are 38.46kHz and 60.61kHz, respectively. This indicates that frequency separations of 23.96% between 2nd longitudinal mode and the 4th bending mode, and 19.83% between the 2nd longitudinal mode and 3rd longitudinal mode are achieved. Moreover, the resonant frequency of the 1st longitudinal vibration mode is 29.43kHz, representing a frequency separation of 41.81% between the 2nd longitudinal mode and the 1st longitudinal mode. To avoid modal coupling, the frequency separations between the tuned vibration mode and the surrounding vibration modes should be more than 10% [122]. Thus, for the transducer-horn designed in this work, the frequency separations between the tuned mode and the surrounding modes are sufficient to avoid modal coupling. The resonant frequencies and corresponding mode shapes of the ultrasonic transducer-horn achieved from the EMA and FEA are shown in Fig. 4.14.

CHAPTER 4

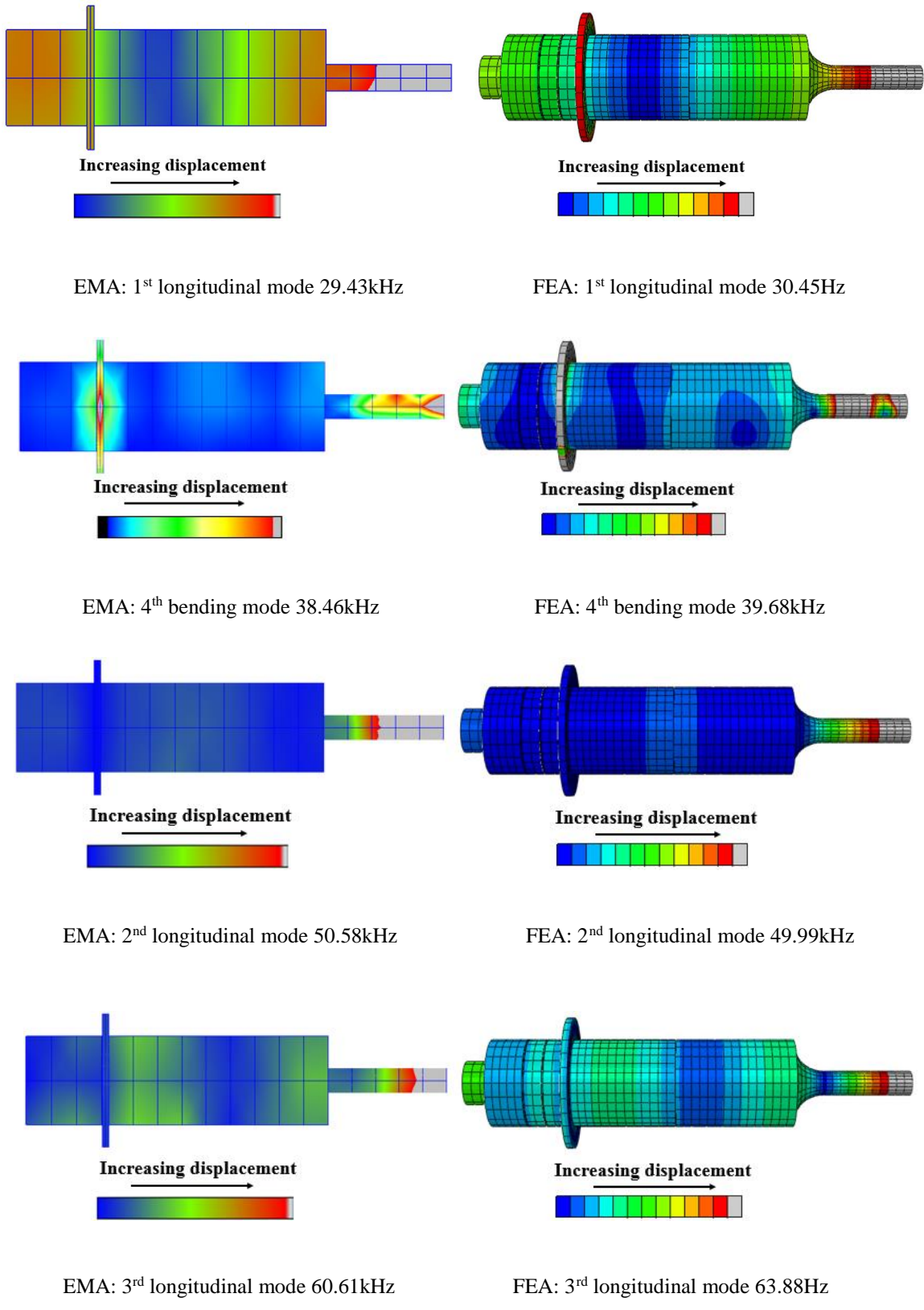


Figure 4.14 The resonant frequencies and corresponding mode shapes of the transducer-horn measured by EMA and predicted by FEA

CHAPTER 4

Fig. 4.14 shows the mode shape and resonant frequency of the tuned mode (2nd longitudinal mode) measured from the experiments, which indicates the ultrasonic transducer-horn operates at the tuned frequency with a pure longitudinal mode. The predicted and measured 2nd longitudinal mode shape are in good agreement. The resonant frequency of the 2nd longitudinal vibration mode predicted by FE model (49.99kHz) also closely matches the resonant frequency extracted from the experimental data (50.58kHz), representing a 1.17% difference. The differences of the resonant frequencies between the FEA and EMA results are 3.46% for the 1st longitudinal mode, 3.17% for the 4th bending mode and 5.39% for the 3rd longitudinal mode. Moreover, the mode shapes of the 1st longitudinal mode, the 4th bending mode, the 2nd longitudinal mode and the 3rd longitudinal mode measured by the EMA are also close to the FE results. The experimental results indicate the FE model of the transducer-horn is an adequate model to estimate the resonant frequencies and mode shapes of the transducer-horn.

4.3 Experimental setup of the ultrasonic-sonic needle system

To measure the impact force, validate the numerical model of the needle system and then optimise the needle system, an US needle system and corresponding experimental rig is designed and manufactured. The other components of the US needle are also investigated, including the free mass and biopsy needle.

4.3.1 The ultrasonic-sonic needle system

The US needle system is presented in Fig. 4.15, which consists of five main parts: an ultrasonic transducer-horn, a free mass, a biopsy needle, a spring and a casing. The spring is placed between the needle and the casing. It is used to supply a pre-load and ensure the whole system remains in contact. The rod at the back of the needle, in Fig. 4.15(b), is used to ensure the free mass travelling axially between the horn tip and the needle. For experimental analysis, the whole system is fixed on an optical table. A load cell (Kistler 9311B), which is in contact with the needle, is used to measure the impact force and therefore the effective impulse can be calculated.

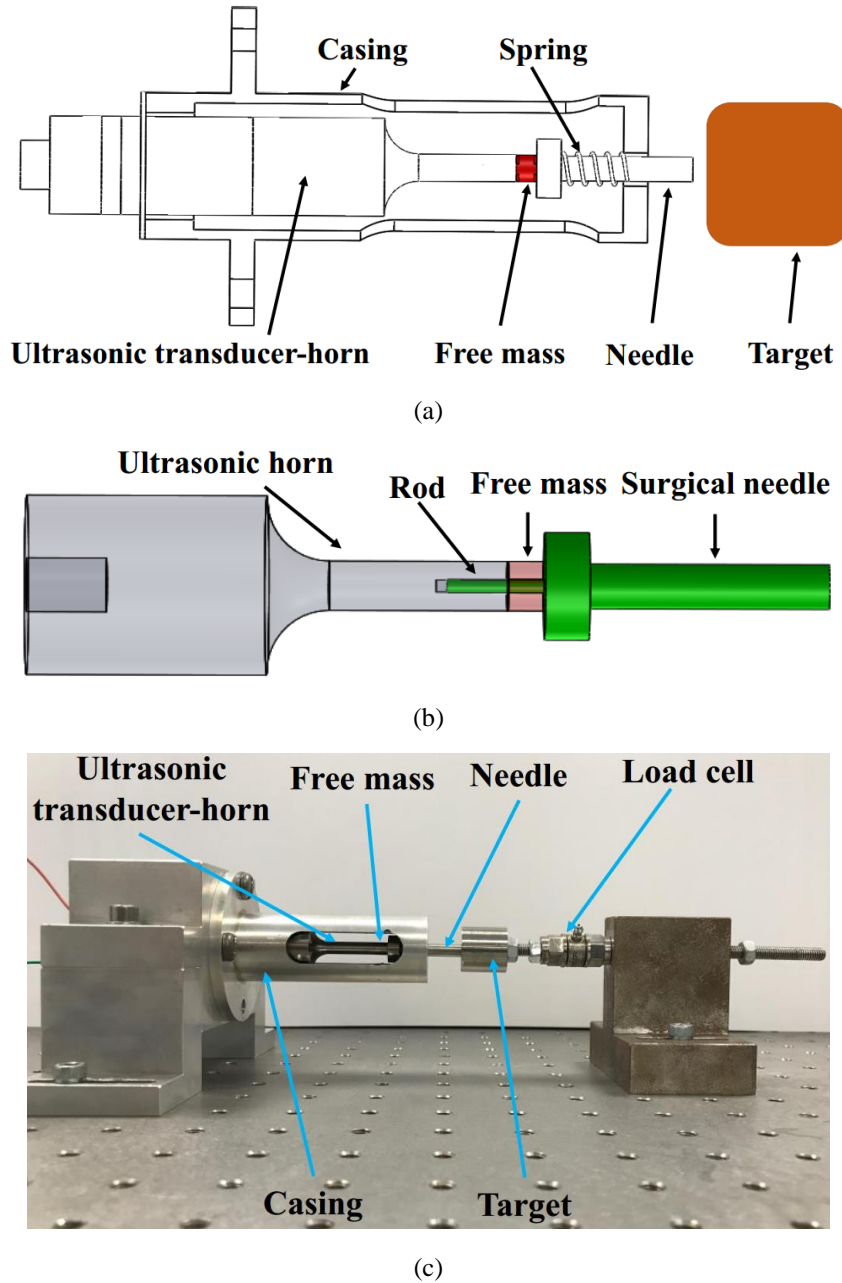


Figure 4.15 US needle system (a) schematic of the US needle system (b) the position of the rod (c) impact force measurement experimental setup

For this design, the US needle is easy to assemble as a hand-held device and it can be used to perform bone biopsy by holding the casing. Moreover, the total length of the needle system is 137.80mm, which is similar to the length of commercial biopsy needles (ranging from 100.00mm to 200.00mm). This size is suitable for the surgeon to perform bone biopsy.

4.3.2 The components of the ultrasonic-sonic needle system

Free mass

The free mass is placed between the ultrasonic transducer-horn and surgical needle, and it receives momentum from the ultrasonic horn and then imparts its momentum to the needle. The shape of the free mass determines the contact type between the horn tip and free mass, and between the free mass and the needle. Contact types can be point contact, line contact or surface contact, and it determines the magnitude of the stress generated in the ultrasonic-horn and needle during the impact process. Indentation damage or fracture in the ultrasonic horn and the needle is produced when the stress in the horn and needle is larger than the ultimate strength of the titanium alloy Ti-6Al-4V. In this section, the shape of the free mass is investigated and five different shapes of free masses are considered, as shown in Fig. 4.16.

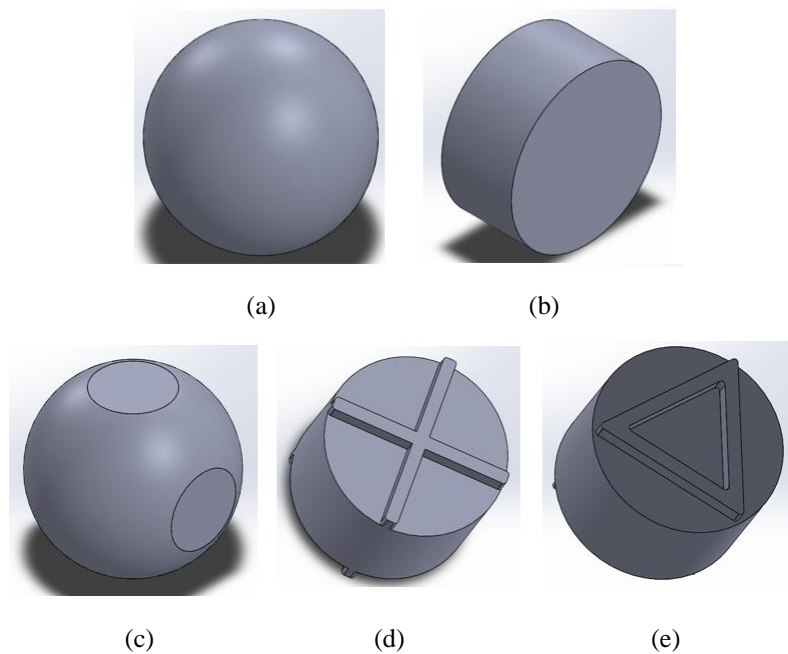


Figure 4.16 Different shapes of free mass (a) spherical free mass (b) cylindrical free mass (c) sphere with four flat faces (d) cylinder with cross profiles (e) cylinder with triangular profiles

These free masses are investigated based on the ultrasonic-sonic needle system 2 (US needle 2) since US needle 1 has not been studied at the free mass design stage. US needle 1 and US needle 2 are shown in Fig. 4.17.

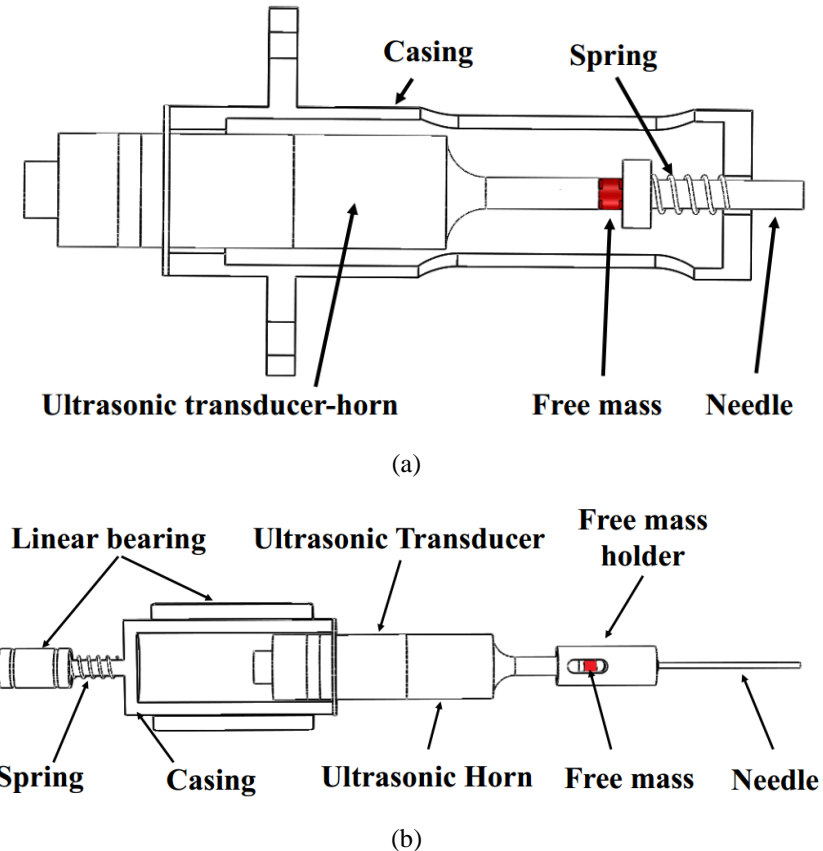


Figure 4.17 Two different US needles (a) schematic of US needle 1 (b) schematic of US needle 2

Both US needle 1 and US needle 2 have the same drilling mechanism. The free mass also vibrates between the ultrasonic horn and the needle for US needle 2. Thus, the free mass designed for US needle 2 can also be used for US needle 1 by machining a hole (1.5mm diameter) at the centre of the free mass. The experimental setup of US needle 2 is shown in Fig. 4.18. The transducer-horn of US needle 2 is fixed in a casing within two linear bearings. It can freely move forwards and backwards with minimal friction. The transducer-horn also operates at the 2nd longitudinal mode. The free mass is in the free mass holder that is manufactured with the needle as one part. During the bone biopsy procedure, the penetration process of US needle 2 is intermittent because the transducer-horn, free mass and needle cannot be kept in contact by the spring placed between the casing and linear bearing. On the other hand, US needle 1 gives a consecutive penetration process because the whole system remains in contact by the spring placed between the needle and casing. Thus, US needle 2 is not adopted in this work. The five different shapes of free masses are discussed below.

CHAPTER 4

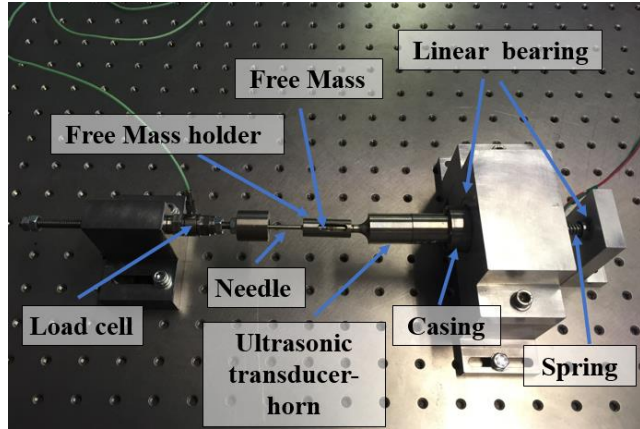


Figure 4.18 Impact force measurement experimental setup of US needle 2

For a spherical free mass, stress concentrations are produced because of the point contacts of the free mass to the horn, and the free mass to the free mass holder. The stress concentrations result in the maximum stress in the ultrasonic horn and needle is larger than the material's ultimate strength. Thus, indentation damage or fracture in the horn and needle is produced. This was reported by a spherical free mass used in an ultrasonic-sonic drill for rock drilling [58].

A cylindrical free mass has a large contact area which has the advantage of reducing stress concentrations. However, it was reported by the NASA Jet Propulsion Laboratory (JPL) that the large contact area also created strong coupling with the horn, which changed the vibrational characteristics of the system, making the impacting process difficult to start [153]. For the ultrasonic-sonic rock drilling device invented by the JPL, the contact area between the horn tip and a cylindrical free mass is 62.04mm^2 . On the other hand, for the needle devices, the contact area between the horn tip and a cylindrical free mass is 23.75mm^2 , which is about one third of the contact area produced by the ultrasonic-sonic rock drilling device. Thus, the cylindrical free mass is tested to investigate whether it can be used for US needles. The third type of free mass, a sphere with four flat faces, has the appropriate contact area for the needle system but is difficult to manufacture due to high toughness properties of the material. To avoid high stress concentrations, but to ensure that the system can easily vibrate, cylinders with cross profiles (or triangular profiles) on the top and bottom surfaces are proposed. In this work, the cylindrical free mass and the cylinder with cross profiles are selected and tested for the US needle.

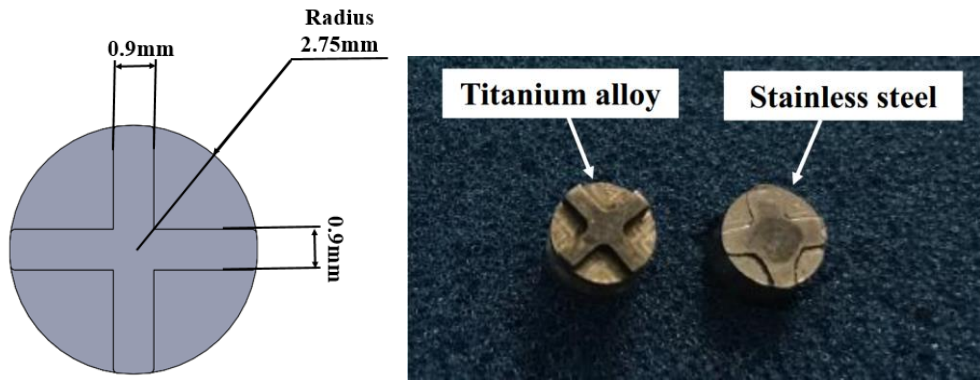


Figure 4.19 Testing the titanium free mass and stainless steel free mass for US needle

The cylinder with cross profiles was first investigated and the material used to manufacture the free mass was also studied. Two free masses (5.5mm diameter) were made of titanium alloy Ti-6Al-4V and stainless steel 316, respectively. The mass of the free mass significantly affects the effective impulse delivered to the target and hence also affects the stress generated in the ultrasonic horn and the needle during the impact process. Thus, the two free masses with the same mass 0.63g were manufactured. For the two free masses, the cross profiles on the top and bottom surface had the same dimensions, as shown in Fig. 4.19, and the thickness of the cross profile is 0.5mm. The length of the titanium and stainless steel masses were 7mm and 4mm, respectively. The two free masses were tested using US needle 2 with the same configuration: the same transducer-horn (Fig. 4.8), the same vibration amplitude of the horn tip, a needle with 15g mass and impacting the same target (titanium metal block shown in Fig. 4.18). The tests were ran for 20 minutes for the two free masses and the testing results are shown in Fig. 4.19. It can be seen that the cross profile on the free mass made of stainless steel had severe indentation damage. However, no indentation damage occurred on the free mass made of titanium alloy and the dimensions of the cross profile was same as before the test. Further testing of the titanium free mass was conducted. The titanium free mass was tested for 2 hours and there was still no damage observed on the cross profile.

For the cylindrical free mass, it was made of titanium alloy Ti-6Al-4V and used to test whether it resulted in US needles difficult to vibrate. A cylindrical free mass with the dimensions of a 5mm length and a 5.5mm diameter was tested using US needle 2. The vibration amplitudes of the horn tip were varied from $8\mu\text{m}$ to $12\mu\text{m}$, which were the vibration amplitudes used to conduct penetration tests. The free mass was observed to move freely

CHAPTER 4

during the testing. In this work, the cylindrical free mass is selected because it can reduce the stress concentration to avoid horn damage and is also easy to manufacture compared to the free mass with cross profiles (or triangular profiles). Previous work (from the Medical and Industrial Ultrasonics Group of the School of Engineering of the University of Glasgow) investigated the material of the cylindrical free mass used for an ultrasonic-sonic device for rock drilling (Ultrasonic planetary core drill, UPCD) [58, 154]. This work confirms the results using the cross profile free mass configuration, shown in Fig. 4.19, where the cylindrical free mass made of the stainless steel was shown to deform while titanium cylindrical free mass was robust under typical operating condition.

Based on the above discussion, the free mass used for the US needle is determined: a cylindrical free mass with a 1.50mm diameter hole located at the centre of the free mass, made of titanium alloy Ti-6Al-4V.

Biopsy needle

The biopsy needle receives the momentum from the free mass and then moves forward to impact the target. The geometry of the needle tip significantly affects the penetration performance. A needle tip with a large contact area will decrease the pressure delivered to the target, which results in the device failing to penetrate the target. Fig. 4.20 shows common geometries of the needle tip used for bone biopsy.

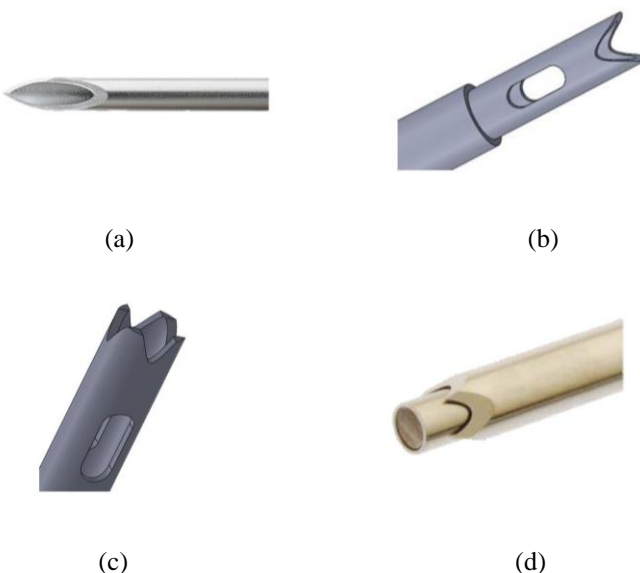


Figure 4.20 Needle tip geometries used for bone biopsy (a) bevel-shaped needle tip (b) fish-mouth-shaped needle tip (c) needle with multiple teeth (d) multi-bevel shaped needle

CHAPTER 4

The bevel-shaped needle tip is the most common needle used for soft and hard tissue biopsy. It is easy to manufacture and the bevel angle of the needle tip can be easily adjusted according to design requirements. The bevel-shaped needle tip also has a relatively small contact area with the target and this can greatly improve the pressure delivered to the target. However, for hard tissue biopsy (cortical bone), the quality of the biopsy sample achieved by this kind of needle is usually unsatisfactory. This is because the shape of the needle tip is not symmetric and the uneven penetration force causes the needle to extract an irregularly shaped biopsy sample, which will have a negative influence on the clinical analysis of the sample. The needle tip geometries, in Fig. 4.20(b) and 4.20(c), are symmetric while they both have a common drawback, which is a large contact area with the target. This means a large penetration force is required in order to penetrate the target. For the multi-bevel shaped needle in Fig. 4.20(d), the contact between the needle tip and the target is a point contact at the beginning of biopsy procedure, which is helpful in penetrating the target. Then, the contact changes to line contact as the procedure progresses, but the contact area between the needle and target is still small. Thus, the force required to penetrate the target for the multi-bevel shaped needle is much smaller than the other needle tip geometries. Moreover, the multi-bevel shaped needle tip is also symmetric which means a high quality biopsy sample can be extracted. The multi-bevel needle (CareFusion Ltd., TJC4011 and TJC4008), in Fig. 4.20(d), is selected in this work for bone biopsy.

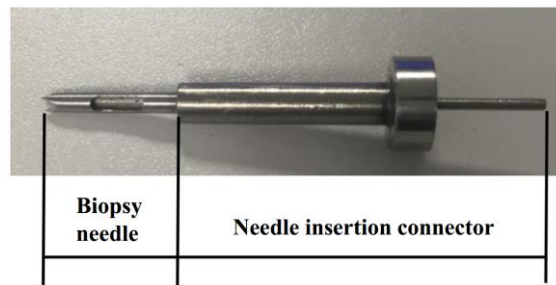


Figure 4.21 The assembled biopsy needle for the US needle

Commercial biopsy needles are normally manufactured as a tube with a thin wall thickness. The needle will therefore be damaged if the free mass directly impacts the biopsy needle. To avoid needle damage and ensure the needle receives the momentum from the free mass, a needle insertion connector is designed, as shown in Fig. 4.21. There are two methods that

CHAPTER 4

can be used to assemble the needle and the connector: one is achieved by press fit and the other is to assemble them together by thread fit. The method of thread fit is a reliable way to assemble the needle and the connector, and it also has the advantage of easily replacing the needle for single-use. In this work, it is difficult to implement the method of thread fit on a commercial needle. The reason is that the wall thickness of the needle is small and thus the threaded part of the needle is easily fractured during operation. The purpose of this work is to investigate the feasibility of the ultrasonic-sonic drilling mechanism applied in a surgical device by testing a prototype in biomechanical test samples. The needle will be used multiple times in the test programme and thus the method of press fit is more useful for assembly of the needle and the needle insertion connector. A slot at the left end of the assembled needle is also manufactured to retrieve the biopsy sample.

The material of the commercial biopsy needle is stainless steel 316 while the needle insertion connector is made of titanium alloy Ti-6Al-4V. The connector requires a high strength to prevent indentation damage.

Casing and spring

The casing has two roles in this work. One is that the casing is held to perform biopsy tests and the other is to fix the casing with the mounting, as shown in Fig. 4.15(c). There are four clearance holes evenly distributed on the flange indicated in Fig. 4.22, which are used to fix the casing. A slot is manufactured to observe and measure the motion of the ultrasonic transducer-horn, free mass, and assembled needle.

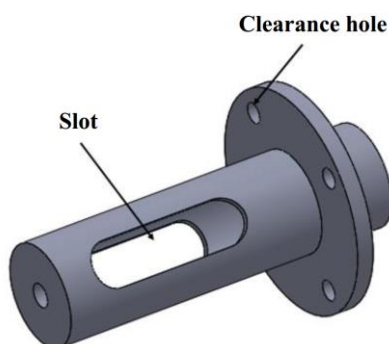


Figure 4.22 Schematic of the casing used for the US needle

CHAPTER 4

The spring plays an important role in the US needle. An extremely low or high level of spring pre-load results in a low level of effective impulse and hence failure to penetrate the target. For example, a high level of pre-load, which creates a strong coupling between the dynamic components (the transducer-horn, free mass and needle), causes the needle system difficulties to vibrate. On the other hand, a low level of pre-load significantly reduces the number of impacts between the horn and free mass, and between the free mass and surgical needle. This also reduces the effective impulse delivered to the target. To investigate the pre-load and spring rate effects on the performance of the needle system, a set of compression springs (Lee Spring) were adopted, with spring rates from 1.68N/mm up to 4.7N/mm (1.68N/mm part number: LC026D02S, 2.92N/mm part number: LC030D01S and 4.7N/mm part number: LCM080D01S). The optimal pre-load and spring rate are determined based on maximising the effective impulse delivered to the target, which is presented in Chapter 5.

4.4 Chapter Conclusion

Optimisation of the ultrasonic horn for the US needle was studied in this chapter, based on transferring the maximum momentum to the free mass. An FE model of the horn impacting the free mass was developed to evaluate the performance of different horn configurations, and a horn was selected based on the post-impact velocity of the free mass. From the simulation results, a stepped horn with 5.5mm tip diameter was selected and manufactured for the US needle system.

The stepped horn with 5.5mm tip diameter and the ultrasonic transducer were assembled and modelled in Abaqus to ensure the assembled ultrasonic transducer-horn operated at 50kHz. The ultrasonic stepped horn and each part of the ultrasonic transducer were manufactured and the assembled system was evaluated by electrical impedance analysis and experimental modal analysis. The electrical impedance analysis indicated that the resonant frequency of the ultrasonic transducer-horn is at 50.73kHz, which is close to the target design frequency. The ultrasonic transducer-horn operating at the tuned frequency with a pure longitudinal mode has been validated by the EMA. The resonant frequency of the 2nd longitudinal vibration mode predicted by FEA (49.99kHz) closely matches the resonant frequency extracted from the experimental data (50.58kHz), representing a 1.17% difference. This

CHAPTER 4

indicates the FE model of the ultrasonic transducer-horn is able to predict these modal parameters of the transducer-horn.

The components of the US needle (free mass, biopsy needle, casing and spring) were also investigated. A cylindrical free mass was selected because it can reduce the stress concentrations between the free mass and ultrasonic horn to avoid horn damage, and is also easy to manufacture compared to a cylindrical free mass with cross profiles. For the needle configuration, a multi-bevel needle was adopted to achieve a high quality biopsy sample and maximise the pressure delivered to the target. To investigate the effect of the pre-load and spring rate on the performance of the needle system, spring rates from 1.68N/mm up to 4.7N/mm were adopted in this work. The assembled US needle will be used to conduct a parametric study to maximise the effective impulse delivered to the target by simulations and experiments.

Chapter 5 Modelling and optimisation of the ultrasonic-sonic needle system

Once the prototype of the US needle was manufactured, the next aim of the research was to build a mathematical model to simulate the working process and optimise the US needle. Two approaches were used: FEM and a mass-spring-damper (MSD) modelling approach. FEM has been used to tune the ultrasonic transducer-horn and predict its vibrational behaviour. Furthermore, the FE model of the transducer-horn impacting the free mass, which was developed in Chapter 4, will be used to calculate the contact time between the transducer-horn and free mass. The effective mass of the ultrasonic horn was calculated from this contact time, which was used to verify the effective mass value of the horn achieved by MSD method. To model the continuous collision process between the components of the US needle, a MSD modelling approach was undertaken. Fig. 5.1 shows the mathematical model of the needle system built in Matlab/Simulink to simulate the entire dynamic stack and analyse the dynamic behaviour. Each part of the dynamic stack was modelled as a MSD model. The mathematical model of the US needle was developed by assembling each unit of the dynamic MSD model and then running in Matlab/Simulink to calculate the impact force delivered to the target.

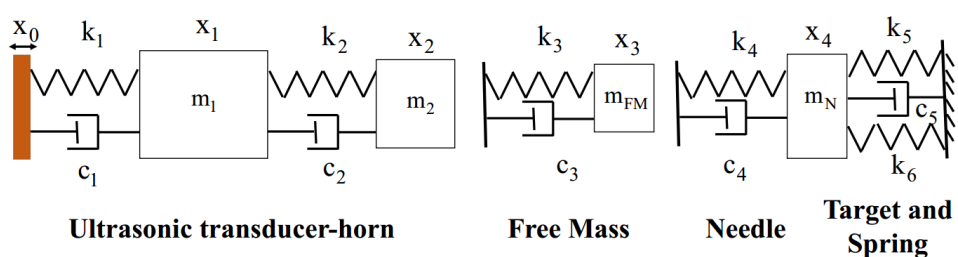


Figure 5.1 The MSD model of the US needle

In Fig. 5.1, k_{1-4} , m_{1-4} and c_{1-4} represent the contact stiffness, effective mass and damping coefficient of the dynamic components, respectively. x_0 represents the vibrational displacement of the piezo-ceramic stack in the ultrasonic transducer. k_5 and c_5 are the

CHAPTER 5

contact stiffness and damping coefficient of the target material and k_6 is the stiffness of the spring.

In this chapter, the method of modelling each dynamic component as a MSD model will be presented. The dynamic equations used to describe the motion of US needle system are obtained and entered into Matlab/Simulink to calculate the velocity of each dynamic component and the impact force delivered to the target. The numerical model is validated through experiments using a prototype needle, which records the velocities of free mass and needle, the impact time duration and the impact force by a laser Doppler vibrometry, an ultra-high speed camera and a load cell respectively. To validate the model, the simulated and measured forces are compared in terms of magnitude of the force, number of force peaks and different level force distribution within the same time period. The value of the effective impulse for different spring pre-loads is also calculated and compared between experiment and simulation to further verify the accuracy of the US needle MSD model. Lastly, the US needle is optimised by the MSD model to achieve the maximum effective impulse. A parametric study (the mass of the free mass, spring pre-load and spring rate) is conducted by the MSD model to determine the optimal configuration of the needle system. The optimal configuration of the US needle refers to the needle system can deliver the maximum effective impulse to the target.

5.1 The MSD model of the ultrasonic transducer-horn

A mathematical model used to simulate the ultrasonic transducer-horn is first presented. There are a number of papers explaining ultrasonic transducer-horn modelling, but majority of them focus on FEM to design the transducer and investigate modal parameters [114, 115, 155]. In this section, the transducer-horn is modelled as a one-dimensional numerical model, which is used to simulate the impact process of the US needle and analyse the dynamic behaviour of the needle system.

5.1.1 Numerical model

The process of modelling the ultrasonic transducer-horn as a MSD model is shown in Fig. 5.2. The transducer-horn can be divided into three parts: a back section, one piezo-ceramic

CHAPTER 5

ring and a front section. The front section is defined as a two-step titanium alloy bar with different area of cross sections. There are two nodal points on the transducer-horn: one is near the piezo-ceramic rings and the other is located near the step of the horn. The displacement at the nodal point is zero, therefore the back section can be removed in the model because of the existence of the nodal point near the piezo-ceramic ring [156]. The ultrasonic transducer-horn can be represented by a two DOF model, consisting of two parts:

- The single piezo-ceramic ring model
- The front section of the transducer-horn expressed as two mass-spring-damper sets

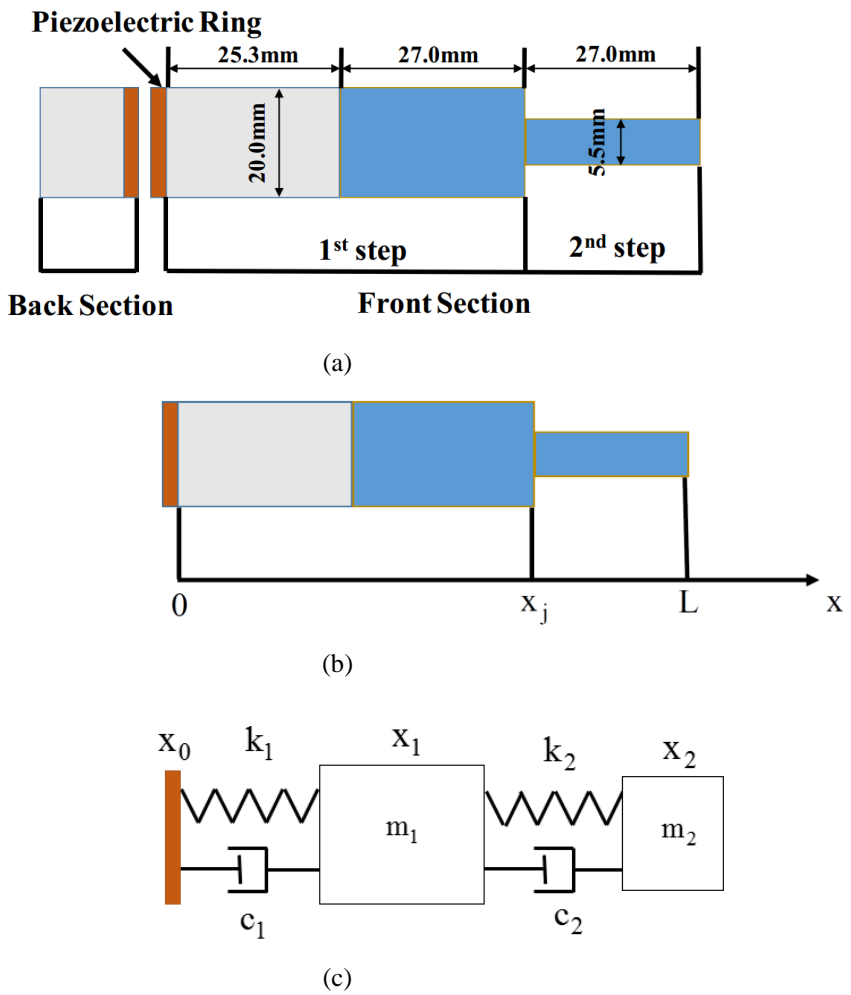


Figure 5.2 Modelling the ultrasonic transducer-horn as a 2-DOF system: (a) structure of the ultrasonic transducer-horn (b) simplification of the ultrasonic transducer-horn (c) the MSD model of the ultrasonic transducer-horn

CHAPTER 5

In Fig. 5.2(c), m_1 and m_2 represent the effective mass of the first and second step mass, respectively. k_1 , k_2 , c_1 and c_2 are the stiffness and damping of the transducer-horn. x_0 stands for the displacement of the piezo-ceramic ring, x_1 and x_2 are the displacement of the two parts m_1 and m_2 . The coordinate of the step position is x_j . The next step is to determine the parameters of the piezo-ceramic ring model and the transducer-horn front section model, based on the dimensions of the transducer-horn and the properties of the piezo-ceramic rings.

The parameters of the transducer-horn front section model are first considered and calculated. The piezo-ceramic ring is temporarily removed and the left end of the model is regarded as immovable. The undamped 2-DOF system is initially analysed and then the damping coefficients can be obtained from experiments. The undamped model of the transducer horn are shown in Fig. 5.3.

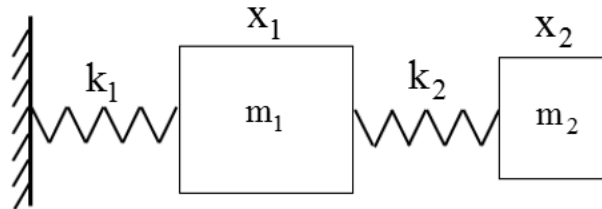


Figure 5.3 The undamped 2-DOF model of the transducer-horn

The 2-DOF model of the transducer-horn front section has two different vibration modes with two corresponding resonant frequencies: the first vibration mode stands for the first and second step masses vibrating in phase, and the second vibration mode represents the first and second step masses vibrating in anti-phase. The resonant frequencies of the undamped 2-DOF model are calculated based on the dimensions of the transducer-horn. The results are shown in Table 5.1.

CHAPTER 5

Table 5.1 The resonant frequencies of the undamped 2-DOF model

Vibration mode	Resonant frequency	
	f (kHz)	ω (rad/s)
The first vibration mode (vibrating in phase)	23.33	1.47×10^5
The second vibration mode (vibrating in anti-phase)	47.19	2.96×10^5

The value $f_2 = 47.19\text{kHz}$ is selected as the operating frequency of the transducer-horn as this resonant frequency allows the first and second masses to vibrate in anti-phase, which is consistent as the transducer-horn driven in practice. The method of calculating the parameters of the 2-DOF model is shown below.

According to Newton's second law, the dynamic equations of the undamped 2-DOF model are expressed as:

$$k_1x_1 + m_1\ddot{x}_1 + k_2(x_1 - x_2) = 0 \quad (5.1)$$

$$m_2\ddot{x}_2 - k_2(x_1 - x_2) = 0 \quad (5.2)$$

The equations for x_1 and x_2 can be expressed as follows because the longitudinal vibration is harmonic.

$$x_1 = D_1 \sin(\omega t) \quad (5.3)$$

$$x_2 = D_2 \sin(\omega t) \quad (5.4)$$

D_1 and D_2 are the vibration amplitude of m_1 and m_2 , respectively. D_1 is equal to the maximum vibration amplitude of the first step; D_2 represents the vibration amplitude at the

CHAPTER 5

end of the horn tip that is the maximum amplitude of the second step. The natural angular frequency of the system is denoted by ω . Substituting x_1 and x_2 into Equation 5.1 and 5.2:

$$(k_1 + k_2 - m_1 \omega^2)D_1 - k_2 D_2 = 0 \quad (5.5)$$

$$-k_2 D_1 + (k_2 - m_2 \omega^2) D_2 = 0 \quad (5.6)$$

Changing Equation 5.5 and 5.6 to matrix form:

$$M\lambda\Psi = K\Psi \quad (5.7)$$

$$M = \begin{bmatrix} m_1 & 0 \\ 0 & m_2 \end{bmatrix} \quad K = \begin{bmatrix} k_1 + k_2 & -k_2 \\ -k_2 & k_2 \end{bmatrix}$$

$$\lambda = \begin{bmatrix} \omega_1^2 & 0 \\ 0 & \omega_2^2 \end{bmatrix} \quad \Psi = \begin{bmatrix} \Psi_1 & \Psi_2 \\ 1 & 1 \end{bmatrix} \quad (5.8)$$

Where Ψ_1 and Ψ_2 represent the ratio of the vibration amplitude between the first step and second step mass when the 1st vibration mode and 2nd vibration mode are excited, respectively. Ψ_2 can be obtained from experimental measurements when the ultrasonic transducer operates in the 2nd vibration mode (vibrating in anti-phase). The values of D_1 and D_2 are measured by a 3D laser Doppler vibrometry and thus Ψ_2 is known. Ψ_1 can be also calculated from Equation 5.13.

Equation 5.7 can be expressed as follows:

$$M^{-1}K\Psi = \lambda\Psi \quad (5.9)$$

Letting $Q = M^{-1}K$, the expression for Q is shown below:

CHAPTER 5

$$Q = \begin{bmatrix} q_1 & q_2 \\ q_3 & q_4 \end{bmatrix} = \begin{bmatrix} \frac{k_1 + k_2}{m_1} & -\frac{k_2}{m_1} \\ -\frac{k_2}{m_2} & \frac{k_2}{m_2} \end{bmatrix} \quad (5.10)$$

According to Equation 5.9 and 5.10, the following equations can be calculated.

$$\begin{cases} q_1\Psi_1 + q_2 = \omega_1^2\Psi_1 \\ q_3\Psi_1 + q_4 = \omega_1^2 \\ q_1\Psi_2 + q_2 = \omega_2^2\Psi_2 \\ q_3\Psi_2 + q_4 = \omega_2^2 \end{cases} \quad (5.11)$$

$$q_3 = -\frac{k_2}{m_2}$$

$$q_4 = \frac{k_2}{m_2}$$

Due to $q_3 = -q_4$, Equation 5.11 is reduced to three equations and Equation 5.13 is also calculated.

$$\begin{cases} q_1\Psi_1 + q_2 = \omega_1^2\Psi_1 \\ q_3\Psi_1 + q_4 = \omega_1^2 \\ q_1\Psi_2 + q_2 = \omega_2^2\Psi_2 \end{cases} \quad (5.12)$$

$$\omega_1^2 - \omega_2^2 = \omega_1^2\Psi_2 - \omega_2^2\Psi_1 \quad (5.13)$$

Substituting the expressions for q_1 , q_2 , q_3 and q_4 into Equation 5.12, the following equations are obtained.

$$\begin{cases} (m_1\omega_1^2 - k_1 - k_2)\Psi_1 - k_2 = 0 \\ m_2\omega_1^2 + (\Psi_1 - 1)k_2 = 0 \\ (m_1\omega_2^2 - k_1 - k_2)\Psi_2 + k_2 = 0 \end{cases} \quad (5.14)$$

CHAPTER 5

In Equation 5.14, there are four unknown parameters (k_1 , k_2 , m_1 , m_2) whose values cannot be identified using three equations. To determine the solutions of Equation 5.14, a fourth equation is sought for the calculation of the four unknown parameters. It is assumed that the energy distributed in the 2-step transducer-horn (in Fig. 5.2(b)) is equal to the energy of the 2-DOF MSD model. The total strain energy of the transducer-horn structure is expressed as follows:

$$U = \frac{E}{2} \left[S_{\text{step1}} \int_0^{x_j} \left(\frac{dD_1(x)}{dx} \right)^2 dx + S_{\text{step2}} \int_{x_j}^L \left(\frac{dD_2(x)}{dx} \right)^2 dx \right] \quad (5.15)$$

S_{step1} and S_{step2} are the area of the first step cross section and the second step cross section, respectively. According to the wave equation and the boundary conditions of the transducer-horn front section, $D_1(x)$ and $D_2(x)$ are calculated and shown in Equation 5.16 and 5.17, which describe the displacement of the first step and second step, respectively.

$$D_1(x) = A \sin(k_{wn} x) \quad 0 < x < x_j \quad (5.16)$$

$$D_2(x) = B \cos[k_{wn}(x - L)] \quad x_j < x < L \quad (5.17)$$

The value of A and B are equal to D_1 and D_2 , respectively. k_{wn} is the wavenumber and is equal to $\sqrt{\rho\omega^2/E}$. Substituting $D_1(x)$ and $D_2(x)$ into Equation 5.15,

$$U = \frac{E}{2} \left[S_{\text{step1}} \int_0^{x_j} A^2 k_{wn}^2 \cos^2 k_{wn} x dx + S_{\text{step2}} \int_{x_j}^L B^2 k_{wn}^2 \sin^2 k_{wn} (x - L) dx \right] \quad (5.18)$$

The energy of the ultrasonic transducer-horn can be calculated because all of the parameters in Equation 5.18 can be measured in experiments for a specific transducer-horn. Therefore, the value of U is known. The energy of the 2-DOF model is shown below:

$$U_{\text{MSD}} = \frac{1}{2} k_1 D_1^2 + \frac{1}{2} k_2 (D_2 - D_1)^2 \quad (5.19)$$

CHAPTER 5

The energy U_{MSD} is equal to the value of U ; therefore, the fourth equation is determined.

$$\begin{cases} (m_1\omega_1^2 - k_1 - k_2)\Psi_1 - k_2 = 0 \\ m_2\omega_1^2 + (\Psi_1 - 1)k_2 = 0 \\ (m_1\omega_2^2 - k_1 - k_2)\Psi_2 + k_2 = 0 \\ \frac{1}{2}k_1D_1^2 + \frac{1}{2}k_2(D_2 - D_1)^2 = U \end{cases} \quad (5.20)$$

The parameters (k_1 , k_2 , m_1 , m_2) can be calculated by solving Equation 5.20, which are shown below.

$$k_1 = 4.79 \times 10^8 \text{ N/m}$$

$$k_2 = 1.18 \times 10^8 \text{ N/m}$$

$$m_1 = 20.27 \text{ g}$$

$$m_2 = 1.49 \text{ g}$$

The next step is to calculate the parameters of the piezo-ceramic ring model. The piezo-ceramic ring used in this work is PZT-8, which is ideally suitable for ultrasonic drilling and ultrasonic welding as explained in Chapter 3. The displacement of the piezo-ceramic ring x_0 is given below [156]:

$$x_0 = \frac{s_{33}^E l_0}{S_0} F_0 + d_{33} u \quad (5.21)$$

$$F_0 = c_1(\dot{x}_1 - \dot{x}_0) + k_1(x_1 - x_0) \quad (5.22)$$

Where F_0 is the interaction force between the piezo-ceramic ring model and the 2-step mass, and u is the voltage applied to the transducer; l_0 and S_0 are the thickness and the area of the piezo-ceramic ring respectively; s_{33}^E and d_{33} are the properties of the piezo-ceramic rings, which represent the elastic compliance at constant electric field and the piezo-ceramic

CHAPTER 5

charge constant, respectively. Values of l_0 , S_0 , s_{33}^E and d_{33} are calculated based on the properties and dimensions of the piezo-ceramic rings, and are presented as below.

$$l_0 = 4.00 \times 10^{-3} \text{ m}$$

$$S_0 = 2.64 \times 10^{-4} \text{ m}^2$$

$$s_{33}^E = 1.37 \times 10^{-11} \text{ m}^2 / \text{N}$$

$$d_{33} = 2.40 \times 10^{-10} \text{ C/N}$$

Substituting the values of l_0 , S_0 , s_{33}^E and d_{33} into Equation 5.21,

$$x_0 = 2.08 \times 10^{-10} F_0 + 2.40 \times 10^{-10} u \quad (5.23)$$

The piezo-ceramic ring model and the transducer-horn front section model are developed and thus the whole ultrasonic transducer-horn model can be achieved. Equations of motion for the ultrasonic transducer-horn system are expressed below:

$$m_1 \ddot{x}_1 + c_1 (\dot{x}_1 - \dot{x}_0) + k_1 (x_1 - x_0) + c_2 (\dot{x}_1 - \dot{x}_2) + k_2 (x_1 - x_2) = 0 \quad (5.24)$$

$$m_2 \ddot{x}_2 - c_2 (\dot{x}_1 - \dot{x}_2) - k_2 (x_1 - x_2) = 0 \quad (5.25)$$

Equations 5.21, 5.22, 5.24 and 5.25 describe the dynamic behaviour the transducer-horn model, which are input into Matlab/Simulink to construct the numerical model of the US needle. The damping coefficients c_1 and c_2 are selected to ensure the vibration amplitudes of m_1 and m_2 in the simulation model are the same as the vibration amplitude at the middle part of the first step mass D_1 and the vibration amplitude at end of the second step mass D_2 in experiments, respectively. To calculate the values of c_1 and c_2 , D_1 ($1.19\mu\text{m}$) and D_2 ($12.25\mu\text{m}$) are measured from experiments using a 3D laser vibrometry. According to the measurement values of D_1 and D_2 , the damping coefficients c_1 and c_2 are tuned in the MSD model to match the simulated vibration amplitudes to the experimental measurements. Their values are shown below.

$$c_1 = 0.03 \text{Ns/m}$$

$$c_2 = 0.081 \text{Ns/m}$$

5.1.2 Evaluation of the ultrasonic transducer-horn MSD model

The ultrasonic transducer-horn model is built in Matlab/Simulink according to Equations 5.21, 5.22, 5.24 and 5.25. The simulation results of the transducer-horn model are shown in Fig. 5.4, which shows the displacement of the first mass (m_1) and second mass (m_2) in 0.5 seconds. It can be seen that the transient response of the ultrasonic vibration lasts 0.07 seconds and then the transducer-horn vibration reaches its steady state. The simulation data during the steady state is also expanded to verify the accuracy of the numerical model: the blue line shows the vibration amplitude of the second mass and the pink line represents the first mass vibration amplitude.

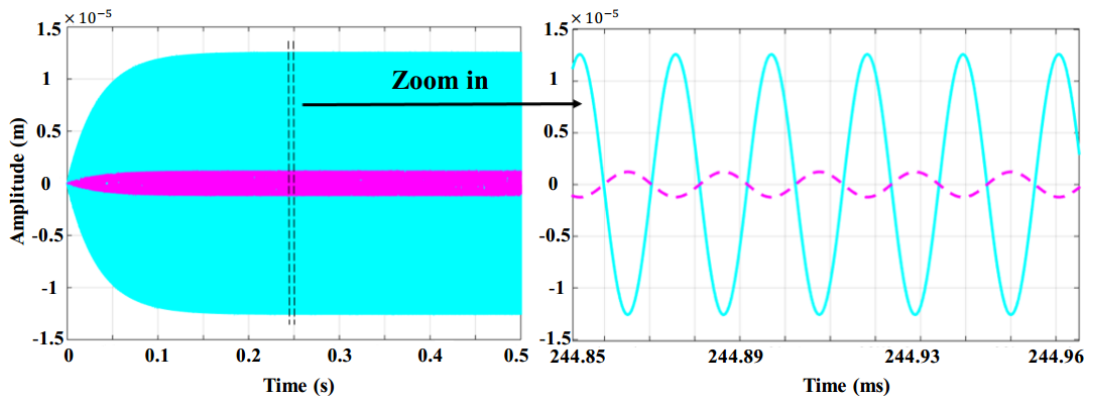


Figure 5.4 Ultrasonic vibration of the ultrasonic transducer-horn model: the blue line shows the vibration displacement amplitude of the 2nd mass and the pink dashed line represents the 1st mass displacement

The simulation results demonstrate that the vibration amplitudes of the first and second mass are $1.22\mu\text{m}$ and $12.5\mu\text{m}$ zero-to-peak, respectively. The simulation results are in good agreement with the experimental results ($D_1 : 1.19\mu\text{m}$, $D_2 : 12.25\mu\text{m}$). It can also be seen from Fig. 5.4 that the first and second mass are vibrating at the second vibration mode (vibrating in anti-phase), and at the resonant frequency of 47.19kHz. Consequently, the MSD

model of the ultrasonic transducer-horn is adequate to simulate the dynamic behaviour of the ultrasonic transducer-horn.

5.1.3 The effective mass of the ultrasonic horn

The momentum of the free mass achieved from the ultrasonic transducer-horn depends on two factors: the vibration amplitude of the horn tip and the effective mass of the ultrasonic horn. The vibration amplitude of m_2 from the MSD model ($12.5\mu\text{m}$) is in agreement with the experimentally measured horn tip vibration amplitude ($12.25\mu\text{m}$). The effective mass is defined as the distance travelled by the wave propagating in the material during the impact event, which has been explained in Section 4.1.1 [58]. The ultrasonic transducer-horn impacting the free mass was modelled in Abaqus and was used to calculate the effective mass of the ultrasonic horn. The FE model is shown in Fig. 5.5. The effective mass value calculated from the FE model is compared to the mass of m_2 obtained from the MSD model.

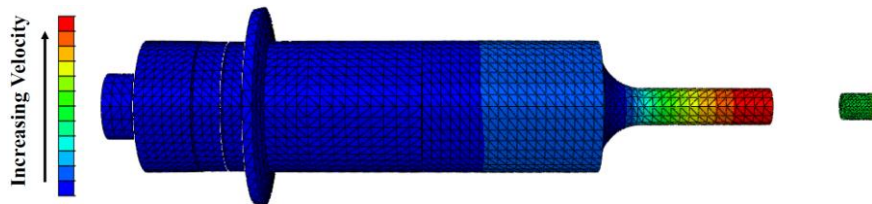


Figure 5.5 FE model of ultrasonic transducer-horn impacting the free mass: the transducer-horn operating at 49.99kHz, 2nd longitudinal mode

This impact model was developed in Chapter 4. The ultrasonic transducer-horn and free mass were modelled as a homogeneous 3D deformable solid and the tetrahedron element (C3D10M) was applied to the ultrasonic transducer-horn and free mass as explained in Chapter 4. The material of the free mass was titanium alloy Ti-6Al-4V and the constituent materials of the ultrasonic transducer-horn were presented in Table 3.4 and Table 3.6. The free mass was originally placed in front of the horn tip with zero velocity. The excitation signal was an AC voltage with a frequency of 50kHz applied to the piezo-ceramic rings, which was converted to mechanical vibrations of the transducer-horn. The transducer-horn retreated first and then advanced to impact the free mass. The contact time between the

CHAPTER 5

ultrasonic transducer-horn and free mass can be extracted from the FE model, which was found to be 2.9×10^{-6} s. The speed of sound in the titanium alloy Ti-6Al-4V is approximately 5027m/s and therefore the length of the effective mass of the horn tip is 1.46cm. The effective mass of the horn tip was calculated as 1.54g, which closely matches the value of m_2 (1.49g) of the MSD model. The mass of m_2 calculated from the transducer-horn MSD model had a good agreement with the effective mass estimated from the FE model.

5.2 The MSD model of the ultrasonic-sonic needle system

To build the whole MSD model of the US needle system, the ultrasonic horn-free mass MSD model, free mass-surgical needle MSD model and needle-target model are also studied and developed.

5.2.1 Free mass-surgical needle MSD model

The MSD model, which is used to investigate the interaction between the free mass and surgical needle, is shown in Fig. 5.6. The dimensions of the free mass and the assembled biopsy needle are small, therefore it can be considered that the effective masses of the free mass m_{FM} and needle m_N are equal to the material masses of the free mass and the needle insertion connector, respectively. The contact stiffness k_4 and damping coefficient c_4 of the dynamic model are determined by the contact time and coefficient of restitution during an impact [157], as shown in Equations 5.26, 5.27 and 5.28. To develop the dynamic model between the free mass and surgical needle, there are two assumptions applied to calculate the parameters of the dynamic model. First, the contact stiffness k_4 and damping coefficient c_4 remain constant for each impact [57, 58]; the second assumption is the impacts between the free mass and surgical needle are elastic collisions, which means there is no energy loss during the impact event.

CHAPTER 5

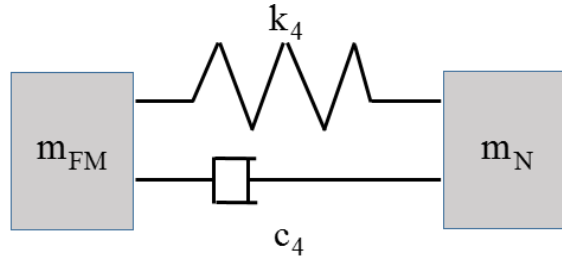


Figure 5.6 MSD model of the impact between free mass and needle

$$c_4 = \frac{2m_N \ln B}{(1+\mu)t} \quad (5.26)$$

$$k_4 = \frac{m_N}{(1+\mu)t^2} (\pi^2 + (\ln(B))^2) \quad (5.27)$$

$$\mu = \frac{m_N}{m_{FM}} \quad (5.28)$$

Where t is the contact time and B is the coefficient of restitution. The coefficient of restitution B is equal to 1 because it is assumed the impact is an elastic collision; therefore, the damping coefficient c_4 is zero and the contact stiffness is determined from the contact time t . To calculate the contact stiffness of the dynamic model, an ultra-high speed camera (Shimadzu Corp., HPV-X) was employed to measure the contact time between the free mass and needle. Since the biopsy needle in Fig. 5.7 is small and light, it does not have an important influence on the impact force delivered to the target [58]. To avoid biopsy needle tip failure, the biopsy needle was removed from the needle insertion connector during the experiment. The experimental setup used to measure the contact time is shown in Fig. 5.8.

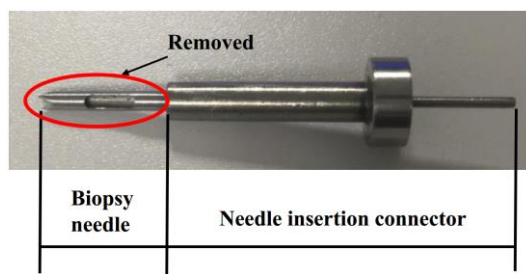


Figure 5.7 The assembled biopsy needle

CHAPTER 5

The frame rate and resolution of the ultra-high speed camera used to measure the contact time were 500000fps and 400 (horizontal) \times 250 (vertical) pixels, respectively. The illumination source was adjusted in line with the camera to achieve a high quality image of the target. The ultrasonic transducer-horn was driven at the tuned frequency, with the horn tip vibrating at an amplitude of 12 μ m. The mass of the free mass was 0.53g with a diameter 5.5mm and a length of 5.5mm; the needle had a mass of 9.2g. The ultra-high speed camera began to record the impact process between the free mass and needle when the US needle system reached steady state vibration. The contact time was calculated from the images recording the impact process.

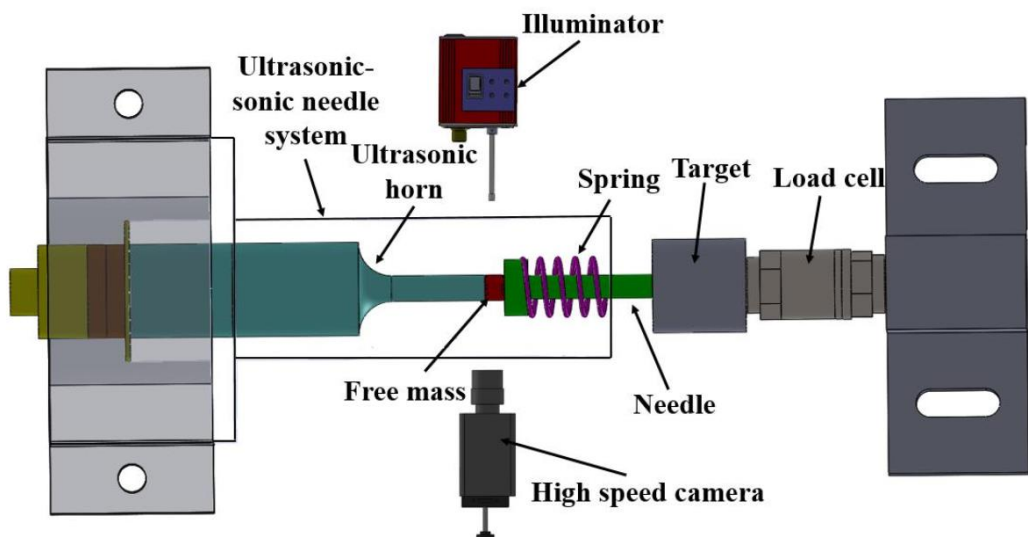


Figure 5.8 Schematic of contact time measurement experimental setup

Fig. 5.9 shows the imaging parts of the needle system: the left, middle and right parts in the images are the ultrasonic horn tip, free mass and surgical needle, respectively; it also describes one impact cycle between the free mass and the needle. For the measurement of contact time, 256 images were recorded and the frame rate was set as 500000fps. This configuration of the ultra-high speed camera ensured that the impact process between the free mass and needle could be effectively captured. Three images were selected from an impact cycle, indicating the stages of pre-impact, during impact and post-impact. The small gap between the free mass and needle was considered as an indicator to calculate the start and end time. The average value of the contact time achieved from 30 impact events was

CHAPTER 5

$25\mu\text{s}$, which was substituted into Equation 5.27 to calculate the contact stiffness k_4 . It should be noted that the value of k_4 calculated in this method was an initial estimation as the contact time between the free mass and the needle was difficult to be accurately measured. Both the free mass and the surgical needle were moving during the imaging process which made it difficult to identify a clear gap to determine the contact time. In comparison, the images produced from the collision between the surgical needle and target were improved in terms of a presentation of a clear gap and contact because the target was static. In addition, light diffraction induced a shadow that resulted in it difficult to accurately determine the beginning and end of contact. Therefore, taking into account both the high speed camera and 3D laser vibrometry measurement results, the value of k_4 was initially calculated based on the contact time measurement, and then was adjusted to ensure the velocities of the needle and free mass from MSD model was consistent with the experimental results.

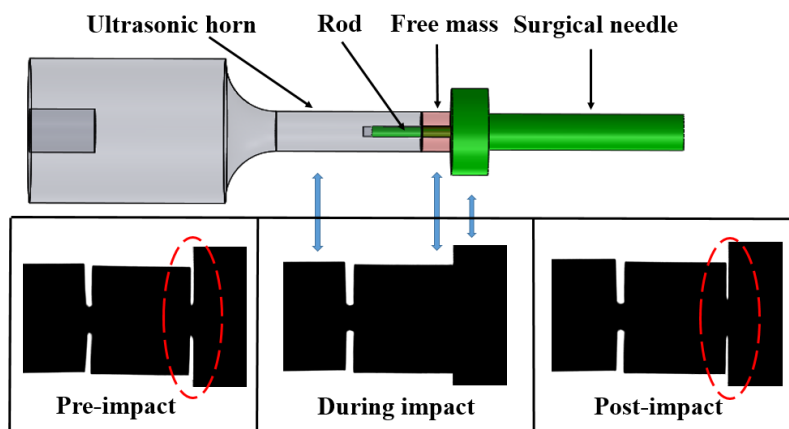


Figure 5.9 One impact cycle between the free mass and needle

For measurement of the contact time between the horn tip and free mass, a shadow was also observed at the beginning and end of the contact. This had a great influence on calculation of the contact time because the transducer-horn operated at ultrasonic frequency 50kHz , and thus the contact time between the horn tip and free mass was small (below $5\mu\text{s}$). It was observed from experiments that the shadow was lasting more than $2\mu\text{s}$ when the horn tip was about to impact free mass. The contact time between the horn tip and free mass cannot be accurately achieved from the ultra-high speed camera measurement. The FE model of the

CHAPTER 5

ultrasonic transducer-horn impacting the free mass described in Section 5.1.3 was employed to calculate the contact time between the horn tip and free mass, which is substituted in Equation 5.27 to calculate the contact stiffness k_3 . Similarly, the value of k_3 is then determined by the measurements of the needle and free mass velocities to ensure the simulated results were consistent with the experimental results.

5.2.2 The contact stiffness and damping coefficient of the target

The target material used in this work is a titanium metal block connected to a load cell, used to measure the impact force. The metal block is a more idealistic target than the bone to evaluate the accuracy of the MSD model and determine the optimal configuration of the US needle. The titanium metal block can give the consistent testing conditions for the needle system with different configurations. On the other hand, bone is an anisotropic, hierarchical and heterogeneous material, and hence the mechanical properties are not consistent for the same bone at different positions. Thus, use of bone as the target cannot accurately determine the optimal configuration of the needle system. The contact stiffness of the target k_5 is determined by the impact duration. Thus, k_5 can be calculated by keeping the contact time consistent between experiment and simulation during the needle impacting the metal block [156]. To determine the value of the contact stiffness k_5 , the contact time between the needle and metal block was also measured using the ultra-high speed camera. The experimental setup (used to measure the contact time between the needle and target) was similar to that used for the free mass and needle impact. The frame rate of the ultra-high speed camera was changed to 200000fps to increase the recording time. This ensured the impact process between the needle and the target can be recorded. The resolution of the ultra-high speed camera was 400 (horizontal) \times 250 (vertical) pixels. The ultrasonic transducer horn operated at the tuned frequency, with the horn tip vibrating at an amplitude of 12 μm . Fig. 5.10 shows the images of the impact between the needle and target: the left and right parts in the images are the surgical needle and metal block, respectively. It also shows the motion of the needle during one impact, which can be used to calculate the contact time.

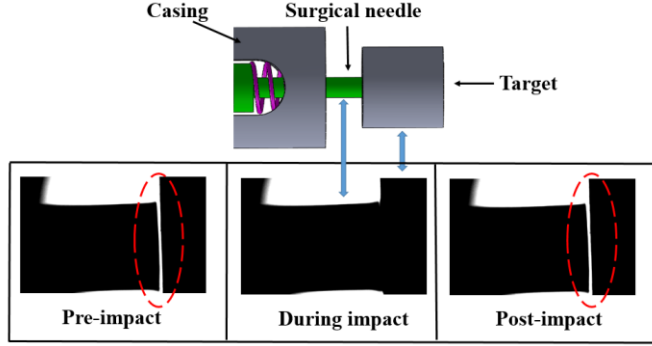


Figure 5.10 Images of the needle during one impact

The average contact time (30 impact events) between the needle and metal block measured from the experiment is 0.077ms (standard deviation 0.011ms). This value is used in the MSD model of the needle system to estimate the contact stiffness k_5 . The simulated impact force can be seen in Fig. 5.11, indicating the contact time between the needle and the target. The average contact time in the MSD model is 0.054ms while the contact stiffness of the metal block is 36.6MN/m. This contact stiffness value can ensure the impact force simulated from the MSD model is consistent with the measured impact force. Consequently, the contact stiffness value of the target was set as 36.6MN/m. The difference in the contact time between the experimental and simulated results is 0.023ms due to the induced shadow preventing an accurate determination for the beginning and end of an impact. The damping coefficient c_5 can be tuned in such a way that the simulated needle velocity matches the experimentally measured needle velocity [156].

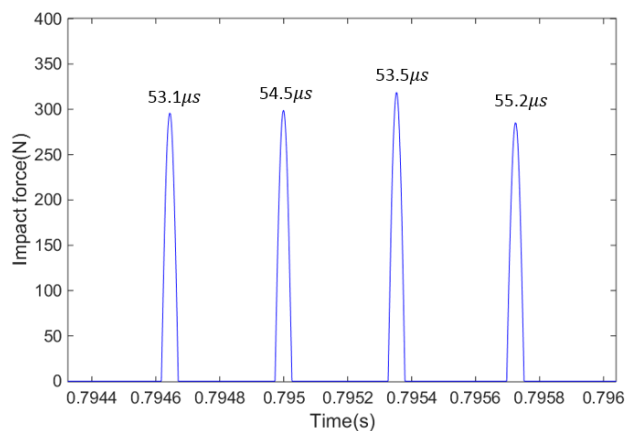


Figure 5.11 Simulated impact force used to show the contact time between the surgical needle and target

5.2.3 Dynamic equations of the ultrasonic-sonic needle system

Fig. 5.12 shows the MSD model of the US needle system. x_0 to x_4 are used to express the displacement of each component (piezo-ceramic ring, ultrasonic transducer-horn, free mass and surgical needle). The dynamic equations used to describe the motion of each dynamic component are shown in Equations 5.29-5.33. Equations 5.29 and 5.30 express the motion of the ultrasonic transducer-horn. Equations 5.31-5.33 represent the motion of the free mass and the needle. In Equation 5.33, k_6 , F_{PL} and F_s are the spring rate, spring pre-load and the force of the spring, respectively. The parameters of k , c and m for each component has been calculated based on the methods explained in Section 5.1, 5.2.1 and 5.2.2. Equations 5.29-5.33 are input to Matlab/Simulink to build the MSD model and simulate the dynamic behaviour of the US needle. The MSD model is also used to calculate the velocity of each dynamic component and the impact force delivered to the target.

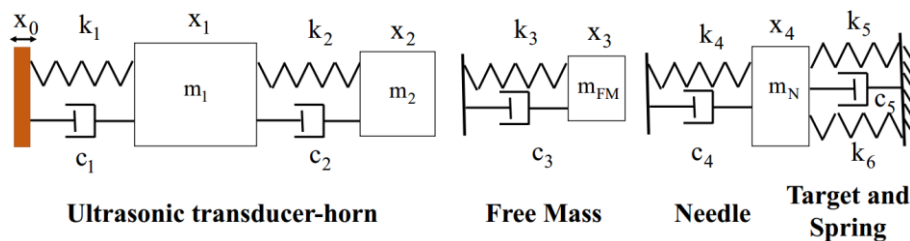


Figure 5.12 The MSD model of the US needle system

$$m_1 \ddot{x}_1 = k_1(x_0 - x_1) + c_1(\dot{x}_0 - \dot{x}_1) - k_2(x_1 - x_2) - c_2(\dot{x}_0 - \dot{x}_1) \quad (5.29)$$

$$m_2 \ddot{x}_2 = k_2(x_1 - x_2) + c_2(\dot{x}_1 - \dot{x}_2) - k_3(x_2 - x_3) - c_3(\dot{x}_2 - \dot{x}_3) \quad (5.30)$$

$$m_{FM} \ddot{x}_3 = k_3(x_2 - x_3) + c_3(\dot{x}_2 - \dot{x}_3) - k_4(x_3 - x_4) - c_4(\dot{x}_3 - \dot{x}_4) \quad (5.31)$$

$$m_N \ddot{x}_4 = k_4(x_3 - x_4) + c_4(\dot{x}_3 - \dot{x}_4) - k_5 x_4 - c_5 \dot{x}_4 - F_s \quad (5.32)$$

$$F_s = F_{PL} + k_6 x_4 \quad (5.33)$$

5.3 Validation of the MSD model of the ultrasonic-sonic needle system

The experimental setup used for validation of the MSD model is shown in Fig. 5.13. The impact force was measured by a load cell and a 3D laser vibrometry was employed to measure the velocities of the free mass and needle. These measurement data were recorded using a data acquisition unit (Picoscope 4424, Pico Technology). The dynamic response of the needle system MSD model was first validated without the presence of the target, and therefore the device operated under free conditions. Then, the MSD model including the target was validated by experiments. The purpose was that the accuracy of the MSD models between the horn tip and free mass, and between free mass and needle, were first considered and validated. Then, the contact stiffness and damping coefficient of the target could be easily validated by the experiments of the impact force measurements when the target was considered.

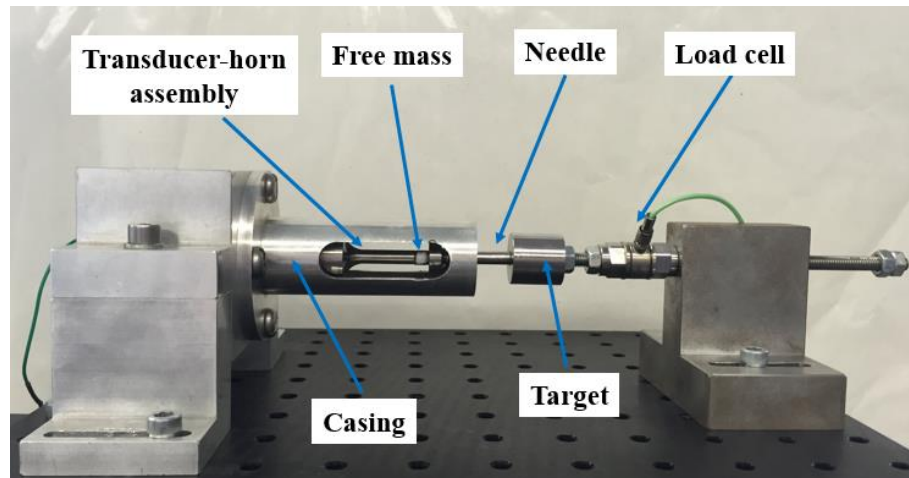


Figure 5.13 Experimental setup used for validation of the MSD model

5.3.1 Validation of the MSD model without the target

The US needle operated under free conditions, indicating the target in Fig. 5.13 was absent. The ultrasonic transducer-horn was driven at its tuned frequency, with the horn tip vibrating at an amplitude of $12\mu\text{m}$. The free mass used in the MSD model and in the experiment had

CHAPTER 5

a mass of 0.53g, a diameter of 5.5mm and a length of 5.5mm; the mass of the needle was 9.2g; the spring rate was 4.7N/mm. The free mass is vibrating between the horn tip and the needle because of the spring. The free mass travels at a constant speed before hitting the needle for each impact. This constant speed of the free mass was recorded for all impacts and averaged for the MSD model validation.

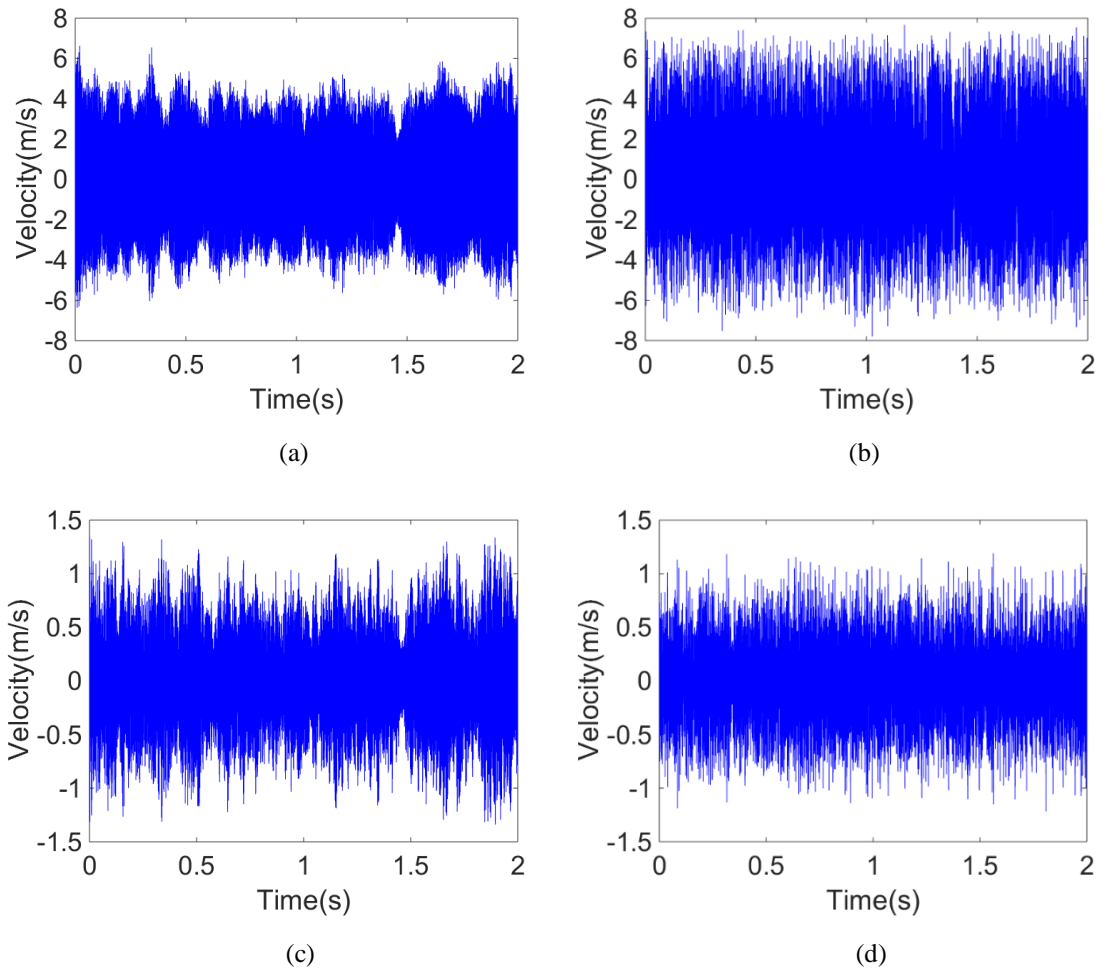


Figure 5.14 Comparison of the simulated velocity and measured velocity (without target): (a) and (b) represent free mass velocities from simulation model and experiment, respectively; (c) and (d) indicate needle velocities from simulation model and experiment, respectively

CHAPTER 5

Table 5.2 Simulation and experiment of free mass average velocity and the average peak value of the needle velocity (without target)

	Simulation	Experiment
Free mass average velocity (m/s)	2.17	2.06
Needle average velocity (m/s)	0.518	0.486

Fig. 5.14 shows the free mass and needle velocities from simulation and experiment. Table 5.2 shows the average velocities of the free mass hitting the needle and the average peak value of the needle velocities in 2 seconds from simulation and experiment. The velocities of the free mass predicted by the numerical model are larger than the experimental results. The difference in the free mass velocities between the simulation and experimental results is 5.3%. Similarly, it can be also observed in the velocity of the needle, where the velocity from simulation result is larger than the experimental result, 6.6% difference. The reason is that the impacts between the horn tip and free mass, free mass and needle are assumed as elastic collisions in numerical model. However, in the experiments, the energy losses of the free mass and surgical needle, especially heat generation, are difficult to be evaluated and thus are not considered in the MSD model. The experimental and numerical results initially show that the MSD model without the presence of the target can be used to simulate the needle system operating in free conditions.

5.3.2 Validation of the MSD model with the target

The target should be included in the MSD model to predict the impact force, optimise the dynamic components and therefore maximise the effective impulse delivered to the target. The contact stiffness and damping coefficient of the target were estimated through the ultra-high speed camera and 3D laser vibrometry measurements as explained in Section 5.2.2. The configuration of the US needle was the same as the one used in Section 5.3.1. In the experiment of impact force measurements, the velocity of the free mass, the velocity of the needle and the impact force delivered to the target were recorded and used to validate the

CHAPTER 5

simulation results. Fig. 5.15 shows the free mass and needle velocities predicted from simulation and measured in experiment, respectively. Table. 5.3 lists the average velocities of the free mass hitting the needle and the average peak values of the needle velocities in 2 seconds from simulation and experiment.

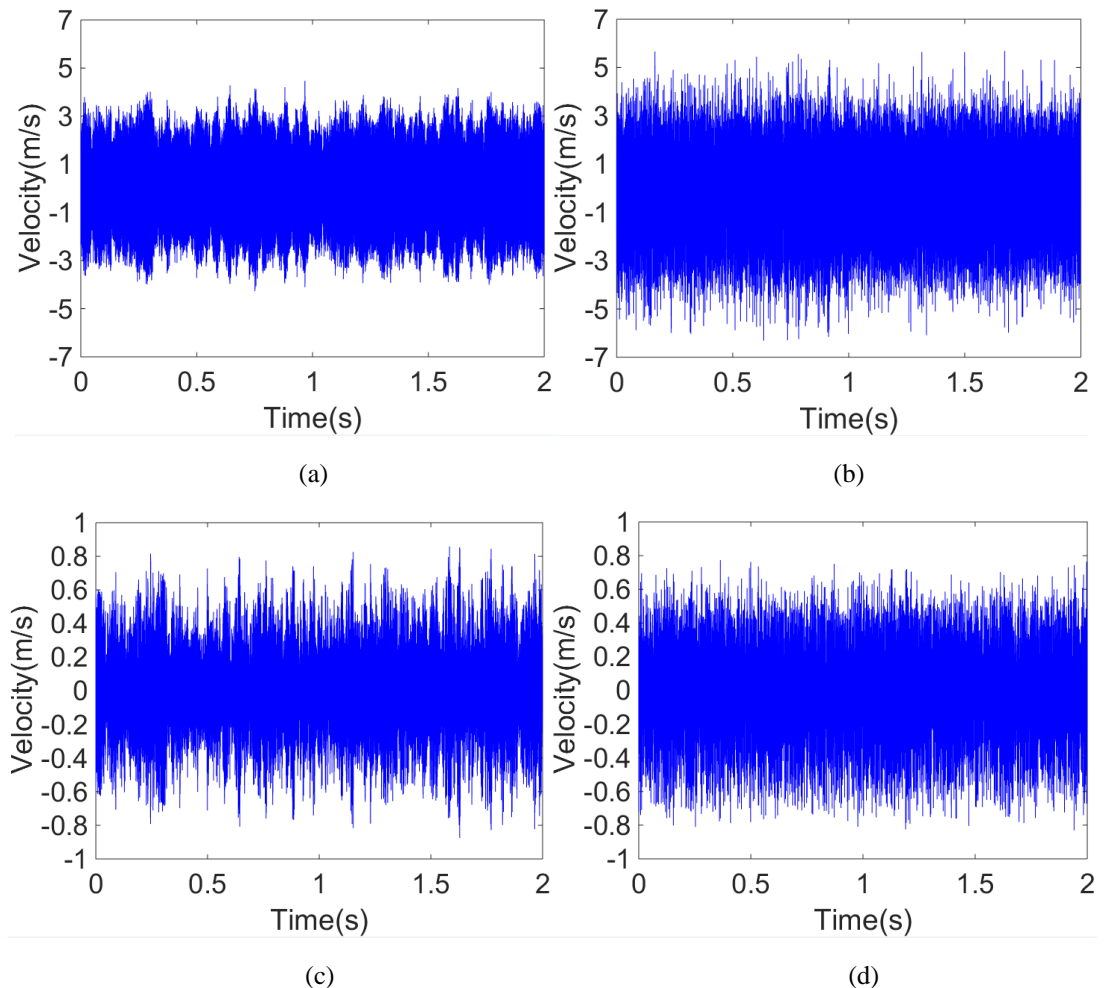


Figure 5.15 Comparison of the simulated velocity and measured velocity (with target): (a) and (b) represent free mass velocity from simulation model and experiment, respectively; (c) and (d) indicate needle velocity from simulation model and experiment, respectively

CHAPTER 5

Table 5.3 Simulation and experiment of free mass average velocity and the average peak value of the needle velocity (with target)

	Simulation	Experiment
Free mass average velocity (m/s)	1.55	1.30
Needle average velocity (m/s)	0.409	0.375

The simulation and experimental results in Fig. 5.15 show the magnitudes of the simulated and measured velocities lie within the same velocity range. The velocities of the free mass and needle from the MSD model are larger than those measured by experiments because of the elastic collision assumption in MSD model (horn tip-free mass impact model and free mass-needle impact model). This is consistent with the results in Section 5.3.1. However, the differences in free mass and needle velocities between simulation and experimental results are increasing, compared to the device operating in free conditions. This can be thought that the energy loss of the free mass and needle in the lateral direction is growing when the target is included in the experiments. In the experiment of impact force measurements, it can also be observed that the lateral motion of the free mass and needle became more drastic in comparison with the unloaded condition, especially for the free mass. However, in the simulation model, the lateral motion of the dynamic component is not considered since the MSD model is a one-dimensional numerical model. The impact forces from the simulation and experiment are shown in Fig. 5.16.

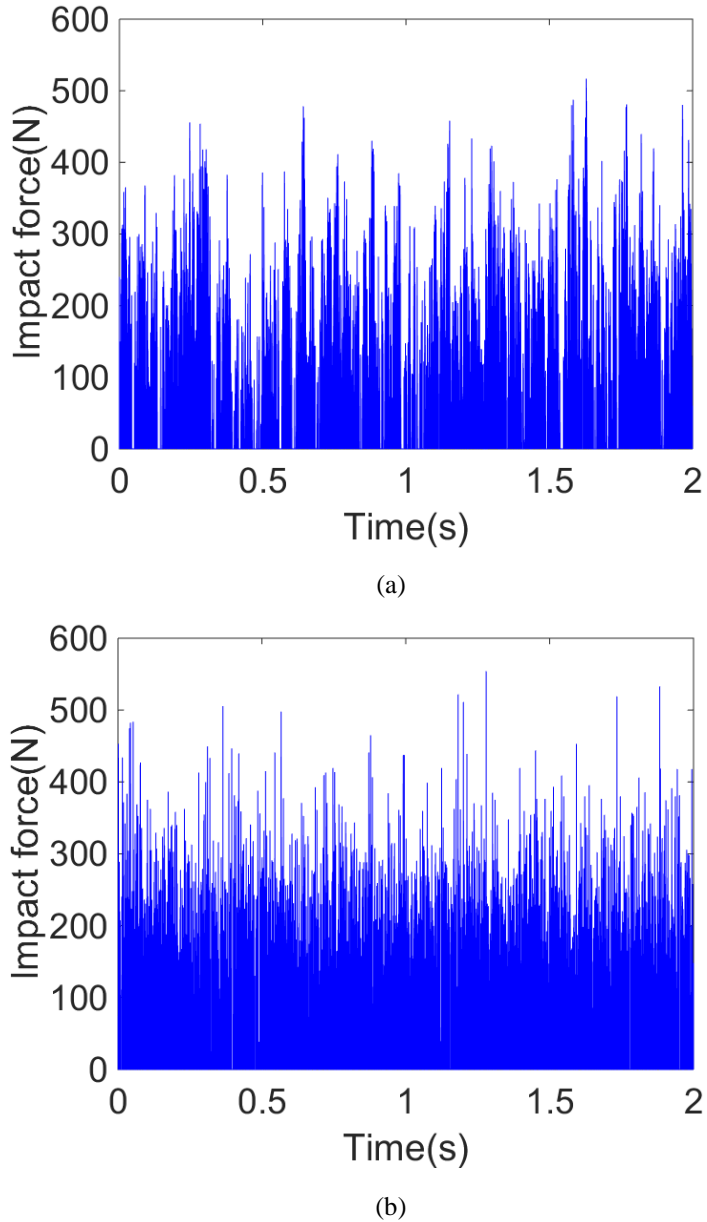


Figure 5.16 Comparison of the simulated impact force and measured impact force (a) the impact force predicted from simulation model (b) the impact force measured from experiment

Fig. 5.16 indicates that the irregular motion of the free mass results in a chaotic force response in simulation and experiment. However, the magnitudes of the simulated and measured impact forces are still in the same force value range. The total number of the simulated and measured force peaks are 2580 and 2438, representing a 5.8% difference. Moreover, the distribution of the impact force values from the simulation and experiment are also studied. The impact forces from the simulation and experiment are compared in the regions of 0N-200N, 200N-400N and 400N-600N. For each region, the number of force

CHAPTER 5

peaks were counted, which was then divided by the total number of force peaks in all region. This calculation was conducted for both simulated forces and measured forces, and the results are shown in Fig. 5.17. The differences in the impact force distribution between the simulation and experiment are listed in Table 5.4. The maximum difference of the impact force distribution is 2.5% for 200-400N region; whilst lower than 2% differences are observed for 0N-200N and 400N-600N regions. Based on these results, conclusion can be drawn that the distribution of the impact force values between the experiment and simulation are in good agreement. Consequently, the MSD model of the US needle has been proven that it can accurately predict the number of force peaks and the distribution of the impact force value.

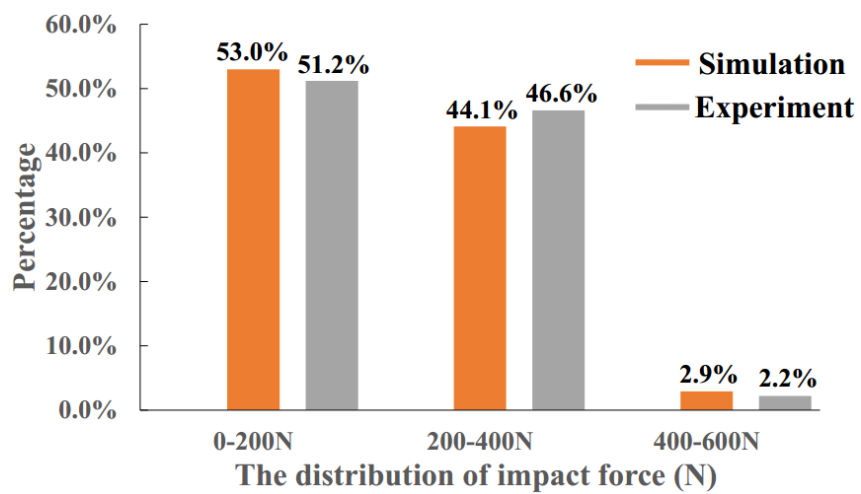


Figure 5.17 Comparison of the impact force distribution between simulation and experiment

Table 5.4 The difference of the impact force distribution between experiment and simulation

Impact force distribution (N)	Difference
0-200	1.8%
200-400	2.5%
400-600	0.7%

CHAPTER 5

It is noted that the number of simulated force peaks in Fig. 5.16(a) seems less than the measured force peaks in Fig. 5.16(b). This is because the dynamic behaviour of the free mass is difficult to keep completely consistent between experiment and simulation. The displacement of the needle determines whether the needle can impact the target, and is largely determined by the momentum of the free mass for each impact. The free mass is vibrating chaotically in the experiment and simulation, and the dynamic behaviour of the free mass in experiment and simulation is different. This results in the impact force occurring at different moment between the experiment and simulation. Additionally, the contact time between the needle and target is also different in experiment and simulation. The impact force signal measured from the experiment is generated by the piezoelectric effect of the load cell. Consequently, the contact time of the measured impact force is not the real contact time and is determined by the configuration of the load cell, which is larger than the real contact time. In the simulation model, the contact time of the impact force is simulated closely to the real contact time achieved from the high-speed camera. Thus, the measured force peaks seems more than the simulated force peaks when the impact forces are overlaid in the same time period. However, this does not affect the accuracy of employing the MSD model to optimise the needle system as the measured and simulated force have been proven that they have a good agreement in terms of the force magnitude, number of total force peaks and different level force distribution.

The validity of the numerical model is further examined by comparing the effective impulse from simulation and experiments, using different spring pre-load values. In experiment and simulation, the ultrasonic transducer-horn was driven at the tuned frequency and the vibration amplitude of horn tip was $12\mu\text{m}$. The free mass had a mass of 0.68g , a diameter of 5.5mm and a length of 7mm . The mass of the needle was 9.2g and the spring rate was 4.7N/mm . The values of the spring pre-load were varied from 7.8N to 14.54N and the corresponding effective impulse delivered to the target was calculated based on an estimation for the compressive strength of bone of 110MPa [81]. The compressive strength of bone varies because bones in different parts of a human body are used to support different forces, and hence the compressive strength of different bones have a large variation. Moreover, bone strength normally decreases when a person gets old. However, it has been studied that the value of the targeted bone compressive strength does not have a significant

influence on the optimisation results [58]. The curve trend of the effective impulse for different spring pre-loads shows good correlation between the simulation and experimental results, as indicated in Fig. 5.18. Both the simulation and experimental results indicate the largest effective impulse can be achieved when the value spring pre-load is 7.8N and that a large spring preload result in a low effective impulse. The effective impulse values predicted by the numerical model are smaller than the experimental results. This is due to the fact that the contact time of the measured impact force is larger than the simulated impact force, as previously discussed. Nevertheless, the numerical model has proven that it can accurately evaluate the performance of the US needle with different configurations. Thus, the numerical model of the needle system can be used as a predictive tool to select the optimal configuration of the needle system and improve the needle penetration performance.

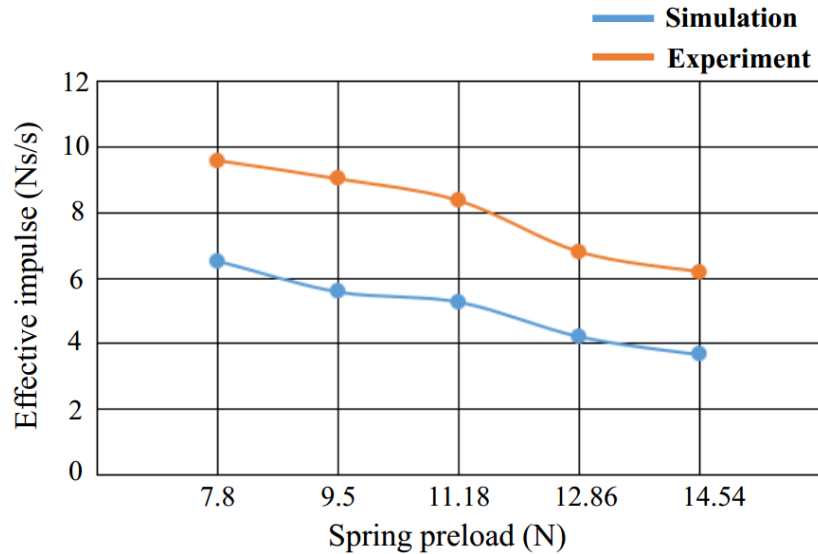


Figure 5.18 The values of effective impulse delivered to the target for different spring pre-loads: orange line is the experimental results and blue line represents the simulation results

5.4 Optimisation of the ultrasonic-sonic needle system

As previously discussed in Section 1.5, the effective impulse delivered to the target is used to evaluate the penetration performance of the US needle. To achieve a desired needle penetration performance, the configuration of the needle system is studied to maximise the effective impulse. The mass of the free mass, spring rate and spring pre-load have a

CHAPTER 5

significant influence on the effective impulse, and thus optimisation of the needle system should focus on studying these parameters.

The MSD model of the needle system was employed to carry out a parametric study to select the optimal configuration of the needle system that was also validated by experiment. In this work, a cylindrical free mass was selected as explained in Section 4.3.2 and it was made of titanium alloy Ti-6Al-4V. Three free masses with different masses were selected to investigate the influence to the needle system. The three free masses are shown in Fig. 5.19: a 0.3g free mass with a 3mm length, a 0.48g free mass with a 5mm length and a 0.68g free mass with a 7mm length. The diameter of these free masses was 5.5mm.

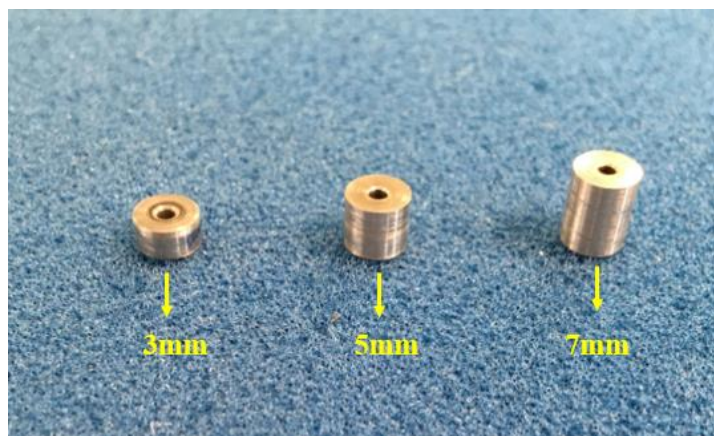


Figure 5.19 Three different free masses used for optimisation of the US needle

The spring effect was studied by two factors: spring rate and spring pre-load. Compression springs (made of stainless steel) were used and three different spring rates were adopted: 1.68N/mm, 2.92N/mm and 4.7N/mm. Five different spring pre-loads were investigated: 7.8N, 9.5N, 11.2N, 12.9N and 14.5N. It was observed from experiment that the needle system was easily stuck during operation when the value of the spring pre-load was more than 25N. In some cases, it was even difficult to start vibration with a larger pre-load because of the strong coupling. On the other hand, the needle system was loose when a low spring pre-load (below 5N) was applied. The disadvantage of this configuration is that the number of impacts between the needle and the target in unit time are limited and the effective impulse delivered to the target is nearly 0. Consequently, the range of the spring pre-load was studied by experiments, and a reasonable range (from 7N to 15N) was selected.

CHAPTER 5

The pre-loads of the three different springs (1.68N/mm, 2.92N/mm and 4.7N/mm) were adjusted to approach the five different pre-loads in each set of experiment, which was achieved by changing the number of spacers to adjust the compressive length of each spring. In the US needle system, the position used to add the spacers was located between the spring and the casing, as shown in Fig. 5.20. The spring rate should have a relatively low value. If a spring with a large rate is adopted, the initial value of the pre-load is large and some intermittent values are neglected. This results in the investigation of the spring pre-load effect on the performance of the needle system being inaccurate. Moreover, if the initial pre-load is larger than a threshold (25N), the US needle will be difficult to vibrate because of the strong coupling. The values of these parameters used in experiment were the same as that used in the numerical model. In experiment and simulation, the ultrasonic transducer-horn operated at the tuned frequency, with the horn tip vibrating at an amplitude of 12 μm .

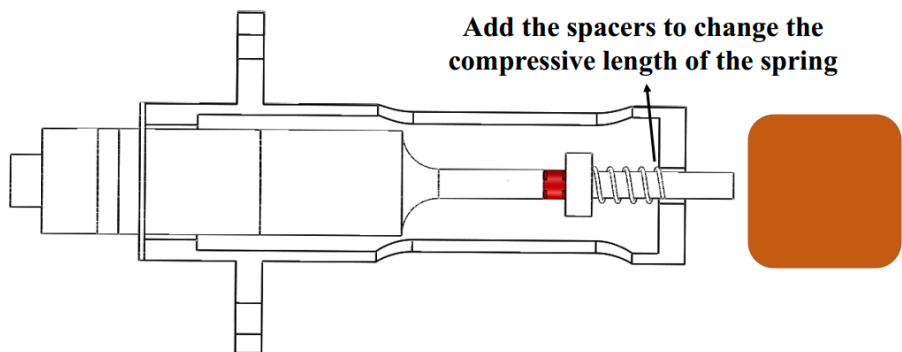


Figure 5.20 The schematic of the US needle system used to indicate the position to add the spacers

Both experiment and simulation were divided into three groups based on the three different spring rates. For each group, one of the three different free masses was first selected and used in experiment and simulation; then the effective impulse was calculated with the values of the spring pre-load varying from 7.8N to 14.5N. This procedure was also carried out on the second and third free masses. The compressive strength of targeted bone was estimated 110MPa, which was used to calculate the effective impulse. The US needle with different configurations were studied by experiment and simulation and the corresponding effective impulse values are shown in Fig. 5.21.

CHAPTER 5

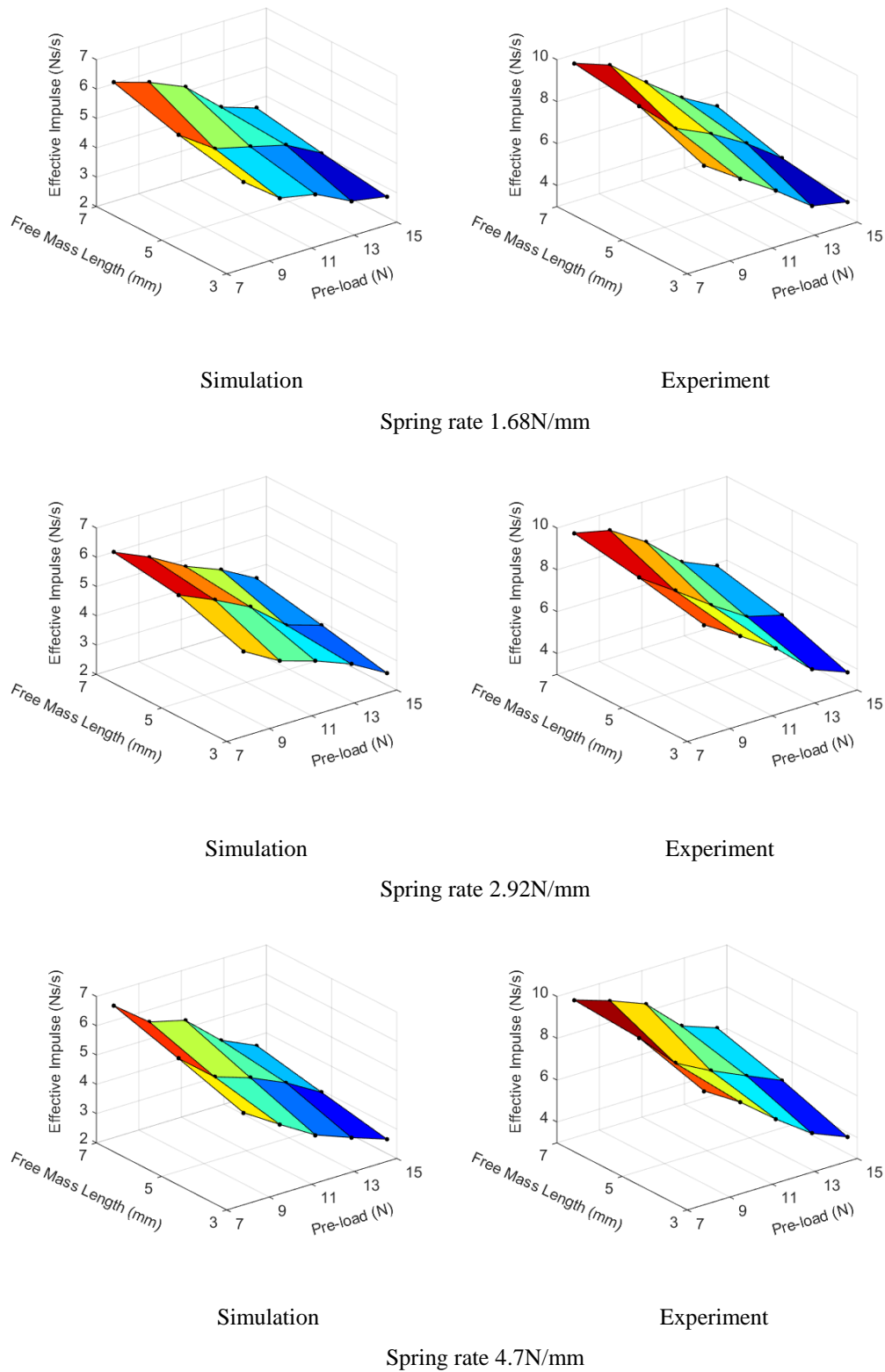


Figure 5.21 The effective impulse values of the US needle with different configurations (simulation and experimental results)

CHAPTER 5

In the experiment, for the three parameters (mass of free mass, spring rate and spring pre-load), the spring pre-load was found to play an important role on the effective impulse delivered to the target. For the spring pre-load ranging from 7N to 15N, both the experimental and simulation results indicate that a large effective impulse can be achieved under conditions where a small spring pre-load is applied to the needle system. Moreover, the effective impulse is decreasing dramatically when the needle system employs a large spring pre-load. A relatively low spring pre-load should be used in the US needle to obtain a large effective impulse.

The mass of the free mass also affects the effective impulse delivered to the target. The simulation results show that increasing the mass of the free mass can improve the effective impulse. This is also proven by the experimental results. In experiment, the needle system was found to be difficult to vibrate if the length of the free mass is longer than 7mm, constructing the free mass to a maximum of 0.68g. The free mass of 0.68g is regarded as the maximum free mass that the ultrasonic transducer-horn designed in this work can drive for the US needle. Thus, the mass of the free mass is selected as 0.68g (7mm length).

The effect of the spring rate on the performance of the needle system can also be evaluated because the spacer is used to change the compressive length of the spring and thus the spring pre-load can be adjusted to the same value for the three springs with different spring rates. For the three different spring rates, both the experimental and simulation results indicate that the spring rate does not have a significant influence on the effective impulse. The differences of the effective impulse are small when spring rates are changing from 1.68N/mm to 4.7N/mm. However, the spring rate is still regarded as an important factor to the US needle. As explained before, a large spring rate results in a high pre-load level, which can reduce the effective impulse and cease the vibration of the needle system. Consequently, it is also necessary to investigate the effect of the spring rate on the performance of the needle system. In this work, the suitable spring rate range of the US needle system is studied by experiment to avoid the needle system stuck, which should be in the range of 1.68N/mm up to 4.7N/mm.

The optimal configuration of the US needle is determined, which aims to deliver the maximum effective impulse to the target and is summarized as follows: a low spring pre-load but more than 5N; 0.68g free mass (7mm length); spring rate ranging from 1.68N/mm

CHAPTER 5

up to 4.7N/mm. This is based on the value of the effective impulse delivered to the target. For this conclusion, the simulation and experimental results are in good agreement.

Case study

Two different configurations of the US needle (US needle 3 and US needle 4) are listed in Table 5.5. They were used to conduct penetration tests to assess the capability of the two needle systems on penetrating cortical bone (strong, hard and high density). US needle 3 was assembled based on the optimal configuration of the needle system. On the other hand, US needle 4 was assembled without a suggested configuration, a small mass of free mass (0.3g) and a large spring pre-load (17.6N). The same spring rate (2.92N/mm) was used for these two needles.

Table 5.5 Two different configurations of the US needles

	US needle 3	US needle 4
Mass of free mass (g)	0.68	0.3
Spring rate (N/mm)	2.92	2.92
Spring pre-load (N)	7.8	17.6

Both the US needle 3 and US needle 4 were used to carry out penetration tests on ovine cortical bone from the central diaphysis of an ovine femur. The same biopsy needle was used for the two US needles, with an outer diameter of 2.83mm and an inner diameter of 1.85mm. The material of the needles were stainless steel. The ultrasonic transducer-horn operated at the tuned frequency. The vibration amplitudes of the horn tip for these two US needles were kept consistent, 12 μ m. The ovine bone was preserved in freezing condition before the test and it was fixed to a bench top vice. For the US needles used for bone penetration, the experimental setup, operation procedure, rate of progress and heat generation around the penetration site will be explained in Chapter 6. The results of the penetration tests are shown in Fig. 5.22.

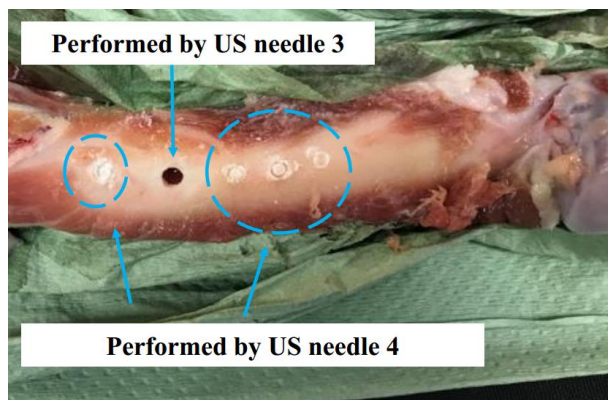


Figure 5.22 Comparison of the penetration performance between US needle 3 and US needle 4

Fig. 5.22 shows the US needle 3 can successfully penetrate the cortical bone. On the other hand, 4 penetration tests are conducted using the US needle 4, and all of the tests shows the US needle 4 failed to penetrate the cortical bone. The thickness of the cortical bone layer is approximately 3mm while the maximum penetration depth of US needle 4 is below 1mm. This is because, as expected, the US needle 4 cannot deliver sufficient effective impulses to the target. Moreover, Fig. 5.23 also shows the needle system failed to penetrate the ovine cortical bone, which is also assembled without a suggested configuration. The optimised prototype US needle system will be used to conduct penetration tests on biomechanical materials and fresh ovine femur (trabecular bone and cortical bone) to investigate the feasibility for use in bone biopsy.

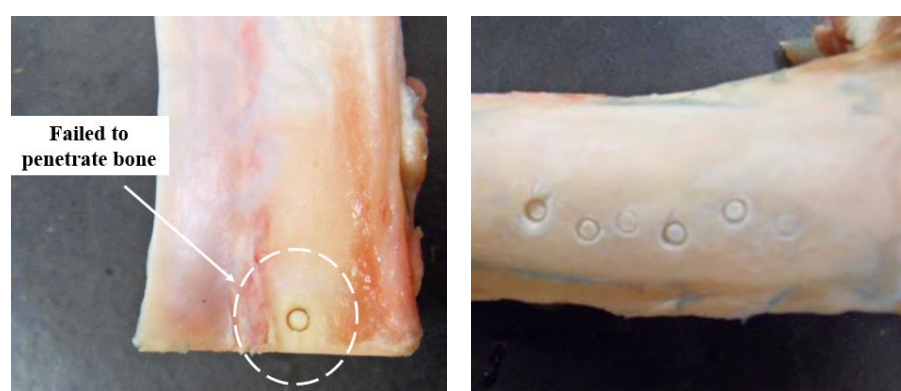


Figure 5.23 Penetration tests on ovine cortical bone using the US needle

5.5 Chapter conclusion

In this chapter, a mathematical model of the US needle was studied and built by the MSD modelling approach and FE method. The MSD model of the needle system was also validated by the experiments and then it was used to optimise the needle system to improve the effective impulse delivered to the target.

The process of modelling of the needle system was presented. Each part of the dynamic stack was modelled as a MSD model, such as the ultrasonic transducer-horn, free mass, surgical needle and target. The MSD model of the ultrasonic transducer-horn was developed by theoretical calculation and experimental method, which was also validated by experiments. The ultrasonic horn-free mass impact model, free mass-surgical needle impact model and needle-target impact model were also investigated, and the parameters of these models (such as contact stiffness, damping coefficient and effective mass) were determined by FE method and experiments of velocities measurements and contact time measurement. The dynamic equations used to describe the motion of the needle system were achieved. The MSD model of the needle system was built in Matlab/Simulink based on these dynamic equations.

The MSD model of the US needle system was validated by experiments before it was used to optimise the needle system. The MSD model was validated by two ways: without the presence of the target and with the target. The velocity of the free mass, the velocity of the needle and the impact force predicted from simulation and measured in experiment were used to validate the MSD model. The simulated impact force was correlated with the measured force in terms of the force magnitude, number of total force peaks and force distribution. The MSD model was further validated by varying the values of the spring pre-load, and the corresponding effective impulses in simulation and experiment were calculated and compared. According to the simulation and experimental results, the numerical model was shown that it can evaluate the performance of the US needle system with reasonable accuracy.

The configuration of the needle system was investigated by the simulation model and experimental method to optimise the US needle system, improve the effective impulse and

CHAPTER 5

achieve the desired needle penetration performance. This was conducted by optimisation of the mass of the free-mass, spring rate and spring pre-load. Both of the experimental and simulation results indicate that an optimal configuration of the needle system should meet the following requirements: spring pre-load in the range of 7N to 10N; 0.68g free mass; spring rate ranging from 1.68N/mm up to 4.7N/mm.

Chapter 6 Penetration tests

Chapters 3 to 5 have studied the optimal configuration of the US needle for bone biopsy, using numerical modelling and experimental methods. The dimensions of the US needle with the optimal configuration are shown in Fig. 6.1. To study the feasibility of applying the ultrasonic-sonic drilling mechanism in a surgical device, the US needle with the optimal configuration was employed to perform penetration tests. It was first used to conduct tests on biomechanical test samples, investigating the needle penetration performance (the capability of penetrating the target and extracting a biopsy sample). Biomechanical materials with three different densities were used in this work to simulate the mechanical properties of human trabecular bone. Then, the US needle was employed to perform penetration tests on the fresh ovine femur, including trabecular bone and cortical bone. The penetration performance of the US needle was evaluated against a conventional trephine needle and an ultrasonic resonant (UR) needle, comparing surface profile of the biopsy site, shape of biopsy sample, rate of progress and heat generation. The temperature around the bone biopsy site was also measured throughout the US needle biopsy procedure.

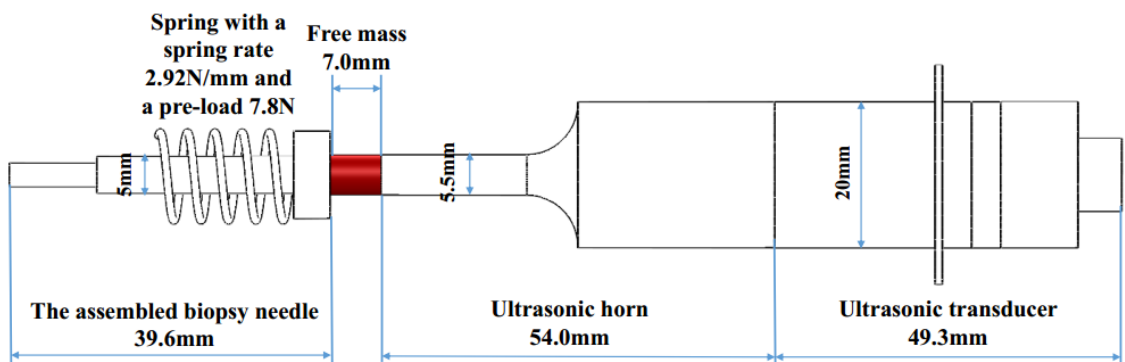


Figure 6.1 The dimensions of the US needle with the optimal configuration (without casing)

6.1 Biopsy needles and testing materials

Biopsy needles

A conventional trephine needle and an US needle, Fig. 6.2, were used to conduct the penetration tests and compare their penetration performance. The trephine needle (introduced in Section 2.2.3) is a conventional surgical instrument and is currently used to perform bone biopsy. Gauge 11 and gauge 8 standard trephine needles were used in this work. The US needle was reassembled based on the optimisation results, which were 0.68g free mass (7mm length), 2.92N/mm spring rate and 7.8N spring pre-load. The inner diameters of the biopsy needles used in the US devices were close to the trephine needles. The dimensions of the trephine and US needles are presented in the following sections.



(a)



(b)

Figure 6.2 Two different bone biopsy needles (a) a conventional trephine needle, 101.00mm length (b) an US needle, 137.80mm length

CHAPTER 6

The penetration performance of the US needle was also compared with an UR needle. Fig. 6.3 shows the UR needle designed by researchers from the Medical and Industrial Ultrasonics Group of the School of Engineering of the University of Glasgow [93]. The UR needle was also designed for bone biopsy. It consists of two components: a half-wavelength Langevin transducer and a half-wavelength resonant needle connected by a threaded joint. The UR needle was tuned to operate at 23.5kHz in the 2nd longitudinal vibration mode, with a length of 122mm, and needle tip inner and outer diameters of 2.84mm and 4mm respectively. It is made of stainless steel 316 and has a flat surface at the needle tip.



Figure 6.3 UR needle designed for bone biopsy, 122mm length [93]

Testing materials

Three different testing samples, Sawbones (Pacific Research Laboratories, Inc.) and the fresh ovine femur (trabecular bone and cortical bone), were used to perform the penetration tests. Sawbones is a biomechanical material, which is solid rigid polyurethane foam with different densities. This biomechanical material offers mechanical properties similar to that of human trabecular bone, created as it was to replace the human bone samples used for testing screw pullout, insertion and tripping torque. The biomechanical material types 1522-01, 1522-03 and 1522-05 were selected to simulate different kinds of trabecular bone used for bone biopsy. The densities of these samples are 0.16g/cm³, 0.32g/cm³ and 0.64g/cm³ and the dimensions of each test sample are 30mm×30mm×5mm. The material properties of the three different biomechanical materials are listed in Table. 6.1.

Bone tissues are generally classified as cortical bone and trabecular bone. Cortical bone lies in the outer layer of the bone, and it is stronger than trabecular bone. The properties of trabecular bone and cortical bone were introduced in Section 2.2.3.

CHAPTER 6

Table 6.1 Material properties of the three types of biomechanical materials

Material type	Density g/cm ³	Compressive		Tensile		Shear	
		Strength (MPa)	Modulus (MPa)	Strength (MPa)	Modulus (MPa)	Strength (MPa)	Modulus (MPa)
1522-01	0.16	2.2	58	2.1	86	1.6	19
1522-03	0.32	8.4	210	5.6	284	4.3	49
1522-05	0.64	31	759	19	1000	11	130

6.2 Penetration tests on biomechanical test sample

The US needle and trephine needle were first used to perform penetration tests on the biomechanical materials. The biomechanical materials were secured in a bench top vice. Both devices were placed perpendicularly to the target during penetration tests. The operation procedures of these two surgical devices are described in Section 6.3.1. Table 6.2 lists the dimensions of both the trephine needle and the biopsy needle used for the US device. The results of the penetration tests are shown in Fig. 6.4.

Table 6.2 Dimensions of the trephine needle and the US needle used for penetration tests on biomechanical samples

	Trephine needle (Gauge 11)	US needle
Length (mm)	101.00	137.80
Outer diameter of biopsy needle (mm)	3.2	2.56
Inner diameter of biopsy needle (mm)	1.95	1.87
Wall thickness of biopsy needle(mm)	0.63	0.345
Material	Stainless steel	Stainless steel
Shape of needle tip	Multi-bevel shaped needle	Multi-bevel shaped needle

CHAPTER 6

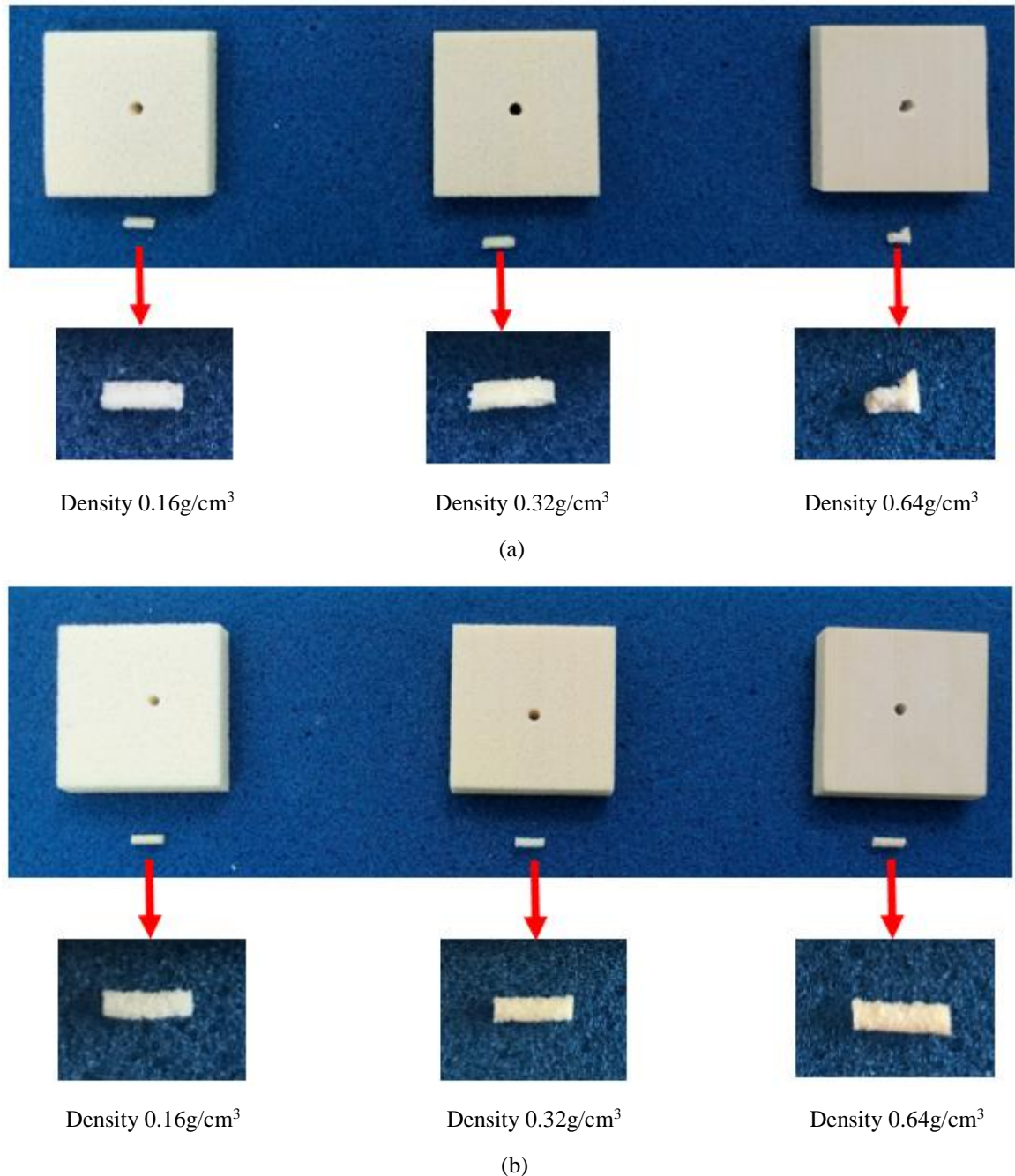


Figure 6.4 Two different bone biopsy needles used to conduct penetration tests on three different biomechanical materials (a) the conventional trephine needle biopsy (b) the US needle biopsy

Both the trephine needle and the US needle successfully penetrated the biomechanical materials and retrieved biopsy samples. For the biomechanical materials with densities 0.16g/cm³ and 0.32g/cm³, the biopsy samples retrieved by the two surgical instruments had the following similar characteristics: 5mm length, regular cylindrical geometry and smooth

CHAPTER 6

surfaces. However, when a denser biomechanical material ($0.64\text{g}/\text{cm}^3$) was used, differences between the two biopsy samples were observed. While the biopsy sample extracted by the US needle maintained its length and shape, the quality of the biopsy sample extracted by the trephine needle decreased, with a sample length of only 4.1mm and irregular geometry. This indicates that the trephine needle gave poor penetration performance on the higher density biomechanical material ($0.64\text{g}/\text{cm}^3$).

The biomechanical material in this work was used to simulate human trabecular bone, which is soft and easily penetrated compared with human cortical bone. Both needles showed excellent rates of progress during penetration of the biomechanical materials, achieving biopsy samples in less than 10 seconds. To penetrate the biomechanical materials, the force applied to the trephine needle was in the order of tens of Newtons, which is acceptable and would not present an excessive challenge to the surgeon using the device. Moreover, during the penetration process, an intermittent repetitive twisting motion was also required for the trephine needle. For the US needle, the force required to penetrate the biomechanical materials was very low (almost zero) and hence it has the ability to extract a high quality biopsy sample without significant deformation.

The UR needle was also used to conduct penetration tests on biomechanical materials. The results show that it could penetrate biomechanical materials and retrieve biopsy samples. The force required to penetrate biomechanical materials for the UR needle was also very low [93]. The heat generated during the penetration process for both the US needle and UR needle was compared.

CHAPTER 6

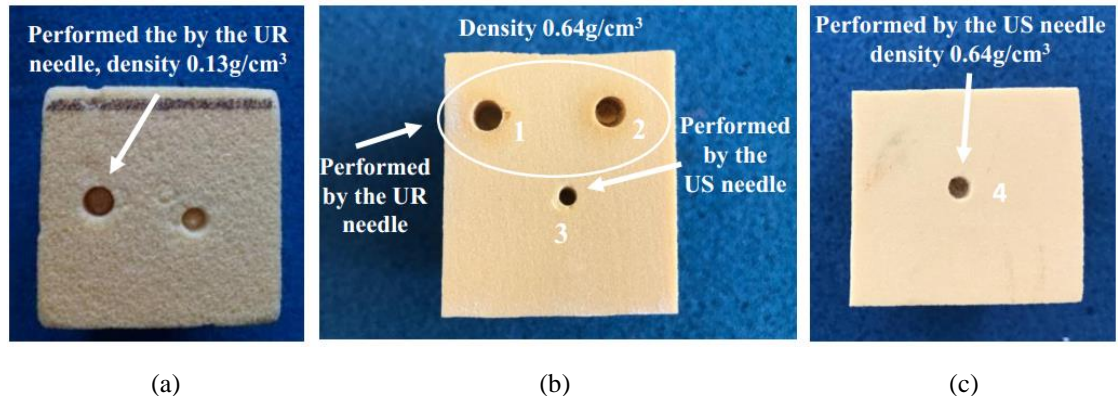


Figure 6.5 The UR needle and the US needle used to perform penetration tests on the biomechanical materials (a) low density testing sample $0.13\text{g}/\text{cm}^3$, thickness 40mm (b) high density testing sample $0.64\text{g}/\text{cm}^3$, thickness 40mm, where Holes 1 and 2 were achieved by the UR needle, Hole 3 was achieved by the US needle (c) high density $0.64\text{g}/\text{cm}^3$ testing sample, thickness 40mm, where Hole 4 was achieved by the US needle

Table 6.3 Dimensions of the penetration holes shown in Fig. 6.5

Hole number	Depth (mm)	Diameter (mm)	Surgical needle type
1	6.65	4.06	UR needle
2	4.23	4.17	UR needle
3	6.34	2.81	US needle
4	6.92	3.34	US needle

Fig. 6.5 shows the results of penetration tests performed by the UR needle and the US needle. Table 6.3 lists the dimensions of the penetration holes. The penetration holes in Fig. 6.5(a) and Fig. 6.5(b) marked numbers 1 and 2 were conducted by the UR needle. In Fig. 6.5(b) and 6.5(c), the penetration holes identified as numbers 3 and 4 were performed by the US needles with two different needle dimensions: one is 2.56mm outer diameter and 1.87mm inner diameter and the other is 3.05mm outer diameter and 2.70mm inner diameter. The densities of the biomechanical materials are $0.13\text{g}/\text{cm}^3$ and $0.64\text{g}/\text{cm}^3$, respectively. For the

CHAPTER 6

penetration tests using the UR needle, there was no sign of burning at the penetration site on the sample with a low density materials (Fig. 6.5(a)). However, on the high density sample (Fig. 6.5(b)), signs of burning were observed. In contrast, there was no sign of burning around the penetration site for the US needle on both materials. These results show that, for the high density material testing, the heat generation produced by the US needle was much less than that of the UR needle. Thus, for penetration of the cortical bone from ovine femur, the US needle may have the advantage of reducing the thermal damage to the bone tissues compared with the UR needle. This will be discussed further in Section 6.3.

6.3 Penetration tests on ovine femur

This section will discuss the penetration tests on the fresh ovine bone (trabecular bone and cortical bone) using the US needle, the trephine needle and the UR needle.

6.3.1 Penetration tests on ovine trabecular bone

The purpose of the test was to retrieve an intact and viable bone biopsy sample for clinical analysis. The structural quality of the biopsy sample was assessed by micro-Computed Tomography (μ CT), which was conducted by the researchers from the Department of Orthopaedics and Trauma of the University of Edinburgh. This technique allows the internal structure of tissue to be assessed non-destructively [158, 159]. An ovine femur was used in this penetration test having been previously preserved by freezing. The ovine femur was fixed to a bench top vice to perform bone biopsy. For the US needle biopsy, the needle system operated at the tuned frequency of 50.58kHz. A very low force was applied to the US needle, which was just used to guide the needle during the biopsy procedure and supply a good contact between the needle and the target. Rotating the device to assist the biopsy process was not required for the US needle. By contrast, the combined application of a large force and an intermittent repetitive twisting action was required for the trephine needle to penetrate bone tissue. The operation procedure of the UR needle was similar to that of the US needle. The UR needle operated at the tuned frequency of 23.50kHz and the operator applied a very low force to conduct bone biopsy. A slow 120° rotation applied by the

CHAPTER 6

operator was required to assist the penetration procedure [93]. Fig. 6.6 shows that the US needle successfully penetrated the trabecular bone.

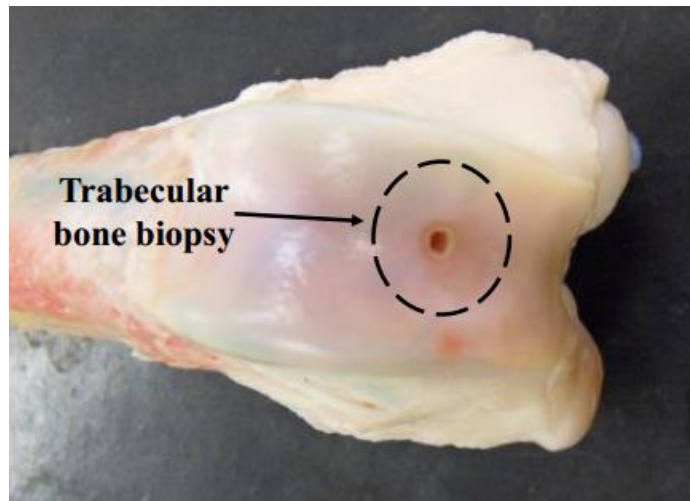
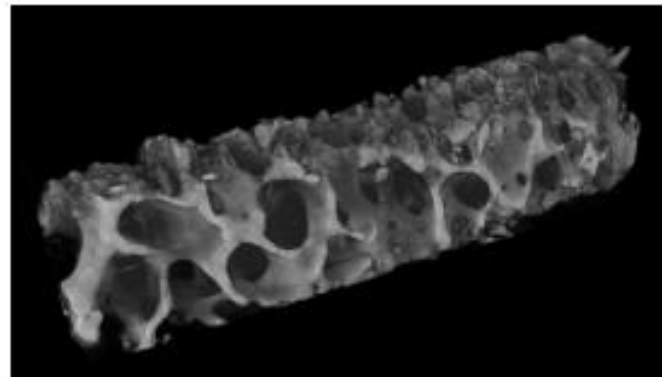
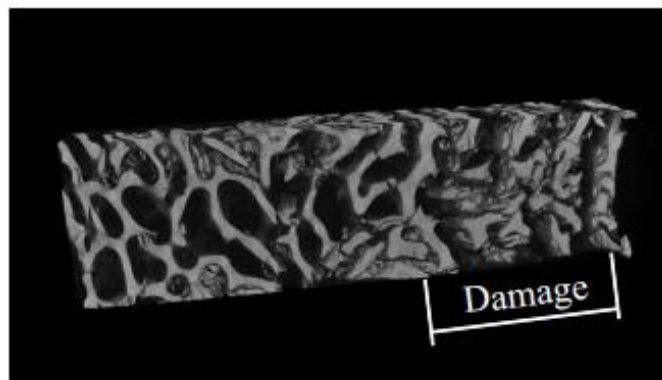


Figure 6.6 A penetration test on ovine femur (trabecular bone) using the US needle

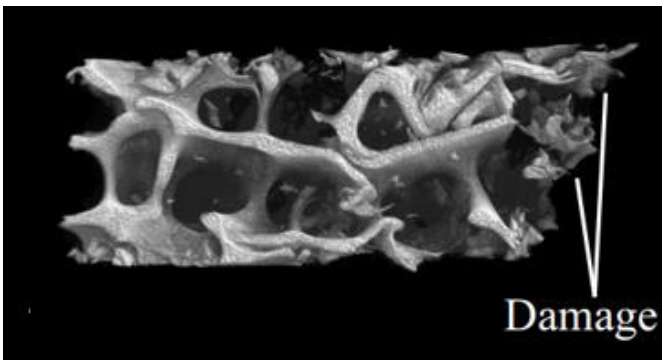
Fig. 6.7 shows a 3D μ CT reconstruction of trabecular bone tissues extracted by the trephine needle, the UR needle and the US needle, respectively [93]. The trephine needle generated the least damage to the bone biopsy sample. It can be seen from Fig. 6.7(b) that damage was produced in one half of the biopsy sample retrieved by the UR needle. In Fig. 6.7(c), damage can be noticed at the right end of the sample. This is because the US needle was pulled out from the biopsy site when the size of the sample retrieved was sufficiently large for further analysis. Thus, the biopsy sample broke away, resulting in damage at the end of the biopsy sample. Nevertheless, the biopsy samples extracted by the US needle and the UR needle were intact and viable. The majority of the samples' micro-architecture remained intact, meaning they would be acceptable for clinical analysis [93]. The penetration tests show that these three needles can extract an intact and viable trabecular bone samples for clinical analysis.



(a)



(b)



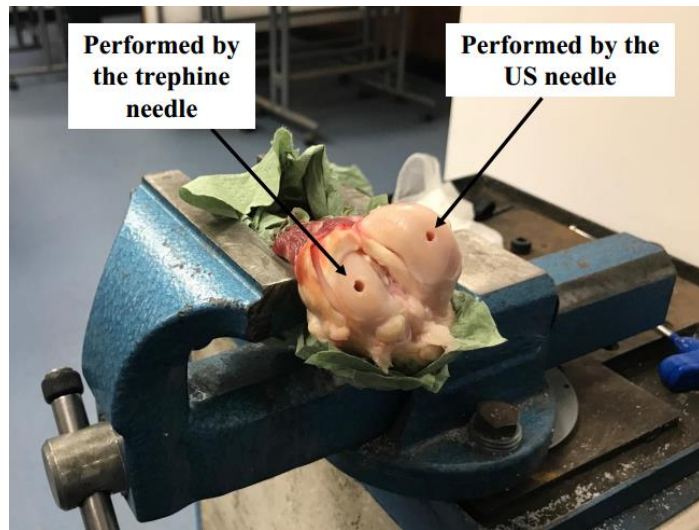
(c)

Figure 6.7 3D µCT reconstruction of trabecular bone biopsy extracted by (a) the trephine needle (b) the UR needle (c) the US needle [93]

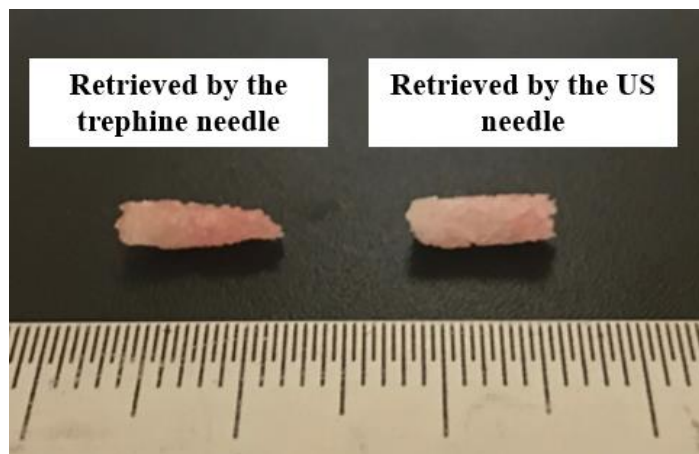
The US needle and the trephine needle were also used to conduct tests on the proximal epiphysis of an ovine femur, as shown in Fig. 6.8. The trabecular bone at this position is denser and harder than the trabecular bone in Fig. 6.6. Both needles successfully penetrated the bone tissue and recovered trabecular bone samples. The quality of the biopsy sample retrieved by the US needle was much better than that retrieved by the trephine needle. In

CHAPTER 6

Fig. 6.8(b), the sample on the left (8.3mm length) was extracted by the trephine needle, which has an irregular shape because of the twisting motion of the needle. On the other hand, the US needle can achieve a regular cylindrical sample (7.6mm length) with a smooth surface.



(a)



(b)

Figure 6.8 Comparison of the US needle biopsy and the trephine needle biopsy (a) Bone penetration tests using the trephine needle and the US needle (b) bone biopsy samples retrieved by the trephine needle and the US needle

CHAPTER 6

6.3.2 Penetration tests on ovine cortical bone

To further evaluate the capability of the US needle, it was used to perform tests on the ovine cortical bone from the central diaphysis of an ovine femur. The cortical bone at this position is the strongest bone in the body. Two different US needles (different dimensions of biopsy needles, US needle 5 and US needle 6) were used to carry out the tests, as shown in Table 6.4. The trephine needles were also used to penetrate cortical bone and were compared with the US needles. Their dimensions are listed in Table 6.4. Trephine needle 2 was machined with a smaller outer diameter (2.93mm) and it was then employed in US needle 5 to deliver a larger effective impulse to the bone. For US needle 6, the biopsy needle was manufactured by the mechanical workshop in the University of Glasgow.

Table 6.4 Dimensions of the trephine needles and the biopsy needles used for US needles

	Trephine needle 1 (Gauge 8)	Trephine needle 2 (Gauge 11)	US needle 5	US needle 6
Needle outer diameter (mm)	4.15	3.20	2.93	3.05
Needle inner diameter (mm)	2.70	1.95	1.95	2.70
Wall thickness (mm)	0.73	0.63	0.49	0.18
Material	Stainless steel	Stainless steel	Stainless steel	Stainless steel

CHAPTER 6

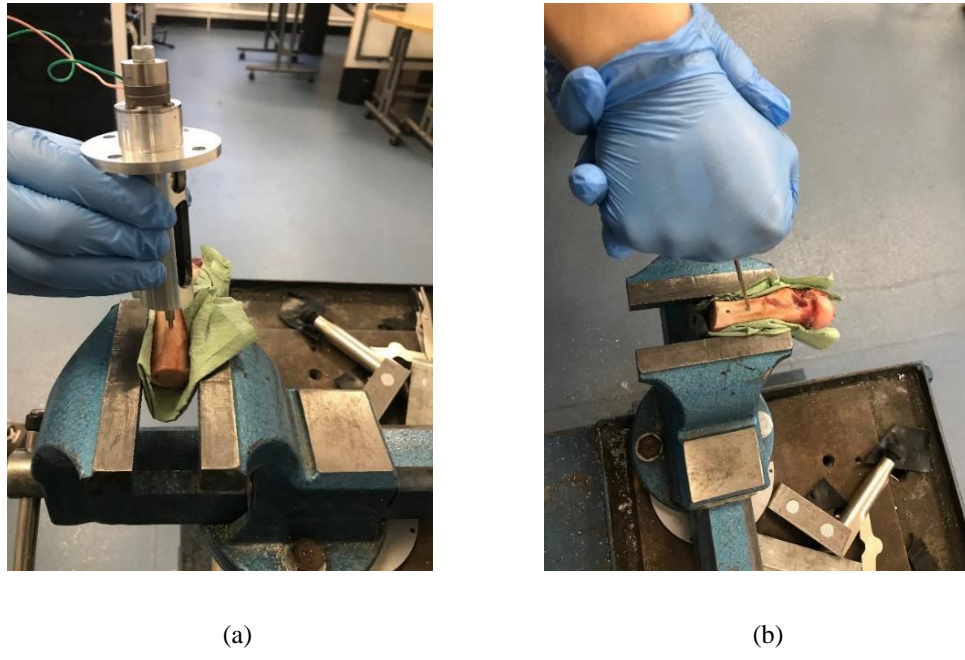


Figure 6.9 Bone biopsy tests (a) US needle biopsy (b) conventional trephine needle biopsy

The testing setups for the US and the trephine needle biopsies can be seen in Fig. 6.9. The ovine femur was fastened to a bench top vice. The operation procedures of the two surgical needles were consistent with the methods used to penetrate trabecular bone. However, the trephine needle required a larger force to penetrate cortical bone compared with that required for trabecular bone. It has been reported that the force applied to the trephine needle to penetrate cortical bone was more than 500N with a twisting motion [93]. Fig. 6.10 shows that trephine needle 1 has acquired a large deformation after use, which indicates a significant force was applied to the needle. For the cortical bone biopsy using the US needle, a very low force applied to the device was required to guide the needle system through the penetration site, similar in magnitude to the force used in penetrating the trabecular bone. US needle 5, US needle 6 and trephine needle 1 successfully penetrated the cortical bone. However, trephine needle 2 failed in this task. The condition of the bone biopsy site and bone biopsy sample are analysed as follows.

CHAPTER 6

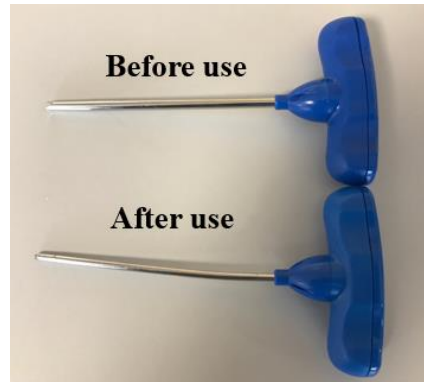


Figure 6.10 Comparison of the trephine needle 1 before and after use

Analysis of the condition of the bone biopsy site

The profiles of the biopsy sites performed by trephine needle 1 and US needle 5 can be seen in Fig. 6.11. By examination of the tissue surrounding the biopsy site, it is evident that the trephine needle induced more damage than the US needle. There was a significant deformation around the biopsy site for trephine needle biopsy, which was caused by the twisting motion of the needle and the large force applied by the operator. The face of the bone biopsy site performed by the US needle was flat and without significant deformation, and the resulting hole regular in shape.

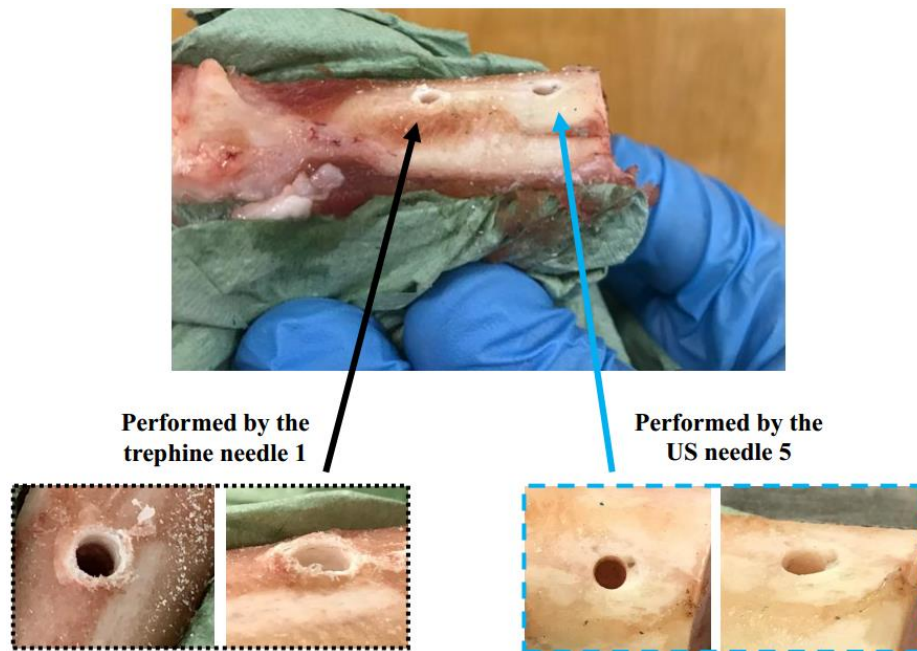


Figure 6.11 Comparison of bone biopsy performance between the trephine needle and the US needle

CHAPTER 6

Analysis of the biopsy sample

The biopsy samples of cortical bone retrieved by US needle 5 and trephine needle 1 are shown in Fig. 6.12. The biopsy sample (2.8mm length, performed by US needle 5) in Fig. 6.12(a) has a regular cylindrical profile and smooth surface. The regular shape of the biopsy sample also indicates that the biopsy site was not subjected to a considerable stress during the biopsy procedure. Some tests of the US needle produced biopsy samples which, whilst maintaining a regular cylindrical profile, were shorter in length than the thickness of the cortical bone layer (approximately 3mm), as shown in Fig. 6.12(b). This could be because the needle was not placed perpendicularly to the target during the US needle biopsy.

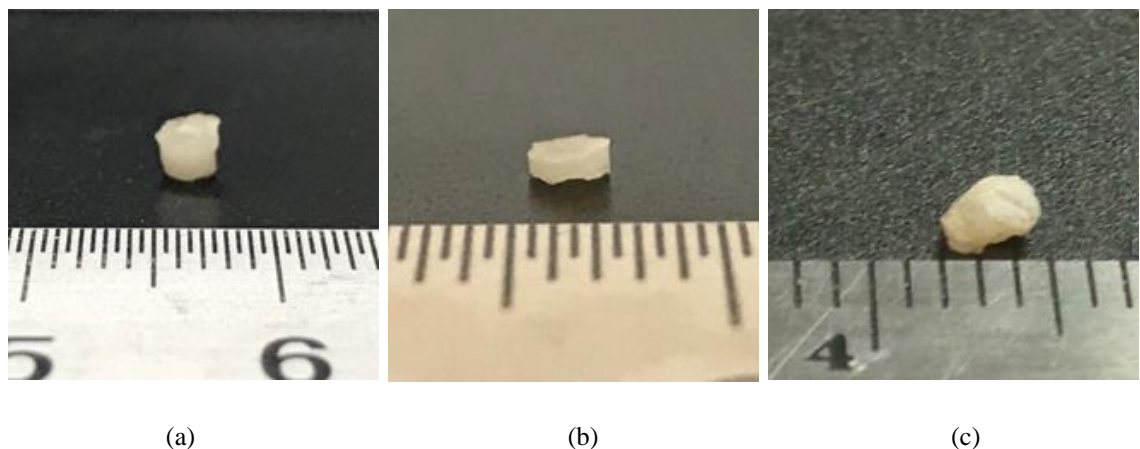


Figure 6.12 Biopsy samples from cortical bone (a) retrieved by the US needle, 2.83mm length (b) retrieved by the US needle, 1.4mm length (c) retrieved by the trephine needle

In this work, trephine needle 1 successfully penetrated cortical bone; however, the biopsy sample was crushed and hence there was no biopsy sample recovered. Fig. 6.12(c) shows the biopsy sample of cortical bone (also from the central diaphysis of an ovine femur) extracted by a surgeon using a conventional trephine needle [93]. It can be observed that the biopsy sample extracted by the trephine needle has a significant deformation, which has a negative influence on the clinical analysis of the sample. This is because of the combined effect of a significant force and a twisting motion applied to the trephine needle to retrieve the biopsy sample. This resulted in the needle penetrating the bone through an irregular path and thus the bone biopsy sample has an irregular shape.

CHAPTER 6

Bone chips around the biopsy site

The bone chips produced during the US needle and trephine needle biopsy processes can be seen in Fig. 6.13. The quantity of bone chips around the biopsy site generated by the US needle biopsy is much smaller than that produced by the trephine needle biopsy. This means the US needle biopsy may reduce the risk of foreign-body-reactions [50].

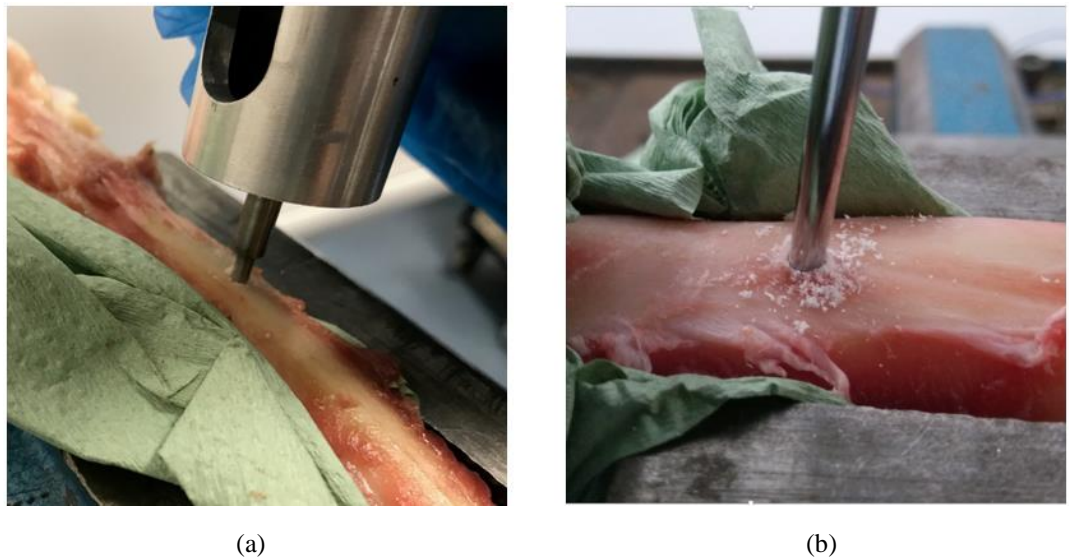


Figure 6.13 Bone chips around the biopsy site (a) US needle biopsy (b) trephine needle biopsy

Needle failure

Fig. 6.14 shows US needle 6 used to conduct bone biopsy on cortical bone. The penetration site was also at the central diaphysis of the ovine femur. US needle 6 penetrated into the cortical bone and extracted a bone biopsy sample. Moreover, it also demonstrated excellent rate of progress: taking 90 seconds to penetrate the cortical bone. This is because the wall thickness of US needle 6 (0.18mm) is small and it can deliver a high pressure to the target during each impact, which can greatly improve the rate of progress. However, the teeth of US needle 6 were broken during the bone biopsy process, as shown in Fig. 6.14(b). Thus, a biopsy needle with a larger wall thickness should be used in the US needle to prevent needle failure.

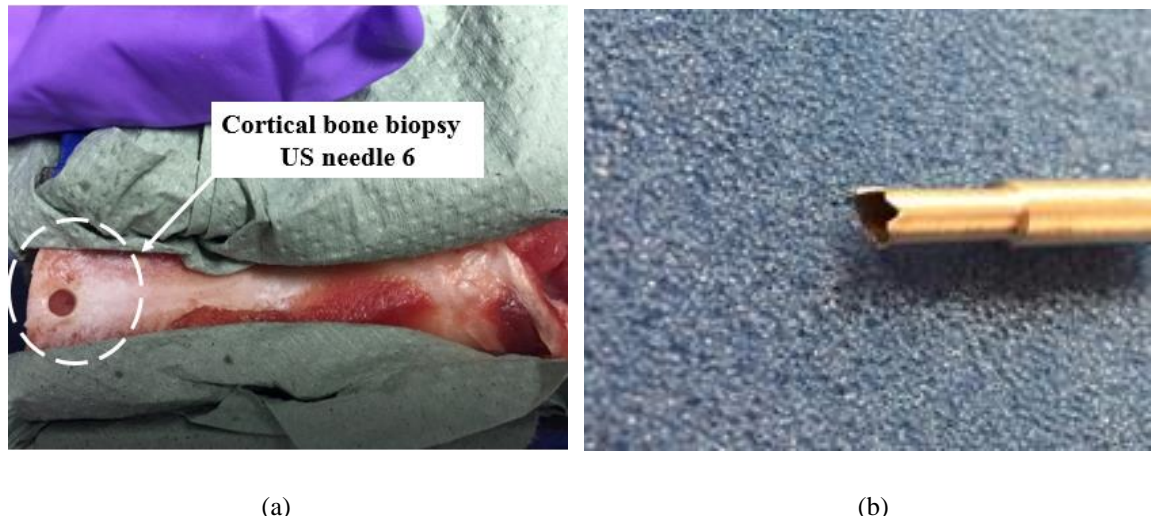


Figure 6.14 US needle biopsy (a) US needle 6 used to conduct cortical bone biopsy (b) needle tip broken during the bone biopsy process

Rate of progress

US needle 5 penetrated the cortical bone from the central diaphysis of an ovine femur and extracted a 2.83mm length biopsy sample within 180 seconds. This was much faster than the UR needle, which obtained a similar length cortical bone sample (also from the central diaphysis of an ovine femur) in 10 minutes. The difference in rate of progress can be ascribed to the differences in drilling mechanisms for the two ultrasonic devices. For the US needle, the ultrasonic transducer-horn resonates at an ultrasonic frequency and the free mass vibrates at sonic frequencies. Compared to the UR needle that directly delivers the impulse to the needle, the transducer-horn of the US needle has sufficient time to recover its vibration amplitude during the interval between two successive impacts and hence transfer a nearly consistent impulse to the free mass and needle for each impact. Thus, the US needle can significantly improve the rate of progress. The trephine needle 1 took 110 seconds to penetrate cortical bone in this work.

Comparison of heat generation between the US and UR needle

A flow of phosphate buffered saline (PBS), which is used to prevent bone tissue heating, is normally applied to the bone cutting procedure using ultrasonic resonant devices [135, 149]. It is reported that the application of PBS was necessary for the bone biopsy procedure (cortical bone from ovine femur) using the UR needle [93]; otherwise, notable burning around the

CHAPTER 6

biopsy site would be produced, indicating serious thermal damage. For the US needle used to perform the cortical bone biopsy, the cooling solution was not applied while there were no obvious signs of burning around the biopsy site, as shown in Fig. 6.11 and 6.14(a). During the US needle biopsy, the temperature around the penetration site was measured and analysed using an infrared thermal camera (FLIR T425).

6.4 Thermal damage analysis of the ultrasonic-sonic needle biopsy

The temperature around the penetration site has a significant influence on bone biopsy as bone cells will become necrotic and irreparable if the temperature increases more than a given threshold. The thermal damage to the bone tissue largely depends on the magnitude of the temperature around the biopsy site and the time that the tissue is subjected to the damaging temperature [160-163]. As explained in Chapter 2, the majority of the researchers believe that a cutting temperature in the range 52°C to 55°C for 30 seconds can induce bone cell death. However, bone can survive higher temperatures (up to 70°C) if the exposure time is very short. As an initial investigation into thermal damage of the bone tissue during US needle 5 biopsy, the temperature around the biopsy site was measured using the infrared thermal camera. The emissivity of a sample material is critical to achieve accurate measurements of the surface temperature of a sample. It represents the efficiency of the material surface in emitting energy through thermal radiation, and the value of emissivity varies from 0 to 1. It was reported that the emissivity of the ovine bone was 0.98, and this value was used in this work [149, 164]. The temperature measurements were conducted on penetration tests on the ovine femur (cortical bone) without cooling solution. The experimental setup was similar to the one shown in Fig. 6.9(a). The fresh ovine bone was fixed to a bench top vice and the infrared thermal camera was employed to record the temperature around the bone biopsy site during the biopsy process. The penetration test was finished in 175 seconds, and a biopsy sample with a length of 3.12mm was extracted. During this bone biopsy process, the maximum temperature around the biopsy site was recorded and is shown in Fig. 6.15.

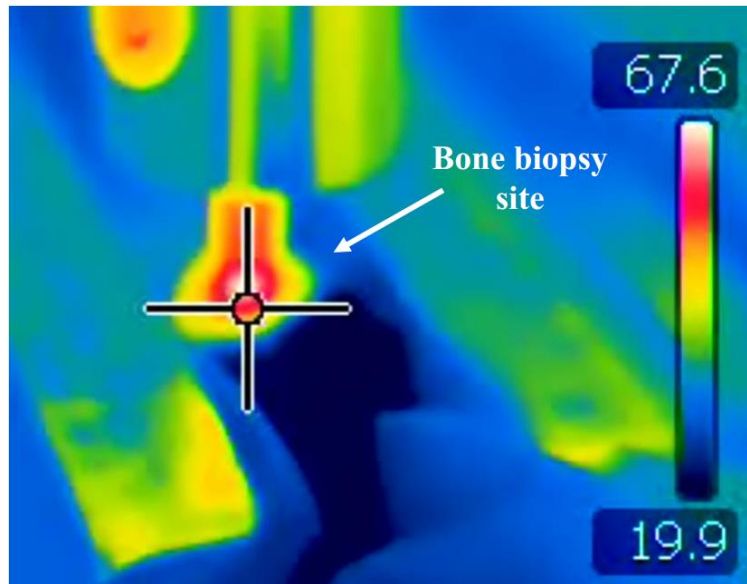


Figure 6.15 Temperature measurement during the bone biopsy procedure

It can be seen that the heat was accumulated at the biopsy site and the maximum temperature around the biopsy site during the bone biopsy process was 67.6°C. Moreover, the temperature (the maximum value of the temperature colour bar) around the biopsy site fluctuated at 63°C and lasted 120 seconds during the process. This temperature value and exposing time can cause irreparable thermal damage to the bone tissue. The bone biopsy site and biopsy sample should be further analysed to investigate the proportion of live cells. The experimental result also suggests the application of PBS is required during the US needle biopsy to reduce heat generation and thermal damage to the bone tissues.

6.5 Chapter conclusion

To study the feasibility of the US needle used in bone biopsy, the US needle with the optimal configuration was used to conduct penetration tests on biomechanical materials and fresh ovine femur (trabecular bone and cortical bone). The penetration performance of the US needle was also compared with the conventional trephine needle and the UR needle. For penetration tests on biomechanical test samples, both the US needle and the trephine needle successfully penetrated the biomechanical materials and extracted bone biopsy samples. The qualities of the biopsy samples extracted by the two needles were virtually identical when the biomechanical materials had a low density. However, for the biomechanical material

CHAPTER 6

with a high density, the quality of the biopsy sample extracted by the trephine needle was worse than that recovered by the US needle, which was less than 5mm length and had irregular geometry. Moreover, the penetration tests also indicated the heat generation produced by the US needle was much less than the UR needle.

The penetration tests were also performed on fresh ovine femur. The trephine needle, the UR needle and the US needle successfully penetrated trabecular bone and extracted biopsy samples. The biopsy samples were analysed with μ CT. The results show that the three needles had extracted an intact and viable trabecular bone sample. For penetration tests on cortical bone, both trephine needle 1 and US needle 5 penetrated the cortical bone; however, there was no biopsy sample retrieved using the trephine needle in this work. An example biopsy sample extracted by the trephine needle was taken from literature and compared with the biopsy sample retrieved by the US needle. The qualities of the bone biopsy site and biopsy sample extracted using the US needle are much better than that recovered by the trephine needle: no significant deformation was observed around the biopsy site and the bone biopsy sample had a more cylindrical geometry and smoother surface. More importantly, the US needle significantly reduced the force required to operate the device. This helps preserve the tissue around the bone biopsy site and ensures a high quality biopsy sample recovered.

The temperature around the biopsy site was measured by an infrared thermal camera during the cortical bone biopsy using US needle 5. The experimental results indicated the temperature around the biopsy site fluctuated at 63°C and lasted 120 seconds during the process. To reduce the thermal damage of the bone tissues, the application of PBS is required for the US needle biopsy procedure. It was also observed from experiments that the heat generation produced by the US needle was much less than the UR needle for the cortical bone biopsy process. This was consistent with the findings from the tests of biomechanical samples.

Chapter 7 Conclusions and future work

7.1 Conclusions

The work presented in this thesis focused on studying the feasibility of the ultrasonic-sonic drilling mechanism applied in a surgical application and design of an ultrasonic surgical device for bone biopsy. An US needle was investigated through the FEM, MSD modelling approach and experimental methods. The configuration of the US needle was also investigated using a MSD model and experimental methods to maximise the effective impulse delivered to the target. The US needle with the optimal configuration (deliver the maximum effective impulse to the target) was assembled and tested in ovine femur *in vitro*. The testing results demonstrated that the needle device extracted a cortical bone biopsy sample with a more cylindrical geometry, smoother surface and more intact sample than a cortical biopsy sample retrieved using a conventional trephine needle. More importantly, the US needle can greatly reduce the force applied to the device, which has the advantages of retrieving a high quality biopsy sample and reducing the trauma to the biopsy site. Although the aim of this study is to design a surgical device for bone biopsy, the methodology and the findings in this thesis can also be used to investigate other ultrasonic applications such as a miniature device for soft tissue drilling or an ultrasonic-sonic blade device.

To build the US needle system, the ultrasonic transducer was first designed by the finite element method based on achievement of high acoustic transmission, low mechanical loss and long lifespan. The ultrasonic horn has an important influence on the momentum of the free mass and hence also affects the effective impulse delivered to the target. The ultrasonic horn was optimised by two factors: the shape and the tip diameter of the horn. Stepped horn, stepped-exponential horn, exponential horn and conical horn shapes were used in this work to investigate the influence on the momentum of the free mass. A FE model of the ultrasonic horn impacting the free mass was developed to evaluate the performance of the horn with different shapes and tip diameters. An optimised configuration of the ultrasonic horn was determined based on the velocity of the free mass after collision. The FE results

CHAPTER 7

demonstrated that a stepped horn with the maximum diameter ratio (3mm horn tip diameter) can transfer the maximum momentum to the free mass. However, the maximum stress in this horn is significantly larger than the fatigue limit of the titanium alloy Ti-6Al-4V. To avoid device failure and transfer a large momentum to the free mass, the stepped horn with 5.5mm tip diameter was used. The ultrasonic transducer and the stepped horn with 5.5mm tip diameter were assembled and modelled in Abaqus to ensure the transducer-horn operates at the tuned frequency of 50kHz with a pure longitudinal mode. The dimensions of the transducer-horn were determined by the FE model and then the transducer-horn was manufactured and assembled. The assembled transducer-horn was analysed by the experimental methods: the electrical impedance analysis and EMA. Electrical impedance analysis and EMA demonstrated close correlation between experimental and simulated results, with less than 2% difference for the resonant frequency of the 2nd longitudinal mode. The US needle system was designed and manufactured based on development of a hand-held device with small size. The components of the US needle were also discussed and determined, such as free mass, spring and biopsy needle.

The numerical model of the US needle was studied and developed by the MSD modelling approach and finite element method, which was used to optimise the needle system to improve the effective impulse delivered to the target. Each component of the US needle was modelled as a MSD model, such as transducer-horn, free mass, biopsy needle and target. The MSD model of the needle system was achieved by assembling each unit of dynamic MSD model and then running in Matlab/Simulink to calculate the impact force delivered to the target. The parameters of the MSD model (such as effective mass, contact stiffness and damping coefficient) were determined by the 3D laser Doppler vibrometry and ultra-high speed camera measurements. The numerical model of the US needle was validated through experimental evaluation. The simulated and measured impact force, the free mass velocity and the needle velocity were used to verify the accuracy of the needle system MSD model. The MSD model was further verified by varying the spring pre-loads and the corresponding effective impulse in simulation and experiment were calculated and compared. The simulation and experimental results demonstrated that the MSD model can be used as a predictive tool to estimate an appropriate configuration of the needle system. The MSD model was also used to perform a parametric study to evaluate the performance of the needle

CHAPTER 7

system with different configurations. The mass of the free mass, spring rate and spring pre-load were optimised by the MSD model, which was also validated by experiments. Both the experimental and simulation results demonstrated the optimal configuration of the needle should meet the following requirements: spring pre-load in the range of 7N to 10N; 0.68g free mass; spring rate ranging from 1.68N/mm up to 4.7N/mm. It was also noted that a large free mass (more than 0.68g) and a large spring pre-load (more than 25N) resulted in the needle system difficult to vibrate.

The US needle was reassembled based on the optimisation results, which was 0.68g free mass (7mm length), 2.92N/mm spring rate and 7.8N spring pre-load. The needle system was used to conduct penetration tests on biomechanical test samples and fresh ovine femur (trabecular bone and cortical bone). The needle system successfully penetrated these targets and extracted biopsy samples with regular cylindrical geometry and smooth surface. For the trephine needle, it could achieve a good quality biopsy sample from trabecular bone; however, the biopsy sample had a significant deformation and even failed to achieve a biopsy sample when the trephine needle was used to penetrate cortical bone. Moreover, the US needle required a much shorter time to penetrate the cortical bone than the UR needle, and generated less heat.

The current research shows that the ultrasonic-sonic drilling mechanism can be used in the surgical field, and the US needle designed in this study can penetrate the strongest bone and achieve a biopsy sample for clinical analysis. Moreover, the US needle biopsy can significantly reduce the trauma to the biopsy site and preserve the surrounding tissues compared with the conventional trephine needle biopsy.

7.2 Future work

The following suggestions are presented for future work.

(1) Reducing the size of the US needle

The US needle successfully penetrates bone tissue and achieves bone samples. However, the size of the needle system may be further reduced by investigation of a half-wavelength

CHAPTER 7

ultrasonic transducer to replace the one-wavelength ultrasonic transducer-horn. Half-wavelength ultrasonic transducers with the operating frequencies 35kHz and 50kHz could be designed and investigated for feasibility. The different size of the US needles may be used in different surgical applications, which provide more choices for the surgeon.

(2) Investigation of the thread fit method used to assemble the needle insertion connector and the biopsy needle

In this work, the method of press fit was used to assemble the needle insertion connector and the biopsy needle. This is because the geometry of the need tip was difficult to manufacture using the existing facilities and hence a commercial biopsy needle was used in the US needle system. The wall thickness of the commercial needle was small and it was difficult to manufacture the threaded part on the needle. The needle device is intended for use in surgical applications. It is necessary to ensure the biopsy needle can be easily replaced for single-use. Thus, the method of thread fit should be used, and the wall thickness of the needle connection end is necessary to investigate to ensure the threaded part at the connection end has sufficient strength to avoid failure.

(3) Applying the rotation motion to the needle to improve the rate of progress

The progress rate of penetrating cortical bone may be further improved if a rotation motion is applied to the US needle. It is recommended to investigate the penetration performance of the US needle with a rotation motion, such as rate of progress, heat generation and the quality of biopsy sample. Rotation motion of the needle could be achieved by a gearing system.

(4) Reducing the heat generation during the US needle biopsy

Controlling the temperature around the biopsy site is critical as bone necrosis occurs in the environment of high temperature 52°C to 55°C for more than 30 seconds. During the US needle biopsy, the maximum temperature around the biopsy site is 67.6°C and it is necessary to investigate methods to reduce the cutting temperature. For example, it can be achieved by improving the rate of progress to reduce the penetration time and hence reduce the heat accumulation.

REFERENCES

Appendix I: References

- [1] S. Malempati , S. Joshi , S. Lai , D. Braner , and K. Tegtmeyer, "Bone marrow aspiration and biopsy," New England Journal of Medicine, vol. 361, no. 15, pp. 182-183, 2009.
- [2] S. G. Leffler and F. S. Chew, "CT-guided percutaneous biopsy of sclerotic bone lesions: diagnostic yield and accuracy," American Journal of Roentgenology, vol. 172, no. 5, pp. 1389-1392, 1999.
- [3] C. Errani, F. Traina, F. Perna, C. Calamelli, and C. Faldini, "Current concepts in the biopsy of musculoskeletal tumors," The Scientific World Journal, vol. 2013, Article ID: 538152, 2013.
- [4] F. Pohlig, C. Kirchhoff, U. Lenze, J. Schauwecker, R. Burgkart, H. Rechl, and R. Von Eisenhartroth, "Percutaneous core needle biopsy versus open biopsy in diagnostics of bone and soft tissue sarcoma: a retrospective study," European Journal of Medical Research, vol. 17, no. 1, pp. 29-34, 2012.
- [5] Y. J. Yang and T. A. Damron, "Comparison of needle core biopsy and fine-needle aspiration for diagnostic accuracy in musculoskeletal lesions," Archives of Pathology and Laboratory Medicine, vol. 128, no. 7, pp. 759-764, 2004.
- [6] WebMD. <http://www.webmd.com/cancer/bone-biopsy-open>, Accessed on 24th October 2016.
- [7] MyHealth.Alberta.ca.
<https://myhealth.alberta.ca/health/aftercareinformation/pages/conditions.aspx?hwid=bo1292>, Accessed on 24th October 2016.
- [8] H. H. Postle, "Ultrasonic cavity preparation," The Journal of Prosthetic Dentistry, vol. 8, no. 1, pp. 153-160, 1958.
- [9] W. Lefkowitz, "Ultrasonics in dentistry," The Journal of the American Dental Association, vol. 52, no. 4, pp. 406-409, 1956.

REFERENCES

- [10] P. Leclercq, C. Zenati, S. Amr, and D. Dohan, "Ultrasonic bone cut part 1: state-of-the-art technologies and common applications," *Journal of Oral and Maxillofacial Surgery*, vol. 66, no. 1, pp. 177-182, 2008.
- [11] T. Vercellotti, "Technological characteristics and clinical indications of piezoelectric bone surgery," *Minerva Stomatol*, vol. 53, no. 5, pp. 207-214, 2004.
- [12] M. Volkov and I. Shepeleva, "The use of ultrasonic instrumentation for the transection and uniting of bone tissue in orthopaedic surgery," *Reconstruction Surgery and Traumatology*, vol. 14, pp. 147-152, 1974.
- [13] J. Beziat, J. Bera, B. Lavandier, and A. Gleizal, "Ultrasonic osteotomy as a new technique in craniomaxillofacial surgery," *International Journal of Oral and Maxillofacial Surgery*, vol. 36, no. 6, pp. 493-500, 2007.
- [14] M. Labanca, F. Azzola, R. Vinci, and L. F. Rodella, "Piezoelectric surgery: twenty years of use," *British Journal of Oral and Maxillofacial Surgery*, vol. 46, no. 4, pp. 265-269, 2008.
- [15] H. Seshan, K. Konuganti, and S. Zope, "Piezosurgery in periodontology and oral implantology," *Journal of Indian Society of Periodontology*, vol. 13, no. 3, pp. 155-156, 2009.
- [16] V. Rajendran, *Engineering Physics*: Tata McGraw-Hill, New Dehli, India, 2009.
- [17] L. L. Beranek and T. Mellow, *Acoustics: Sound Fields and Transducers*: Elsevier, 2012.
- [18] N. Brachet, D. Brown, R. Le Bras, Y. Cansi, P. Mialle, and J. Coyne, "Monitoring the earth's atmosphere with the global IMS infrasound network," *Infrasound Monitoring for Atmospheric Studies*: Springer, pp. 77-118, 2010.
- [19] Z. Der, R. Shumway, and E. Herrin, *Monitoring the comprehensive nuclear-test-ban treaty: data processing and infrasound*: Birkhauser, pp. 911-944, 2002.
- [20] A. Jedrusyna and A. Noga, "A simple acoustic generator for boiler cleaning applications," *Mechatronics 2013*: Springer, pp. 387-392, 2014.
- [21] A. Pichon, E. Blanc, and A. Hauchecorne, *Infrasound Monitoring for Atmospheric Studies*: Springer, Netherlands, pp. 475-506, 2010.

REFERENCES

- [22] G. Harvey, A. Gachagan, and T. Mutasa, "Review of high-power ultrasound-industrial applications and measurement methods," *IEEE Transactions on Ultrasonics, Ferroelectrics, and Frequency Control*, vol. 61, no. 3, pp. 481-495, 2014.
- [23] M. Lucas, A. Cardoni, E. McCulloch, G. Hunter, and A. MacBeath, "Applications of power ultrasonics in engineering," *Applied Mechanics and Materials*, vol. 13-14, pp. 11-20, 2008.
- [24] Q. Zhou, K. Lam, H. Zheng, W. Qiu, and K. Shung, "Piezoelectric single crystal ultrasonic transducers for biomedical applications," *Progress in Materials Science*, vol. 66, pp. 87-111, 2014.
- [25] Y. Chen, H. Chang, Y. Chiang, and C. Lin, "Application and development of ultrasonics in dentistry," *Journal of the Formosan Medical Association*, vol. 112, no. 11, pp. 659-665, 2013.
- [26] Y. Kim and Y. Kwon, "Review of magnetostrictive patch transducers and applications in ultrasonic nondestructive testing of waveguides," *Ultrasonics*, vol. 62, pp. 3-19, 2015.
- [27] B. Sigel, J. C. Coelho, D. P. Flanigan, J. J. Schuler, J. Machi, and J. C. Beitler, "Detection of vascular defects during operation by imaging ultrasound," *Annals of Surgery*, vol. 196, no.4, pp. 473-480, 1982.
- [28] L. Angelini, M. Bezzi, G. Tucci, M. M. Lirici, F. Candiani, L. Rubaltelli, and G. Fegiz, "The ultrasonic detection of insulinomas during surgical exploration of the pancreas," *World Journal of Surgery*, vol. 11, no. 5, pp. 642-647, 1987.
- [29] J. A. Gallego-Juarez, "High-power ultrasonic processing: recent developments and prospective advances," *Physics Procedia*, vol. 3, no. 1, pp. 35-47, 2010.
- [30] S. Fuente-Blanco, E. R. F. De Saravia, V. M. Acosta-Aparicio, A. Blanco-Blanco, and J. A. Gallego-Juárez, "Food drying process by power ultrasound," *Ultrasonics*, vol. 44, pp. 523-527, 2006.
- [31] H. Al-Budairi, M. Lucas, and P. Harkness, "A design approach for longitudinal-torsional ultrasonic transducers," *Sensors and Actuators A: Physical*, vol. 198, pp. 99-106, 2013.

REFERENCES

- [32] Y. Watanabe, Y. Tsuda, and E. Mori, "A longitudinal-flexural complex-mode ultrasonic high-power transducer system with one-dimensional construction," Japanese Journal of Applied Physics, vol. 32, no. 5, pp. 2430-2434, 1993.
- [33] J. Tsujino, R. Suzuki, and M. Takeuchi, "Load characteristics of ultrasonic rotary motor using a longitudinal-torsional vibration converter with diagonal slits. Large torque ultrasonic rotary motor," Ultrasonics, vol. 34, pp. 265-269, 1996.
- [34] S. Lin, "Study on the prestressed sandwich piezoelectric ceramic ultrasonic transducer of torsional-flexural composite vibrational mode," The Journal of the Acoustical Society of America, vol. 112, no. 2, pp. 511-517, 2002.
- [35] A. Carovac, F. Smajlovic, and D. Junuzovic, "Application of ultrasound in medicine," Acta Informatica Medica, vol. 19, no. 3, pp. 168-171, 2011.
- [36] P. N. T. Wells, "The medical applications of ultrasonics," Reports on Progress in Physics, vol. 33, no. 1, pp. 45-99, 1970.
- [37] J. A. Jensen, "Medical ultrasound imaging," Progress in Biophysics and Molecular Biology, vol. 93, no. 1, pp. 153-165, 2007.
- [38] T. J. Mason, "Therapeutic ultrasound an overview," Ultrasonics Sonochemistry, vol. 18, no. 1, pp. 847-852, 2011.
- [39] M. Repacholi, G. Gandolfo, and A. Rindi, Ultrasound: Medical Applications, Biological Effects, and Hazard Potential: Springer, US, 2012.
- [40] K. R. Erikson, F. J. Fry, and J. P. Jones, "Ultrasound in medicine-a review," IEEE Transactions on Sonics and Ultrasonics, vol. 21, no. 3, pp. 144-170, 1974.
- [41] S. Martini, "An overview of ultrasound," Sonocrystallization of Fats: Springer, New York, pp. 7-16, 2013.
- [42] M. Schafer, "Ultrasonic surgical devices and procedures," Power Ultrasonics: Elsevier, pp. 633-660, 2015.
- [43] P. Harkness, M. Lucas, A. Mathieson, and C. Murray, "Optimization of ultrasonic horns for momentum transfer and survivability in high-frequency/low frequency planetary drill tools," AIAA SPACE 2011 Conference and Exposition, pp. 27-29, 2011.

REFERENCES

- [44] R. K. Pandey and S. S. Panda, "Drilling of bone: A comprehensive review," *Journal of Clinical Orthopaedics and Trauma*, vol. 4, no. 1, pp. 15-30, 2013.
- [45] G. Augustin, T. Zigman, S. Davila, T. Udilljak, T. Staroveski, D. Brezak, and S. Babic, "Cortical bone drilling and thermal osteonecrosis," *Clinical Biomechanics*, vol. 27, no. 4, pp. 313-325, 2012.
- [46] K. Alam, I. M. Bahadur, and N. Ahmed, "Cortical bone drilling: An experimental and numerical study," *Technology and Health Care*, vol. 23, no. 2, pp. 1-12, 2014.
- [47] M. Louredo, I. Díaz, and J. J. Gil, "DRIBON: A mechatronic bone drilling tool," *Mechatronics*, vol. 22, no. 8, pp. 1060-1066, 2012.
- [48] P. N. Brett, D. A. Baker, L. Reyes, and J. Blanshard, "An automatic technique for micro-drilling a stapedotomy in the flexible stapes footplate," *Proceedings of the Institution of Mechanical Engineers, Part H: Journal of Engineering in Medicine*, vol. 209, no. 4, pp. 255-262, 1995.
- [49] M. B. Abouzgia and D. F. James, "Measurements of shaft speed while drilling through bone," *Journal of Oral and Maxillofacial Surgery*, vol. 53, no. 11, pp. 1308-1315, 1995.
- [50] Y. Eshet, R. R. Mann, A. Anatot, T. Yacoby, A. Gefen, and E. Jerby, "Microwave drilling of bones," *IEEE Transactions on Biomedical Engineering*, vol. 53, no. 6, pp. 1174-1182, 2006.
- [51] S. Chiba, K. Okada, K. Lee, G. V. Segre, and R. M. Neer, "Molecular analysis of defect healing in rat diaphyseal bone," *Journal of Veterinary Medical Science*, vol. 63, no. 8, pp. 603-608, 2001.
- [52] J. T. Payne, G. M. Peavy, L. Reinisch, and D. C. Van Sickle, "Cortical bone healing following laser osteotomy using 6.1 μ m wavelength," *Lasers in Surgery Medicine*, vol. 29, no. 1, pp. 38-43, 2001.
- [53] M. R. Callstrom, J. W. Charboneau, M. P. Goetz, J. Rubin, G. Y. Wong, J. A. Sloan, et al., "Painful metastases involving bone: feasibility of percutaneous CT- and US-guided radio-frequency ablation," *Radiology*, vol. 224, no. 1, pp. 87-97, 2002.

REFERENCES

- [54] I. Ghanem, L. M. Collet, K. Kharrat, E. Samaha, H. Deramon, P. Mertl, et al., "Percutaneous radiofrequency coagulation of osteoid osteoma in children and adolescents," *Journal of Pediatric Orthopaedics B*, vol. 12, no. 4, pp. 244-252, 2003.
- [55] B. S. Yilbas, Z. Yilbas, and M. Sami, "Thermal processes taking place in the bone during CO₂ laser irradiation," *Optics & Laser Technology*, vol. 28, no. 7, pp. 513-519, 1996.
- [56] S. Sherrit, X. Bao, Z. Chang, B. P. Dolgin, Y. Bar-Cohen, D. Pal, et al., "Modeling of the ultrasonic/sonic driller/corer: USDC," *IEEE Ultrasonics Symposium Proceedings*, vol. 1, pp. 691-694, 2000.
- [57] X. Bao, Y. Bar-Cohen, Z. Chang, B. P. Dolgin, S. Sherrit, D. S. Pal, et al., "Modeling and computer simulation of ultrasonic/sonic driller/corer (USDC)," *IEEE Transactions on Ultrasonics, Ferroelectrics, and Frequency Control*, vol. 50, no. 9, pp. 1147-1160, 2003.
- [58] P. Harkness, M. Lucas, and A. Cardoni, "Maximization of the effective impulse delivered by a high-frequency/low-frequency planetary drill tool," *IEEE Transactions on Ultrasonics, Ferroelectrics, and Frequency Control*, vol. 58, no. 11, pp. 2387-2396, 2011.
- [59] P. Harkness and M. Lucas, "A brief overview of space applications for ultrasonics," *Ultrasonics*, vol. 52, no. 8, pp. 975-979, 2012.
- [60] P. G. Newman and G. S. Rozycski, "The history of ultrasound," *Surgical Clinics of North America*, vol. 78, no. 2, pp. 179-195, 1998.
- [61] W. P. Mason, *Physical Acoustics V15: Principles and Methods*: Elsevier Science, pp.102-110, 2012.
- [62] K. Worden, W. A. Bullough, and J. Haywood, *Smart Technologies*: World Scientific, pp. 40-63, 2003.
- [63] N. Waingankar, E. Goldenberg, and B. R. Gilbert, "History of ultrasound," *Ultrasound of the Male Genitalia*: Springer, New York, pp. 1-9, 2015.
- [64] J. Krautkrämer and H. Krautkrämer, *Ultrasonic Testing of Materials*: Springer, pp. 7-36, 1983.

REFERENCES

- [65] S. V. Sancheti and P. R. Gogate, "A review of engineering aspects of intensification of chemical synthesis using ultrasound," *Ultrasonics Sonochemistry*, vol. 36, pp. 527-543, 2017.
- [66] G. T. Clement and K. Hynynen, "A non-invasive method for focusing ultrasound through the human skull," *Physics in Medicine & Biology*, vol. 47, no. 8, pp. 1219-1236, 2002.
- [67] J. D. N. Cheeke, *Fundamentals and Applications of Ultrasonic Waves*: CRC Press, 2010.
- [68] J. Blitz and G. Simpson, *Ultrasonic Methods of Non-destructive Testing*: Springer, Netherlands, 1995.
- [69] T. L. Szabo, *Diagnostic Ultrasound Imaging: Inside Out*: Elsevier, pp. 52-68, 2004.
- [70] A. Criniti and P. C. Lin, "Applications of intraoperative ultrasound in gynecological surgery," *Current Opinion Obstetrics Gynecology*, vol. 17, no. 4, pp. 339-342, 2005.
- [71] D. S. Leonard and C. Timon, "Evaluation of the ultracision ultrasonic dissector in head and neck surgery," *Operative Techniques in Otolaryngology-Head and Neck Surgery*, vol. 19, no. 1, pp. 59-66, 2008.
- [72] T. Bensaha, "A new approach for the surgical exposure of impacted canines by ultrasonic surgery through soft tissue," *International Journal of Oral and Maxillofacial Surgery*, vol. 42, no. 12, pp. 1557-1561, 2013.
- [73] P. A. Lindstrom, "Prefrontal ultrasonic irradiation—a substitute for lobotomy," *A.M.A. Archives of Neurology & Psychiatry*, vol. 72, no. 4, pp. 399-425, 1954.
- [74] W. J. Fry, "Intense ultrasound in investigations of the central nervous system," *Advances in Biological Medical Physics*, vol. 6, no. 4, pp. 281-348, 1958.
- [75] M. Brock, I. Ingwersen, and W. Roggendorf, "Ultrasonic aspiration in neurosurgery," *Neurosurgical Review*, vol. 7, no. 2, pp. 173-177, 1984.
- [76] R. Ramamurti, *Textbooks of Operative Neurosurgery (2 Vol.)*: B.I. Publications Pvt, pp. 55-59, 2005.

REFERENCES

- [77] H. Tang, H. Zhang, Q. Xie, Y. Gong, M. Zheng, D. Wang, et al., "Application of CUSA Excel ultrasonic aspiration system in resection of skull base meningiomas," *Chinese Journal of Cancer Research*, vol. 26, no. 6, pp. 653-657, 2014.
- [78] J. A. James, "New developments in the ultrasonic therapy of Meniere's disease," *Annals of The Royal College of Surgeons of England*, vol. 33, no. 4, pp. 226-244, 1963.
- [79] W. L. Nyborg, "Biological effects of ultrasound: development of safety guidelines. Part II: General review," *Ultrasound in Medicine and Biology*, vol. 27, no. 3, pp. 301-333, 2001.
- [80] G. Osterhoff, E. F. Morgan, S. J. Shefelbine, L. Karim, L. M. McNamara, and P. Augat, "Bone mechanical properties and changes with osteoporosis," *Injury*, vol. 47, pp. S11-S20, 2016.
- [81] S. Li, Cutting of cortical bone tissue: analysis of deformation and fracture process, PhD thesis, Loughborough University, UK, 2013.
- [82] B. Clarke, "Normal bone anatomy and physiology," *Clinical Journal of the American Society of Nephrology*, vol. 3, pp. S131-S139, 2008.
- [83] R. B. Ashman, S. C. Cowin, W. C. V. Buskirk, and J. C. Rice, "A continuous wave technique for the measurement of the elastic properties of cortical bone," *Journal of Biomechanics*, vol. 17, no. 5, pp. 349-361, 1984.
- [84] M. T. Hillery and I. Shuaib, "Temperature effects in the drilling of human and bovine bone," *Journal of Materials Processing Technology*, vol. 92, pp. 302-308, 1999.
- [85] M. B. Abouzgia and D. F. James, "Temperature rise during drilling through bone," *International Journal of Oral Maxillofacial Implants*, vol. 12, no. 3, pp. 342-353, 1997.
- [86] L. S. Matthews and C. Hirsch, "Temperatures measured in human cortical bone when drilling," *The Journal of Bone and Joint Surgery*, vol. 54, no. 2, pp. 297-308, 1972.
- [87] D. L. Brisman, "The effect of speed, pressure, and time on bone temperature during the drilling of implant sites," *International Oral and Maxillofacial Implants*, vol. 11, no. 1, pp. 35-37, 1996.

REFERENCES

- [88] M. B. Abouzgia and J. M. Symington, "Effect of drill speed on bone temperature," International Oral and Maxillofacial Implants, vol. 25, no. 5, pp. 394-399, 1996.
- [89] M. Lucas and A. Mathieson, "Ultrasonic cutting for surgical applications," in Power Ultrasonics, ed Oxford: Woodhead Publishing, pp. 695-721, 2015.
- [90] B. S. Khambay and A. D. Walmsley, "Investigations into the use of an ultrasonic chisel to cut bone. Part 2: cutting ability," Journal of Dentistry, vol. 28, no. 1, pp. 39-44, 2000.
- [91] P. Hennet, "Piezoelectric Bone Surgery: a review of the literature and potential applications in veterinary oromaxillofacial surgery," Frontiers in Veterinary Science, vol. 2, pp. 2-8, 2015.
- [92] A. MacBeath, Ultrasonic bone cutting, PhD thesis, University of Glasgow, UK, 2006.
- [93] A. Mathieson, R. Wallace, R. Cleary, L. Li, H. Simpson, and M. Lucas, "Ultrasonic needles for bone biopsy," IEEE Transactions on Ultrasonics, Ferroelectrics, and Frequency Control, vol. 64, no. 1, pp. 433-440, 2017.
- [94] S. Harder, S. Wolfart, C. Mehl, and M. Kern, "Performance of ultrasonic devices for bone surgery and associated intraosseous temperature development," International Oral and Maxillofacial Implants, vol. 24, no. 3, pp. 484-490, 2009.
- [95] E. A. Al-Moraissi, Y. A. Elmansi, Y. A. Al-Sharaee, A. E. Alrmali, and A. S. Alkhutari, "Does the piezoelectric surgical technique produce fewer postoperative sequelae after lower third molar surgery than conventional rotary instruments? A systematic review and meta analysis," International Journal of Oral and Maxillofacial Surgery, vol. 45, no. 3, pp. 383-391, 2016.
- [96] G. Spinelli, D. Lazzeri, M. Conti, T. Agostini, and G. Mannelli, "Comparison of piezosurgery and traditional saw in bimaxillary orthognathic surgery," Journal of Cranio-Maxillo-Facial Surgery, vol. 42, no. 7, pp. 1211-1220, 2014.
- [97] S. Schaeren, C. Jaquiéry, M. Heberer, M. Tolnay, T. Vercellotti, and I. Martin, "Assessment of nerve damage using a novel ultrasonic device for bone cutting," Journal of Oral and Maxillofacial Surgery, vol. 66, no. 3, pp. 593-596, 2008.

REFERENCES

- [98] D. Parmar, M. Mann, A. D. Walmsley, and S. C. Lea, "Cutting characteristics of ultrasonic surgical instruments," *Clinical Oral Implants Research*, vol. 22, no. 12, pp. 1385-1390, 2011.
- [99] D. Zerbino, "Biopsy: its history, current and future outlook," *Likars' ka sprava/Ministerstvo okhorony zedorov'ia Ukrayny*, pp. 1-9, 1993.
- [100] C. J. Den Heeten, J. Oldhoff, J. W. Oosterhuis, and H. Schraffordt Koops, "Biopsy of bone tumours," *Journal of Surgical Oncology*, vol. 28, no. 1, pp. 247-251, 1985.
- [101] F. Schajowicz, *Tumors and Tumorlike Lesions of Bone and Joints*: Springer, pp. 29-60, 2012.
- [102] M. J. S. Maciel, C. J. Tyng, P. N. V. P. Barbosa, A. G. V. Bitencourt, Junior, Matushita, J. P. KawaoKa, C. E. Zurstrassen, et al., "Computed tomography-guided percutaneous biopsy of bone lesions: rate of diagnostic success and complications," *Radiologia Brasileira*, vol. 47, no. 5, pp. 269-274, 2014.
- [103] J. A. Welker, R. M. Henshaw, J. Jelinek, B. M. Shmookler, and M. M. Malawer, "The percutaneous needle biopsy is safe and recommended in the diagnosis of musculoskeletal masses," *Cancer*, vol. 89, no. 12, pp. 2677-2686, 2000.
- [104] A. Puri, V. U. Shingade, M. G. Agarwal, C. Anchan, S. Juvekar, S. Desai, and N. A. Jambhekar, "CT-guided percutaneous core needle biopsy in deep seated musculoskeletal lesions: a prospective study of 128 case," *Skeletal Radiology*, vol. 35, no. 3, pp. 138-143, 2006.
- [105] S. Kasraeian, D. C. Allison, E. R. Ahlmann, A. N. Fedenko, and L. R. Menendez, "A comparison of fine-needle aspiration, core biopsy, and surgical biopsy in the diagnosis of extremity soft tissue masses," *Clinical Orthopaedics and Related Research*, vol. 468, no. 11, pp. 2992-3002, 2010.
- [106] W. G. Ward, P. Savage, C. A. Boles, and S. E. Kilpatrick, "Fine-needle aspiration biopsy of sarcomas and related tumors," *Cancer Control*, vol. 8, no. 3, pp. 232-238, 2001.
- [107] T. Valebjørg, B. Spahic, F. Bremtun, J. Kahrs, J. Hammerstrom, R. Brudevold, J. Kolflaath, and W. Ghanima, "Pain and bleeding associated with trephine biopsy," *European Journal of Haematology*, vol. 93, no. 4, pp. 267-272, 2014.

REFERENCES

- [108] M. F. Dillon, A. D. K. Hill, C. M. Quinn, A. O'Doherty, E. W. McDermott, and N. O'Higgins, "The accuracy of ultrasound, stereotactic, and clinical core biopsies in the diagnosis of breast cancer, with an analysis of false-negative cases," *Annals of Surgery*, vol. 242, no. 5, pp. 701-707, 2005.
- [109] Y. Bar-Cohen, S. Sherrit, B. P. Dolgin, D. Pal, T. Peterson, R. Kroh, et al., "Ultrasonic/sonic drilling/coring (USDC) for in-situ planetary applications," *Proceedings SPIE*, vol. 3992, pp. 661-668 2000.
- [110] M. Badescu, A. Ressa, Y. Bar-Cohen, S. Sherrit, K. Zacny, G. L. Paulsen, L. Beegle, and X. Bao, "Auto-Gopher: a wireline deep sampler driven by piezoelectric percussive actuator and EM rotary motor," *Proceedings SPIE*, pp. 8692-8696, 2013.
- [111] Y. Bar-Cohen, S. Sherrit, B. P. Dolgin, N. Bridges, X. Bao, Z. Chang, A. Yen, R. S. Saunders, D. Pal, J. Droh, and T. Peterson, "Ultrasonic/sonic driller/corer (USDC) as a sampler for planetary exploration," *IEEE Ultrasonics Symposium Proceedings*, vol. 1, no. 1, pp. 263-271, 2001.
- [112] C. Potthast, J. Twiefel, and J. Wallaschek, "Modelling approaches for an ultrasonic percussion drill," *Journal of Sound and Vibration*, vol. 308, no. 3, pp. 405-417, 2007.
- [113] N. N. Abboud, G. L. Wojcik, D. K. Vaughan, J. Mould, D. J. Powell, and L. Nikodym, "Finite element modelling for ultrasonic transducers," *Ultrasonic Transducer Engineering Conference*, pp. 19-42, 1998.
- [114] S. Lin, "Optimization of the performance of the sandwich piezoelectric ultrasonic transducer," *The Journal of the Acoustical Society of America*, vol. 115, no. 1, pp. 182-186, 2004.
- [115] S. W. Or, H. W. Chan, V. C. Lo, and C. W. Yuen, "Dynamics of an ultrasonic transducer used for wire bonding," *IEEE Transactions Ultrasonics, Ferroelectrics, and Frequency Control*, vol. 45, no. 6, pp. 1453-1460, 1998.
- [116] M. Wilm, A. Reinhardt, V. Laude, R. Armati, W. Daniau, and S. Ballandras, "Three-dimensional modelling of micromachined-ultrasonic-transducer arrays operating in water," *Ultrasonics*, vol. 43, no. 6, pp. 457-465, 2005.
- [117] S. Lin, "Study on the multifrequency Langevin ultrasonic transducer," *Ultrasonics*, vol. 33, no. 6, pp. 445-448, 1995.

REFERENCES

- [118] T. Nishimura, H. Hosaka, and T. Morita, "Resonant-type Smooth Impact Drive Mechanism (SIDM) actuator using a bolt-clamped Langevin transducer," *Ultrasonics*, vol. 52, no. 1, pp. 75-80, 2012.
- [119] J. A. Gallego-Juárez, G. Rodriguez, V. Acosta, and E. Riera, "Power ultrasonic transducers with extensive radiators for industrial processing," *Ultrasonics Sonochemistry*, vol. 17, no. 6, pp. 953-964, 2010.
- [120] B. Fu, T. Hemsel, and J. Wallaschek, "Piezoelectric transducer design via multiobjective optimization," *Ultrasonics*, vol. 44, no. 4, pp. 747-752, 2006.
- [121] B. J. O'Daly, E. Morris, G. P. Gavin, J. M. O'Byrne, and G. B. McGuinness, "High-power low-frequency ultrasound: A review of tissue dissection and ablation in medicine and surgery," *Journal of Materials Processing Technology*, vol. 200, no. 1, pp. 38-58, 2008.
- [122] H. D. Al-Budairi, Design and analysis of ultrasonic horns operating in longitudinal and torsional vibration, PhD thesis, University of Glasgow, UK, 2012.
- [123] S. Lin, "Study on the Langevin piezoelectric ceramic ultrasonic transducer of longitudinal–flexural composite vibrational mode," *Ultrasonics*, vol. 44, no. 1, pp. 109-114, 2006.
- [124] G. Zhou, Y. Zhang, and B. Zhang, "The complex-mode vibration of ultrasonic vibration systems," *Ultrasonics*, vol. 40, no. 1, pp. 907-911, 2002.
- [125] C. Yang, X. Shan, and T. Xie, "A new piezoelectric ceramic longitudinal–torsional composite ultrasonic vibrator for wire drawing," *Ceramics International*, vol. 41, pp. 625-630, 2015.
- [126] Y. Yi, W. Seemann, R. Gausmann, and J. Zhong, "Development and analysis of a longitudinal and torsional type ultrasonic motor with two stators," *Ultrasonics*, vol. 43, no. 8, pp. 629-634, 2005.
- [127] T. Asami and H. Miura, "Study of ultrasonic machining by longitudinal-torsional vibration for processing brittle materials-observation of machining marks," *Physics Procedia*, vol. 70, pp. 118-121, 2015.

REFERENCES

- [128] E. A. Neppiras, "The pre-stressed piezoelectric sandwich transducer," Ultrasonics International 1973 Conferences Proceedings, pp. 295-302, 1973.
- [129] H. J. Lee, S. Zhang, Y. Bar-Cohen, and S. Sherrit, "High temperature, high power piezoelectric composite transducers," Sensors, vol. 14, no. 8, pp. 14526-14552, 2014.
- [130] J. Awrejcewicz, K. J. Kaliński, R. Szewczyk, and M. Kaliczyńska, Mechatronics: Ideas, Challenges, Solutions and Applications: Springer International Publishing, 2016.
- [131] C. E. Limited., Piezoelectric Ceramics, <http://www.celindia.co.in/drupal7/?q=node/47>, Accessed on June 2016.
- [132] CeramTec., Advanced Ceramic Materials for Piezo Applications, <https://www.ceramtec.com/ceramic-materials/piezo-ceramics/sonox-p/>, Accessed on June 2016.
- [133] K. Lweesy, L. Fraiwan, A. Shatat, G. Abdo, A. Dawodiah, and M. Sameer, "Design and ex vivo kidney evaluation of a high-intensity focused ultrasound transducer and 3D positioner," Medical & Biological Engineering & Computing, vol. 48, no. 3, pp. 269-276, 2010.
- [134] J. A. Gallego-Juarez, "Piezoelectric ceramics and ultrasonic transducers," Journal of Physics E: Scientific Instruments, vol. 22, no. 10, pp. 804-816, 1989.
- [135] A. C. Mathieson, Nonlinear characterisation of power ultrasonic devices used in bone surgery, PhD thesis, University of Glasgow, UK, 2012.
- [136] T. E. G. Álvarez-Arenas, "Acoustic impedance matching of piezoelectric transducers to the air," IEEE Transactions on Ultrasonics, Ferroelectrics, and Frequency Control, vol. 51, no. 5, pp. 624-633, 2004.
- [137] T. R. Gururaja, W. A. Schulze, L. E. Cross, R. E. Newnham, B. A. Auld, and Y. J. Wang, "Piezoelectric composite materials for ultrasonic transducer applications. Part I: Resonant modes of vibration of PZT rod-polymer composites," IEE Transactions on Sonics and Ultrasonics, vol. 32, no. 4, pp. 481-498, 1985.
- [138] B. Fu, Piezoelectric actuator design via multiobjective optimization methods, PhD thesis, University of Paderborn, Germany, 2005.

REFERENCES

- [139] Y. Kuang, A. Hilgers, M. Sadiq, S. Cochran, G. Corner, and Z. Huang, "Modelling and characterisation of a ultrasound-actuated needle for improved visibility in ultrasound-guided regional anaesthesia and tissue biopsy," *Ultrasonics*, vol. 69, pp. 38-46, 2016.
- [140] Hibbit, Karlesson and Sorensen, *ABAQUS User's Manual: Version 6.12*, 2013.
- [141] APC International., piezoelectric constants, <https://www.americanpiezo.com/knowledge-center/piezo-theory/piezoelectric-constants.html>, Accessed on May, 2016.
- [142] Z. S. Al-Sarraf, A study of ultrasonic metal welding, PhD thesis, University of Glasgow, UK, 2013.
- [143] A. D. M. Patel and B. A. U. Rajurkar, "Analysis of different shaped sonotrodes used for plastic welding," Published in institute of technology, Nirma University, Ahmadabad, 2001.
- [144] S. G. Amin, M. H. M. Ahmed, and H. A. Youssef, "Computer-aided design of acoustic horns for ultrasonic machining using finite-element analysis," *Journal of Materials Processing Technology*, vol. 55, no. 3-4, pp. 254-260, 1995.
- [145] G. Amza and D. Drimer, "The design and construction of solid concentrators for ultrasonic energy," *Ultrasonics*, vol. 14, no. 5, pp. 223-226, 1976.
- [146] K. M. Shu, Y. J. Wang, and H. S. Yen, "On the design and analysis of acoustic horns for ultrasonic welding teflon encapsulated O-Ring," *Advanced Materials Research*, vol. 753, pp. 402-406, 2013.
- [147] K. I. Mori, *Simulation of Material Processing: Theory, Methods and Application: Proceedings of the 7th International Conference NUMIFORM 2001*, Toyohashi, Japan: Taylor & Francis, 2001.
- [148] R. J. Morrissey and T. Nicholas, "Fatigue strength of Ti-6Al-4V at very long lives," *International Journal of Fatigue*, vol. 27, no. 10, pp. 1608-1612, 2005.
- [149] Z. Pan, Modelling and design of ultrasonic bone cutting blades, PhD thesis, University of Glasgow, UK, 2015.

REFERENCES

- [150] O. B. Ozdoganlar, B. D. Hansche, and T. G. Carne, "Experimental modal analysis for microelectromechanical systems," *Experimental Mechanics*, vol. 45, no. 6, pp. 498-506, 2005.
- [151] D. J. Ewins, *Modal Testing: Theory and Practice*: Research Studies Press, 1984.
- [152] M. Lucas, A. Cardoni, F. C. N. Lim, M. P. Cartmell, and J. A. McGeough, "Effects of modal interactions on vibration performance in ultrasonic cutting," *CIRP Annals - Manufacturing Technology*, vol. 52, no. 1, pp. 193-196, 2003.
- [153] X. Bao, S. Sherrit, M. Badescu, Y. Bar-Cohen, S. Askins, and P. Ostlund, "Free-mass and interface configurations of hammering mechanisms," U.S. Patent, 8,960,325, 2012.
- [154] X. Li, P. Harkness, K. Worrall, R. Timoney, and M. Lucas, "A parametric study for the design of an optimized ultrasonic percussive planetary drill tool," *IEEE Transactions on Ultrasonics, Ferroelectrics, and Frequency Control*, vol. 64, no. 3, pp. 577-589, 2017.
- [155] R. Lerch, "Simulation of piezoelectric devices by two- and three-dimensional finite elements," *IEEE Transactions on Ultrasonics, Ferroelectrics, and Frequency Control*, vol. 37, no. 3, pp. 233-247, 1990.
- [156] S. Voronina and V. Babitsky, "Autoresonant control strategies of loaded ultrasonic transducer for machining applications," *Journal of Sound and Vibration*, vol. 313, no. 3, pp. 395-417, 2008.
- [157] K. Li and A. P. Darby, "Modelling a buffered impact damper system using a spring-damper model of impact," *Structural Control and Health Monitoring*, vol. 16, no. 3, pp. 287-302, 2009.
- [158] M. Stauber and R. Müller, "Micro-computed tomography: a method for the non-destructive evaluation of the three-dimensional structure of biological specimens," *Osteoporosis: Methods and Protocols*, vol. 455, no. 37, pp. 273-292, 2008.
- [159] J. S. Thomsen, A. Laib, B. Koller, S. Prohaska, L. Mosekilde, and W. Gowin, "Stereological measures of trabecular bone structure: comparison of 3D micro computed tomography with 2D histological sections in human proximal tibial bone biopsies," *Journal of Microscopy*, vol. 218, no. 2, pp. 171-179, 2005.

REFERENCES

- [160] J. Lee, Y. Rabin, and O. B. Ozdoganlar, "A new thermal model for bone drilling with applications to orthopaedic surgery," *Medical Engineering & Physics*, vol. 33, no. 10, pp. 1234-1244, 2011.
- [161] F. Birkenfeld, M. E. Becker, B. Kurz, S. Harder, M. Kern, and R. Lucius, "Changes in human mandibular bone morphology after heat application," *Annals of Anatomy*, vol. 192, no. 4, pp. 227-231, 2010.
- [162] J. Lundskog, "Heat and bone tissue. An experimental investigation of the thermal properties of bone and threshold levels for thermal injury," *Scandinavian Journal of Plastic Reconstructive Surgery*, vol. 9, pp. 1-80, 1972.
- [163] G. F. Tawy, P. J. Rowe, and P. E. Riches, "Thermal damage done to bone by burring and sawing with and without irrigation in knee arthroplasty," *The Journal of Arthroplasty*, vol. 31, no. 5, pp. 1102-1108, 2016.
- [164] A. Feldmann and P. Zysset, "Experimental determination of the emissivity of bone," *Medical Engineering & Physics*, vol. 38, no. 10, pp. 1136-1138, 2016.

PUBLICATIONS

Appendix II: Publications

Journal Papers

1. A. Mathieson, R. Wallace, R. Cleary, L. Li, H. Simpson, and M. Lucas, “Ultrasonic needles for bone biopsy,” IEEE Transactions on Ultrasonics, Ferroelectrics, and Frequency Control, vol. 64, pp. 433-440, 2017.
2. L. Li, A. Mathieson, X. Li, and M. Lucas, “Modelling of an ultrasonic-sonic surgical needle for bone biopsy,” IEEE Transactions on Ultrasonics, Ferroelectrics, and Frequency Control, under revising and submit soon.

Conference Paper

1. L. Li, A. Mathieson, and M. Lucas, “A miniature surgical drill using ultrasonic/sonic frequency vibration,” Proceedings of the 2015 International Congress on Ultrasonics, France, pp. 14-17, 2015.